Multirate Control Techniques for Fast and Precise Positioning and Applications to High-Precision Stages

(高速高精度位置決めのためのマルチレート制御技術と
超精密ステージへの応用)

by

Koichi Sakata

(坂田　晃一)

Dissertation Submitted to

Division of Physics, Electrical and Computer Engineering

for the Degree of

Doctor of Philosophy

at

Yokohama National University

March 2011

Ph.D. Advisor:

Associate Professor Hiroshi Fujimoto

Supervisor:

Professor Atsuo Kawamura

邦文概要

精密位置決めステージは半導体や液晶パネル製造、微細加工に欠かせない産業機器である。近年、生産性向上のためステージは大型化の一途を辿っている。また、制御の観点からも高速高精度位置決め制御は、生産性や製品の精密化に大きく関わる重要な技術である。しかしながら、大型ステージはその剛性の低さから低周波域に共振モードを持つため、従来のシングルレートフィードバック制御では年々高まる要求仕様を満たすには限界がある。そこで本論文の前半では、ステージの各種制御に対して、高速高精度位置決めのためのマルチレート制御技術を提案した。さらに本論文の後半では、周辺技術として、パワーエレクトロニクス、センサ、メカニクスの分野にまたがったマルチレート制御技術の確立を行った。また、提案する制御技術は全て極めて実用的であり、大型精密ステージおよび実験用精密ステージを用いてその有効性を明らかにした。

本論文の内容及び構成を以下に示す。

第 1 章では、露光装置の歴史と、精密位置決めステージおよび 2 慣性系に関係する従来の代表的な制御の研究を振り返り、その有効性や問題点を明らかにし、本研究の位置付けを行った。従来の制御系では、フィードバック制御器設計が保守的になりがちであったり、低い共振に対して制振制御が十分でないといった問題があった。本論文では、マルチレート制御に基づくフィードフォワード制御器を精密位置決めステージの各種制御に導入し、性能の大幅な改善を実現した。

第 2 章では、大型超精密ステージに対して、完全追従制御 (PTC) を適用することで高速高精度位置決めの大幅な改善が望めることを実証した。PTC はマルチレート制御に基づくフィードフォワード制御であり、本章では制御対象の共振特性まで含めた制御対象の正確な逆システムを導出する制振 PTC を適用する。これにより、共振モードに阻まれフィードバック制御のみでは達成し得なかった高速高精度な位置決めを実現できた。また、精密ステージは、主にステップ駆動タイプとスキャン駆動タイプの 2 種類に分類することができる。ステップステージでは、移動後の整定時間をいかに短くするかが重要であり、スキャンステージでは、移動中の目標軌道への追従性能が問われる。本章では、この 2 つの要求仕様に制振 PTC が有効であることを、それぞれの大型超精密位置決めを用いて実証した。

第 3 章では、2 つの精密ステージの実位置を同期させる、マルチレート制御に基づく同期位置決め制御を提案し、2 台の実験用精密ステージを用いてその有効性を実証した。工作機器や露光装置といった産業機器では、精密ステージをマスタ・スレーブ方式により同期位置

決め制御させることがしばしば要求される。同期位置決め制御では、システムに存在するむだ時間や外乱が同期精度に影響を及ぼしやすい。そこで本章では、前章にて設計されたPTCシステムに対して、むだ時間を考慮したオブザーバを設計することで、むだ時間およびマスタ側の外乱に強い同期位置決め制御システムを提案した。

第4章では、マルチレート制御に基づく姿勢制御を提案し、スキャンタイプの大型超精密ステージを用いてその有効性を実証した。レンズ機構を有する露光装置では、製造品の微細化のためレンズのフォーカス範囲が年々狭まっており、このフォーカス範囲内にステージの姿勢を保ちながらスキャン駆動させる必要がある。つまり、前章までの並進方向の位置決め制御に加えてステージ平面のピッチング、ローリング、高さを同時に制御することが求められる。また、姿勢の検出にはイメージセンサが用いられる。センサの出力周期はDSPの演算周期に比べて十数倍長く、シングルレートフィードバック制御では制御周期を出力周期に合わせなければならず、十分な性能を発揮できない問題がある。そこで本章では、並進方向の駆動力と表面形状に由来する外乱をモデル化し、外乱情報を制振PTCの目標軌道に用いた制御系を提案した。

本論文の後半では、パワーエレクトロニクス、センサ、メカニクスの分野にまたがったマルチレート制御技術の確立を行った。第5章では、インバータのPWMパルスに基づくモデルとマルチレート制御を組み合わせたマルチレートPWM制御を提案し、キャリア周期のわずか10周期分という短さで位置決めがナノスケールの精度で完了する超高速ナノスケールサーボを実現した。これは、インバータの動特性まで考慮することで、はじめて可能となるパワーエレクトロニクスの技術を取り入れたマルチレート制御技術である。この制御技術はある程度高剛性の精密ステージに対して有効であり、実験用精密ステージを用いてその有効性を実証した。産業機器では、半導体露光装置に使われているステージがこの制御技術に適していると言える。

第6章では、前章同様、モーションコントロールでは一般的に取り扱われない電流ループの特性まで考慮したマルチレート制御技術が位置制御だけでなく、電流制御、速度制御にまで有効であることをACモータを用いて実証した。提案する制御技術は、ドライバのスイッチングロスの低減と追従性能の向上というトレードオフの関係を両立できることを実証した。さらに、マルチレートフィードフォワード制御のロバスト性について理論的に解析を行い、プラント変動による性能劣化について考察を行った。

第7章では、センサの位置情報から速度情報を取得する際に発生する量子化誤差を低減するオブザーバを提案し、実験用精密ステージを用いてその有効性を実証した。一般に精密ステージには1 nm/pulseの非常に高分解能なリニアエンコーダないしレーザ干渉計が用いられ、位置のみならず速度も制御することがしばしば求められる。しかしながら、これらのセンサの位置情報から差分によって得られる速度にはわずかではあるが量子化誤差が乗ってしまい、ナノスケールの制御ではこれを嫌う。そこで本章では、オブザーバの演算周期と制御周期の違いを巧みに利用したマルチレートに基づくオブザーバを提案し、速度のみならず精度の良い状態量を推定できることを実証した。

第8章では、2慣性システムに大変有効な複数センサを用いたフィードバック制御設計を

提案した。駆動側と負荷側に分かれる 2 慣性システムのフィードバック制御は、制御したい負荷側の状態量を直接センサで検出し制御するフルクローズド制御と、駆動側の状態量を検出し間接的に負荷側を制御するセミクローズド制御に分類できる。しかし、いずれもモータトルクを制御入力、センサの検出量を出力とした 1 入力 1 出力 (SISO) 系がほとんどである。2 慣性システムの有する共振モードは、ノッチフィルタ等で抑圧する他なく、第 2 章で述べたようにフィードバック制御の高帯域化の妨げになるうえ、わずかなプラント変動に対して制御系が不安定になりやすい。そこで本章では、負荷側と駆動側の両方にセンサを用いた 1 入力 2 出力 (SIMO) 系とするだけで共振モードに対して完全にロバストなフィードバック制御設計法を提案した。本手法は機械パラメータに基づく大変見通しの良い制御設計法である。センサの追加は多少のコストがかかるが、機械的構造変更に比べて容易であり、共振モードのロバスト化とフィードバックの高帯域化の実現といった何倍もの見返りがある。また、提案するフィードバック制御設計は、大型超精密ステージに有効であるのはもちろんのこと、一般的な 2 慣性システムに対して理論展開した。

第 9 章では、テーブル機構を有する実験用精密ステージの設計製作について述べる。製作した精密ステージは、並進方向、ピッチング、ローリング、高さの 4 自由度を持つステージである。テーブル機構に関して FEM 解析およびモーダル解析を用いて機械のモード形状とプラント特性の関係を明らかにした。また、第 2 章、第 4 章で述べた制御系を適用し、製作した実験用ステージに対して有効であることを実証した。

第 10 章では、各章を振り返り、本論文を結論付けた。各章で述べた適用例は、従来の制御手法の性能を大幅に改善し、実製品に適用可能である。この事実から本研究が精密位置決めの分野に与える貢献は大きく、さらには各分野にまたがった複合的な制御を提案し、新たなマルチレート制御技術の確立に成功したと言うことができる。

なお、本文は英語により記述されていることを付記する。

Multirate Control Techniques for Fast and Precise Positioning and Applications to High-Precision Stages

by

Koichi Sakata

Dissertation Submitted to

Division of Physics, Electrical and Computer Engineering

for the Degree of

Doctor of Philosophy

at

Yokohama National University

March 2011

Ph.D. Advisor:

Associate Professor Hiroshi Fujimoto

Supervisor:

Professor Atsuo Kawamura

Acknowledgments

First of all, I would like to express my gratitude to my previous supervisor and Ph.D. advisor Associate Professor Hiroshi Fujimoto of the University of Tokyo for giving me valuable advice on this work and influencing my way of thinking. He taught me many things not only on my research but also how engineering and a researcher should be. His instructive advice always stimulated me. He also gave me opportunity to take part in academic committees and conferences, and to discuss with many academic and industrial researchers. I can never imagine that I could accomplish this work without his kind help. I am very proud that I was a member of his laboratory from 2005 to 2010 in Yokohama National University and from 2010 to 2011 in the University of Tokyo. These six years will be my precious treasure through my life. I would like to thank Professor Atsuo Kawamura, who was my supervisor when I was in the last doctoral course from 2010 to 2011. He helped me research in the University of Tokyo by using the research guidance commission.

I appreciate all members of the committees for nano scale servo (NSS) of IEE Japan, where I served as an observer. They gave me many comments about this work from the point of view both in the motion control theory and practical industries.

I would like to thank Mr. Kazuaki Saiki, Mr. Atsushi Hara, Mr. Takeshi Ohtomo, Mr. Takachika Shimoyama, and their colleagues of Nikon Corporation for many helpful discussions through the collaborative research. They have improved and implemented the proposed multirate control techniques to the latest products. This success encouraged me very much.

I wish to express my gratitude to Professor Tsutomu Oyama, Associate Professor Yasutaka Fujimoto, and Assistant Professor Takao Tsuji of Yokohama National University, who are members of the judging committee of my doctoral degree with Professor Atsuo Kawamura and Associate Professor Hiroshi Fujimoto. Their constructive comments in the preliminary judging meeting helped me to modify this dissertation.

I am greatly thankful to the previous and current members of my laboratory. They sometimes helped me to prepare the experimental setups and to take care of our computer systems. Discussion with my colleagues and all members of my laboratory always stimulated me. I appreciate Ms. Eriko Hino and Ms. Yoko Matsushima, Associate Professor Hiroshi

Fujimoto's office administrators, for their sincere work.

This dissertation cannot have finished without financial support by Japan society for the promotion of science (JSPS), where I am supported as research fellow. A part of this research was carried out with a subsidy of the Scientific Research Fund of the Ministry of Education, Science, Sports and Culture of Japan.

Finally, I would like to thank all my family members and good friends for their encouragement and support.

Koichi Sakata
Yokohama National University
March 2011

Contents

List of Figures

List of Tables

Notation

$\triangleq$	defined as
$\boldsymbol{A}$	matrix
$\boldsymbol{I}$	identity matrix
$\boldsymbol{O}$	zero matrix
$\boldsymbol{A}^T$	transpose of $\boldsymbol{A}$
$\boldsymbol{A}^{-1}$	inverse of $\boldsymbol{A}$

$G(s)$	continuous-time system
$G[z]$	discrete-time system
$x(t)$	continuous-time signal
$x[k]$	discrete-time signal
$\left[\begin{array}{c\|c} \boldsymbol{A} & \boldsymbol{B} \\ \hline \boldsymbol{C} & \boldsymbol{D} \end{array}\right]$	$\triangleq \boldsymbol{C}(z\boldsymbol{I}-\boldsymbol{A})^{-1}\boldsymbol{B}+\boldsymbol{D}$: shorthand for state space realization

Chapter 1

Introduction

1.1 Background of the Research

Mechatronic systems, such as industrial robots, NC machine tools and exposure systems require fast and precise position control in order to improve productivity and product quality. Especially, high-precision stages are applied to NC machine tools and exposure systems. Here, let me explain the history of the exposure systems and the demands.

History of the exposure systems

Today, integrated circuits (ICs) are used in all kinds of electronic devices, for example PCs and mobile phones to televisions and so on. ICs must be crucial components in IT-based society today and in the future. Also, liquid crystal displays (LCDs) are employed in a wide range of products including PC monitors, mobile phones, digital cameras, video cameras, LCD TVs and so on. Nowadays, high performance applications like smart phones and 3D LCD TVs are being developed. This market is spreading more and more.

The most important manufacturing equipment of the ICs and the LCDs is the exposure system. The exposure system has the important role which is "Photolithography". Photolithography, a term created by combining the words "Photo" (photograph) and "Lithography" (a method of printing using a stone surface), is a type of lithographic printing that employs photographic technology. It is the process of printing circuit patterns to glass substrates on the precision stage by using lens and laser light.

The first exposure system appeared for ICs in 1980. It is called "Stepper" because this system is driven as step-and-repeat. In the middle of 1990s, "Scanner" was developed in order to expand the exposure field and improve the productivity. This is applied to the lens-scanning system, where the two stages on which the reticle (mask) and wafer are mounted are moved simultaneously during exposure.

The exposure systems also appeared for LCDs in the middle of 1980s. The LCD exposure

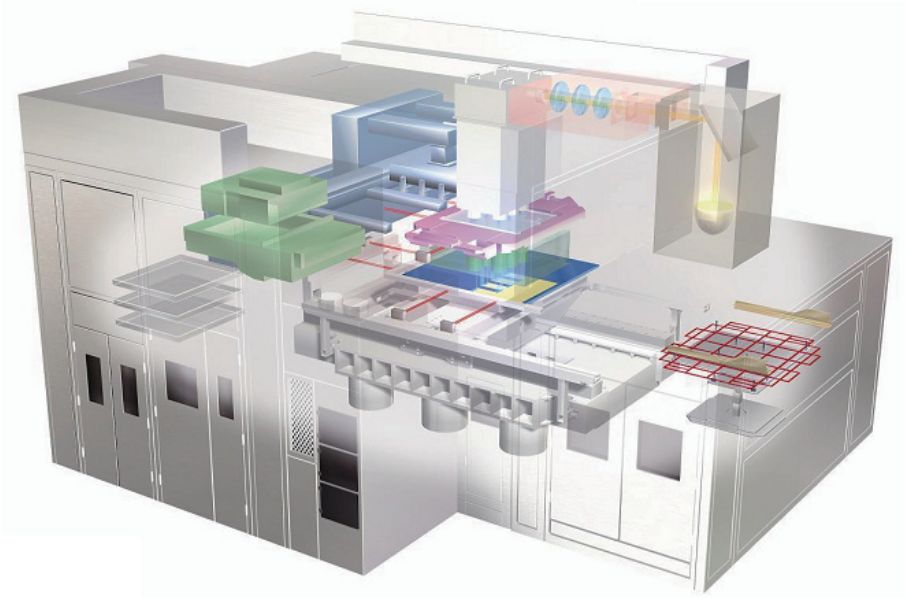

Figure 1.1: LCD exposure system (Scanner).

systems are derivatives of the IC exposure systems. These are also classified into stepper and scanner. Steppers are for the production of small LCDs of PC monitors, mobile phones, digital cameras and video cameras. Scanners are for the production of large LCDs of LCD TVs and so on. The overview of the scanner is shown in Fig. 1.1. The basic mechanics of the LCD exposure systems is almost the same as that of the IC exposure systems. The big difference between LCD and IC exposure systems is the size of the precision stages on which glass substrates are mounted. The reason is that larger LCDs are required in the market of LCD TVs. Now, the 10th generation exposure system is the latest. The latest one can print circuit patterns to the plate whose size is about 3×3 m. It is still on the way of evolution.

Approach by control techniques

In early 2000s, it was tried that feedback control based on H_∞ synthesis was applied to wafer stages of IC exposure systems [1, 2]. H_∞ control treats the uncertainty of the plant based on the small gain theorem to assure the robust stability of only the gain. Thus, conservative controllers are generally obtained. The precision control of a XY-table driven by a linear motor, a DC-motor with a ball-screw or a piezoactuator has also been widely studied [3]-[6]. They described on feedback control design about robust control in [3], nonlinear feedback control in [4] and [5]. However, these are not enough for fast and precise positioning of the large-scale precision stages which have low resonance mode.

Also, iterative learning control which is a kind of feedback control was applied to wafer stages of IC exposure systems [7, 8, 9]. ILC can improve the tracking error of the system

which executes the same task multiple times by learning from previous tracking errors. Therefore, ILC does not need the precise plant model. ILC works well even though the system has a non-linear characteristic or a uncertainty of the plant. However, the convergence of the tracking error often assumes the high bandwidth feedback control. In the large scale high-precision stage which has the row resonance mode, the performance of ILC is not enough. As above, a feedforward control is absolutely imperative for fast and precise positioning in high-precision stage. In [10], ILC is applied to a feedforward control. The feedforward gains with respect to the acceleration and the jerk are optimized by iterative learning.

The resonance mode of the high-precision stage is a serious problem against fast and precise positioning. Many vibration suppression controls have been researched in the field of motion control. Representative researches are introduced from both feedback and feedforward control approach.

Resonance ratio control [11, 12] is a kind feedback control to reduce the amplitude of the resonance mode and to remove it to higher frequency by using disturbance-observer-based techniques. The resonance ratio between the resonance mode and the anti-resonance mode is determined by the inertia ratio between the motor and the load. This control method can change the resonance ratio by the appropriate observer gain. This control method is simple and effective, but it cannot remove the resonance mode absolutely. Especially, the effectiveness of resonance ratio control is not still enough in the system which has the low resonance mode.

Phase-lead compensation is also a good feedback control technique for the vibration suppression. [13] proposed to set a notch filter at higher frequency than the resonance mode on purpose in order to make the phase margin. It is said that the curve of the resonance mode should be removed to the first quadrant in the open loop vector locus (Nyquist diagram). The phase compensation has an advantage compared with the gain compensation. It is robustness against the resonance variation. Although the gain compensation does not allow the resonance variation at all, the phase compensation can allow small quantity of the resonance variation. [14] proposed a vibration suppression control based on a phase-lead compensation for multi-inertia system. The phase-lead compensation is based on a disturbance observer and can stabilize all resonance modes. This dissertation also proposes a novel feedback control to overcome the resonance problem in chapter 8.

Final-state control [15] is a kind of feedforward control for the vibration suppression. This control method can obtain a feedforward control input whose frequency components are minimum at the desired frequency points. It is enough that the evaluation function and the step number of the tracking are only prepared. [16] applied the final-state control to short track-seeking control of hard disk drives (HDDs).

Genetic algorithms are also effective to the vibration suppression and the feedforward control design [17, 18, 19]. The optimal set of the plant parameters and the free parameters

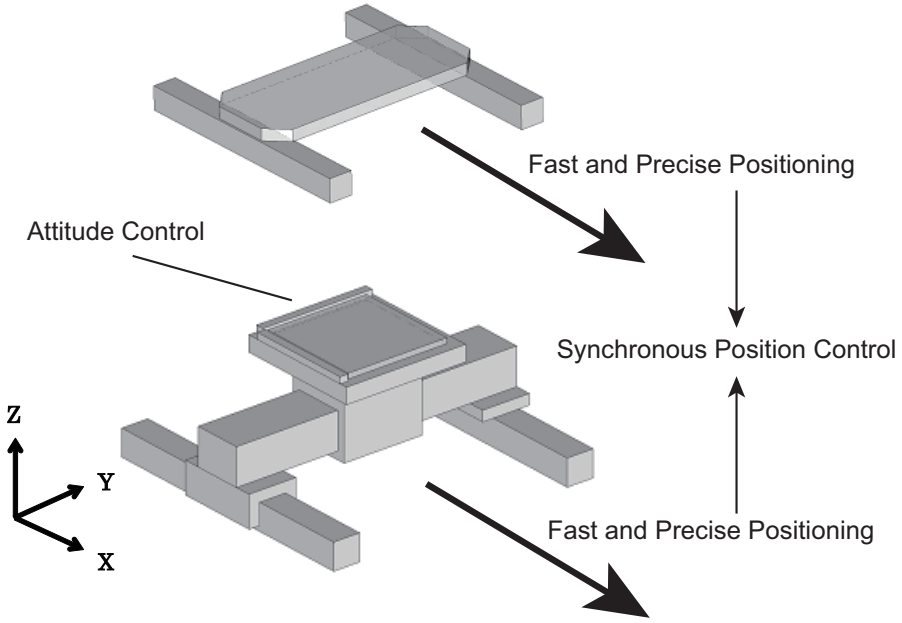

Figure 1.2: Control techniques for high-precision stages.

of compensators can be identified by the optimization ability of GA. Therefore, GA has advantages that the initial plant identification and design of compensators based on the plant model are unnecessary, and it is robust against plant variations.

1.2 Motivations of the Dissertation

Required control techniques for high-precision stages are shown in Fig. 1.2. High-precision stages require not only fast and precise positioning but also synchronous position control and attitude control.

Perfect tracking control method based on multirate feedforward control was proposed [20]. Then this method already was applied to commercial HDDs, and the effectiveness was evaluated [21]. Multirate control techniques are applied to these controls of high-precision stages in this dissertation. Then, the multirate control techniques which extend to power electronics, sensors and mechanics around control techniques are established. This dissertation evaluates that multirate control systems are highly effective for practical high-precision stages.

1.3 Outline of the Dissertation

The chapters of this dissertation are classified in Fig. 1.3. This dissertation consists of two parts. In the early part, applications of multirate control techniques to high-precision

stages are introduced. In the latter part, multirate control techniques which extend to power electronics, sensors and mechanics around control techniques are established. The details of each chapter are as follows.

In chapter 2, perfect tracking control (PTC) is applied to fast and precise positioning of large-scale high-precision stage. PTC consists of feedback control and feedforward control based on multirate control. In this chapter, vibration suppression PTC which can control resonance mode actively is applied. Precision stages can be classified into stepping drive type (called step stages) and scanning drive type (called scan stages or gantry stages). The settling time is very important specification of step stages in order to improve throughput. The tracking performance to the target trajectory in moving is required in scan stages. Experiments of fast and precise positioning with each type large-scale high-precision stage are performed to show the advantages of PTC to each demand.

In chapter 3, a synchronous position control system based on multirate control is proposed in order to synchronize real positions of two precision stages. Then, experiments with two experimental precision stages are performed to show the advantages of the proposed control system. A synchronous position control system by master-slave method is often required in industrial equipment, for example, NC machine tools, exposure systems, and so on. Synchronous position system is easily influenced by not only disturbances but also dead-times. In this chapter, a novel synchronous position control system based on multirate control and dead-time compensation is proposed for a pair of precision stages which are designed by PTC in previous chapter.

In chapter 4, an attitude control based on multirate control is proposed. Then, experiments with large-scale high-precision stage of scan type are performed to show the advantages of the proposed control system. In exposure systems which have lens, the focus range of lens narrows for microfabrication of products every year. These systems require scanning drive on keeping the attitude of the stage in the focus range. Thus, the positions in not only the translation direction but also the pitching, the rolling and the height directions must be controlled. Moreover, the sampling time of output is much longer than the sampling time of control input by DSP because image sensors are employed in the output encoder. It is difficult to reject the disturbances by single-rate feedback system. In this chapter, the disturbances via the driving force in the translation direction and the surface shape of the stage are modeled, and then the multirate control system in which the disturbance information is utilized as the target trajectory is proposed.

In chapter 5, multirate PWM control which combines multirate control with modeling based on PWM pulses of the inverter is proposed. This chapter illustrates ultrahigh-speed nanoscale positioning based on the proposed method with an experimental precision stage. The position error is in 100 nm. The positioning time is 2 ms which was only 10 times as long as the carrier period. This is a novel multirate control technique which introduces power

electronics technique with considering dynamics of the inverter. This control technique is effective in high-precision stages which are rigid until several hundred Hz. Then, experiments with an experimental high-precision stage are performed to show the advantages of the proposed control technique. This control technique can be applied to stages of semiconductor exposure systems in industrial equipment.

In chapter 6, it is shown that multirate control technique with considering dynamics of the driver is effective in not only position control but also speed and current control. The proposed control technique can satisfy both reduction of switching loss of the driver and the tracking performance. Experiments with an AC motor are performed to show the advantages of the proposed control technique. Moreover, the robustness of multirate feedforward controller is verified both theoretically and experimentally.

In chapter 7, an observer which can estimate state variables with reducing the quantization error of the encoder is proposed. High resolution encoders are employed to industrial equipment which is required accuracy, for example, NC machine tools, exposure systems, and so on. Generally, the velocity of machines is calculated by the difference of the position given by the encoder. Although the high resolution encoder is employed, the quantization error and the half sample delay induced by the difference cannot be avoided. These are problems in the case of required high precise velocity. The proposed observer based on multirate control utilizes the difference between the updating time of the observer and the sampling time of control input. Experiments with experimental precision stages are performed to show the advantages of the proposed observer.

In chapter 8, another position sensor is applied to a high-precision stage in the case that it is difficult to change the structure additionally. It is shown that it is possible to design a novel feedback control which not only has high bandwidth but also is absolutely robust against the resonance mode parameters. Finally, simulations and experiments with the high-precision stage are performed to show the advantages of the proposed feedback control design. Here, adding sensors is often apt to be avoided because of sensor cost, but it is considered that sensors should be applied positively if high productivity brings in benefits more than the sensor cost. Finally, the proposed control design is generalized to the general 2 inertia system.

In chapter 9, a new experimental 4-DOF high-precision stage is designed and fabricated. The 4-DOF stage which has the table part can move to not only one translation but also the height, the pitching, and the rolling directions. The structure of the table part is analyzed by both FEM analyses and experimental modal analyses, and then relationship between the mode shapes and plant characteristics is demonstrated. Moreover, control systems in chapter 2 and 4 are applied to the stage, and experiments are performed to show the advantages of the control systems.

In chapter 10, each chapter is reviewed, and then the conclusion of this dissertation is

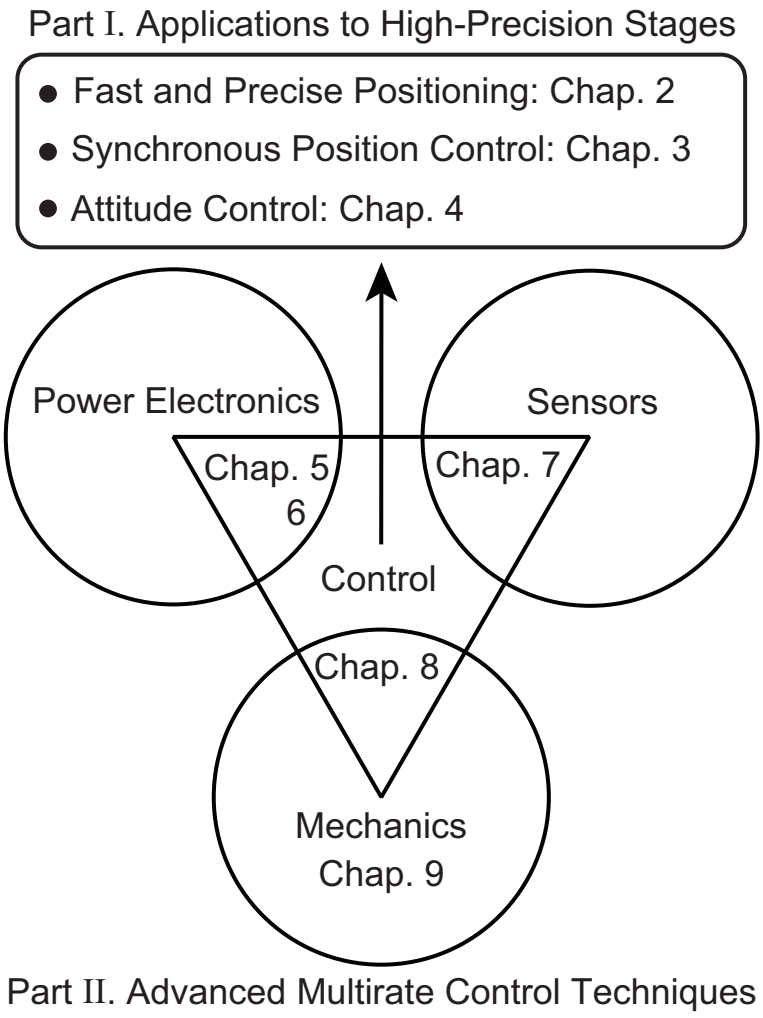

Figure 1.3: Classified chapters of this dissertation.

stated.

Part I

Applications to High-Precision Stages

Chapter 2

Fast and Precise Positioning based on Vibration Suppression PTC

2.1 Abstract

In the positioning system of the large-scale high-precision stage, the primary resonance mode appears in low frequency even in the high stiffness stage. The resonance mode is a major obstacle of fast and precise positioning. In this chapter, vibration suppression PTC (Perfect Tracking Control) which can control the resonance mode actively is applied to the large-scale stage. Finally, simulations and experiments are performed to show the advantages of the vibration suppression PTC.

2.2 Introduction

Large-scale high-precision stages are used in industrial fields such as manufacturing of semiconductors and liquid crystal panels (or displays). Fast and precise positioning control is very important technology related to the improvement of throughput and product quality.

However, a large-scale stage has a low resonance mode because of the low rigidness. It is called that the resonance mode is an obstruction of fast and precise positioning by [22].

Therefore, the large-scale stage cannot depend on a high gain and high feedback control. A two degree of freedom control method that enables an accurate feedforward control should be applied.

[23] indicates that the inverse system of the plant cannot be designed in discrete-time because unstable zero appears in the plant discretized by zero-order hold. [24] proposed the zero phase error tracking controller (ZPETC) which compensates both phase and gain errors caused by uncancellable unstable zeros of discrete-time plant.

Whereas, [20] proposed a perfect tracking control (PTC) based on multi-rate feedforward

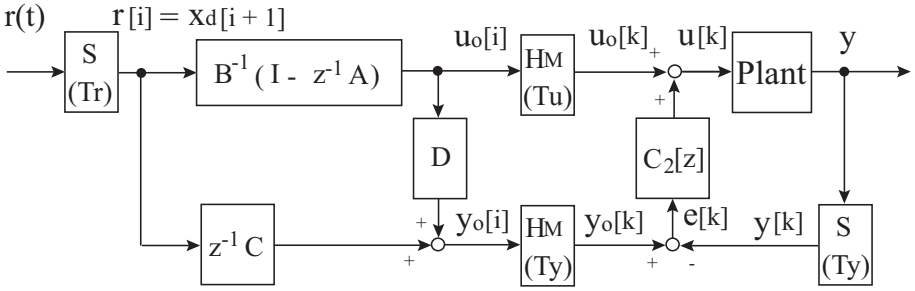

Figure 2.1: Perfect tracking control system.

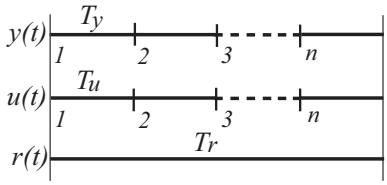

Figure 2.2: Multirate sampling period.

control to eliminate the problem of unstable-zeros. PTC theoretically guarantees that a feedforward control based on an accurate inverse system for a nominal model can be realized and perfect tracking for every sampling period can be achieved as long as there is no unstable zero in the nominal model defined by a continuous-time system. Moreover, [21] also proposed vibration suppression PTC which deals with resonance modes of a plant, and applied to hard disk drives (HDDs).

In recent years, our research group has applied the PTC method to a large-scale high-precision stage to improve the control performance. This chapter describes the application of the PTC method to a large-scale stage.

2.3 Perfect Tracking Control

Perfect tracking control (PTC) [20] which consists of the 2-DOF control system as shown in Fig .2.1. This system has two samplers for the reference signal $r(t)$ and the output $y(t)$, and two holders for the input $u_o(t)$ and nominal output $y_o(t)$. Therefore, there exist sampling periods T_r, T_y and T_u which represent the periods of $r(t)$, $y(t)$, and $u(t)$, respectively. PTC applies the multirate feedforward control in which the control input $u(t)$ is changed n times during one sampling period T_r of reference input $r(t)$ as shown in Fig. 2.2.

Here, n is the plant order. H_M in Fig. 2.1 is the multirate holder which outputs the input $u[i] = [u_1[k] \cdots u_n[k]]^T$ (generated by the long sampling period T_r) on the short sampling period T_u.

Here, the plant discrete time state space matrices $\boldsymbol{A}$, $\boldsymbol{B}$, $\boldsymbol{C}$ and $\boldsymbol{D}$ at the long sampling period T_r can be derived as (2.2) from the discrete time plant model (2.1) at the short sampling period T_u.

$$\boldsymbol{x}[k+1] = \boldsymbol{A}_s\boldsymbol{x}[k] + \boldsymbol{b}_s u[k] \ , \ y[k] = \boldsymbol{c}_s\boldsymbol{x}[k] \tag{2.1}$$

$$\left[\begin{array}{c|c} \boldsymbol{A} & \boldsymbol{B} \\ \hline \boldsymbol{C} & \boldsymbol{D} \end{array}\right] = \left[\begin{array}{c|ccc|c} \boldsymbol{A}_s^n & \boldsymbol{A}_s^{n-1}\boldsymbol{b}_s & \cdots & \boldsymbol{A}_s\boldsymbol{b}_s & \boldsymbol{b}_s \\ \hline \boldsymbol{c}_s & 0 & \cdots & 0 & 0 \\ \boldsymbol{c}_s\boldsymbol{A}_s & \boldsymbol{c}_s\boldsymbol{b}_s & \cdots & 0 & 0 \\ \vdots & \vdots & \ddots & \vdots & \vdots \\ \boldsymbol{c}_s\boldsymbol{A}_s^{n-1} & \boldsymbol{c}_s\boldsymbol{A}_s^{n-2}\boldsymbol{b}_s & \cdots & \boldsymbol{c}_s\boldsymbol{b}_s & 0 \end{array}\right] \tag{2.2}$$

Since the matrix $\boldsymbol{B}$ of (2.2) is non-singular in the case of controllable plant, PTC can be designed as

$$\begin{aligned} \boldsymbol{u}_o[i] &= \boldsymbol{B}^{-1}(\boldsymbol{I} - z^{-1}\boldsymbol{A})\boldsymbol{x}_d[i+1] \\ &= \left[\begin{array}{c|c} \boldsymbol{0} & \boldsymbol{I} \\ \hline -\boldsymbol{B^{-1}A} & \boldsymbol{B^{-1}} \end{array}\right] \boldsymbol{x}_d[i+1] \qquad (2.3) \\ y_o[i] &= z^{-1}\boldsymbol{C}\boldsymbol{x}_d[i+1] + \boldsymbol{D}\boldsymbol{u}_o[i]. \qquad (2.4) \end{aligned}$$

(2.3) is the stable inverse system of plant with input from the previewed desired trajectories. Therefore, perfect tracking is assured at the sampling period T_r.

The feedback control $C_2[z]$ suppresses the error between the output $y[k]$ and the nominal output $y_o[k]$ caused by disturbance or feedforward control imperfectness due to plant model error.

2.4 Modeling of High-Precision Stages

2.4.1 Step Stage

The step stage (XY stage) which is actuated by a ball screw is considerd. X axis of the stage is regarded as the two-inertia system structured by the rotational system of the motor and the translational system of the stage as Fig. 2.3. X axis is only described in this chapter because Y axis can be treated in the same way as X axis. J_{ms} and C_{ms} are the inertia and the viscosity of the motor screw. K_n and C_n are the stiffness and the viscosity of the screw nut. BE is the transfer constant from the translational system to the rotational system. The mass M_{px} of the moving part of the X axis stage is 266 kg. The ball screw pitch SP is 0.01 m/rev. T is the motor torque. P_x and v_x are the translational position and the translational velocity. θ and ω are the rotational position and the rotational velocity.

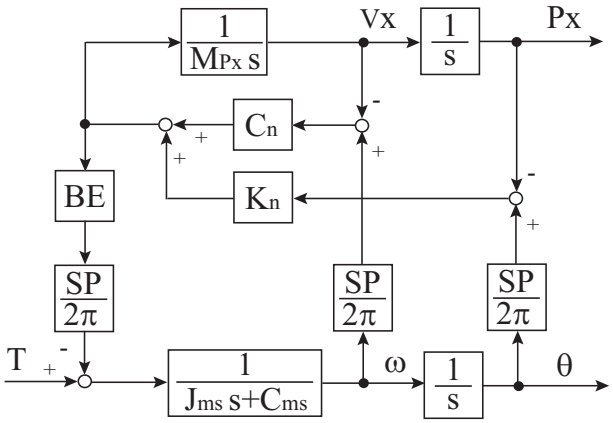

Figure 2.3: Model of step stage.

The plant models from the motor torque T to the translational position P_x and to the rotational position θ are represented by,

$$P_1(s) = \frac{P_x}{T} = \frac{y}{u} = \frac{b_1 s + b_0}{a_4 s^4 + a_3 s^3 + a_2 s^2 + a_1 s}, \tag{2.5}$$

$$P_\omega(s) = \frac{\omega}{T} = \frac{\omega}{u} = \frac{b_{\omega 3} s^3 + b_{\omega 2} s^2 + b_{\omega 1} s}{a_4 s^4 + a_3 s^3 + a_2 s^2 + a_1 s} \tag{2.6}$$

$$\begin{cases} a_4 = (2\pi)^2 J_{ms} M_{Px} \\ a_3 = (2\pi)^2 (J_{ms} C_n + M_{Px} C_{ms}) + BE \cdot SP^2 M_{Px} C_n \\ a_2 = (2\pi)^2 (J_{ms} K_n + C_{ms} C_n) + BE \cdot SP^2 M_{Px} K_n \\ a_1 = (2\pi)^2 C_{ms} K_n \\ b_1 = 2\pi \cdot SP \cdot C_n, \ b_0 = 2\pi \cdot SP \cdot K_n \\ b_{\omega 3} = (2\pi)^2 M_{Px}, \ b_{\omega 2} = (2\pi)^2 C_n, \ b_{\omega 1} = (2\pi)^2 K_n \end{cases}$$

Here, the denominatior of (2.6) is represented to be equal to that of (2.5). The measured frequency responses are shown in Fig. 2.4. The resonance mode exists at about 70 Hz in low frequency.

2.4.2 Gantry Stage

The large-scale high-precision stage with degrees of freedom $XY\theta$ axes is the form with an individual multi-layer Z axis air guide for each degree of freedom as shown in Fig. 2.5. It is called gantry stage.

The gantry stage can be modeled as a mechanically separated SISO-system since it has an individual multi-layer Z axis air guide for each degree of freedom. However, due to the multi-layer configuration, it is generally difficult to adjust the Z position of the actuator to match the Z position of the stage center of gravity. For this reason, if that structure is

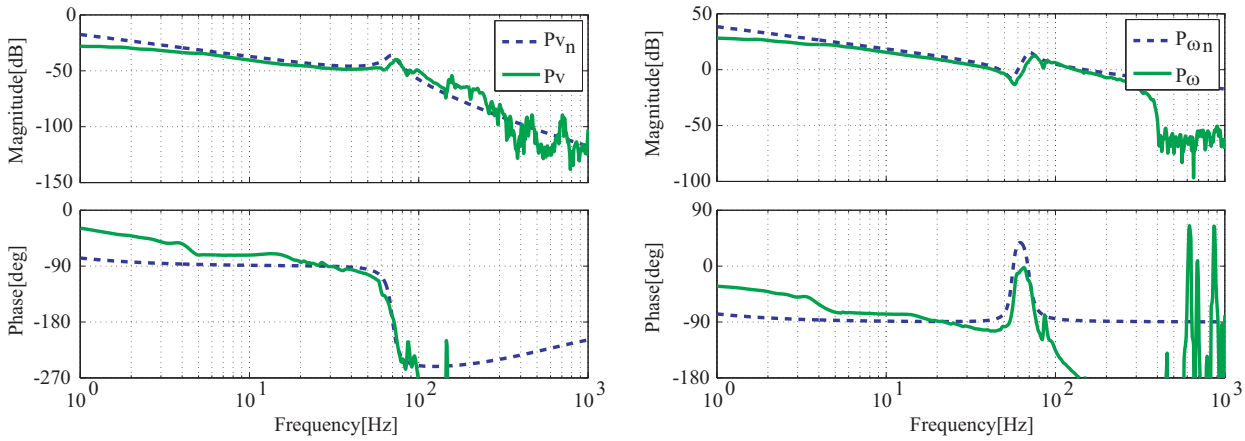

(a) v_x/T (b) ω/T

Figure 2.4: Frequency responses of step stage.

simplified, it can be illustrated as Fig. 2.6. It is assumed that $\sin\theta$ is equal to θ because θ is very small. The transfer function of the plant model is represented by

$$P_2(s) = \frac{X_2}{f} = \frac{y}{u} = \frac{b_2 s^2 + b_1 s + b_0}{a_4 s^4 + a_3 s^3 + a_2 s^2 + a_1 s}, \tag{2.7}$$

$$\begin{cases} a_4 = MmL^2 + MJ + mJ \\ a_3 = M\mu_\theta + m\mu_\theta + (mL^2 + J)C \\ a_2 = Mk_\theta + mk_\theta - MmgL - m^2gL + \mu_\theta C \\ a_1 = (k_\theta - mgL)C \\ b_2 = mL^2 + J - mLl,\ b_1 = \mu_\theta,\ b_0 = k_\theta - mgL \end{cases}, \tag{2.8}$$

where each parameters is shown in Fig. 2.6.

Fig. 2.7 shows the frequency responses of the plant model and actual machine, and they are almost identical to the primary resonance mode (about 17 Hz).

2.5 Control System Design

In this section, conventional and proposed control system designs are explained based on the step stage model. These control system designs as follows can be also applied to the gantry stage basically.

2.5.1 Feedback Controller Design

The conventional control system consists of the feedback controllers based on the translational position controller $C_{Px}(s)$ and the rotational velocity controller $C_\omega(s)$ like Fig. 2.8.

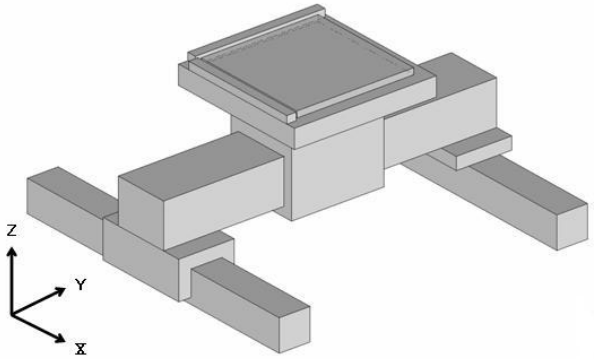

Figure 2.5: Structure of gantry stage.

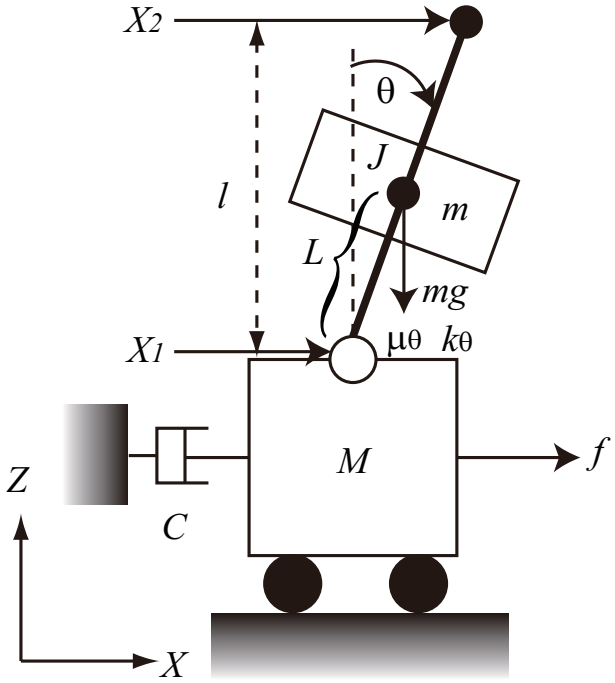

Figure 2.6: Model of gantry stage.

$C_{Px}(s)$ is designed as a proportional controller with a low-pass filter (LPF), and $C_{\omega}(s)$ is designed as a proportional-integral controller with a phase-lead-compensator. The designed $C_{Px}(s)$ and $C_{\omega}(s)$ are discretized by Tustin transformation so that the discrete controller $C_{Px}[z]$ and $C_{\omega}[z]$ are obtained.

Each parameter of the feedback controllers is selected by fine-tuning from frequency responses of the actual experiment. Fig. 2.9 (a) indicates the frequency response of the rotational velocity feedback loop (from ω_{ref} to ω), and Fig. 2.9 (b) indicates the frequency response of the entire feedback loop (from y_{ref} to y). It is shown that the bandwidth is only about 3 Hz in Fig. 2.9 (b). Therefore, the target specification cannot be satisfied only with the feedback controller. The P-PI control system which has a velocity loop inside a position loop is also used as the feedback controller in the gantry stage. In the case of using an approximated simple plant model, feedback controllers are apt to be designed conservatively. Therefore, those parameters were designed through a trial and error process in order to avoid a conservative design.

2.5.2 Conventional Feedforward Controller

In the experiments in the following section, the proposed method is compared with a conventional method. The conventional feedforward controller used in the comparison will be explained below.

A conventional feedforward controller assumes that the plant model is equal to a rigid

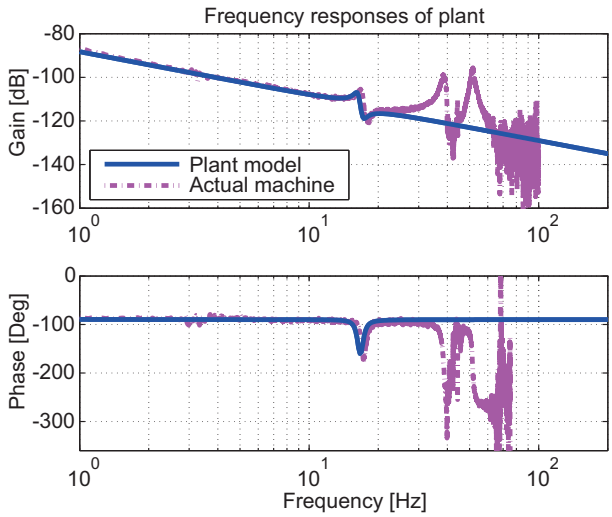

Figure 2.7: Frequency responses of gantry stage.

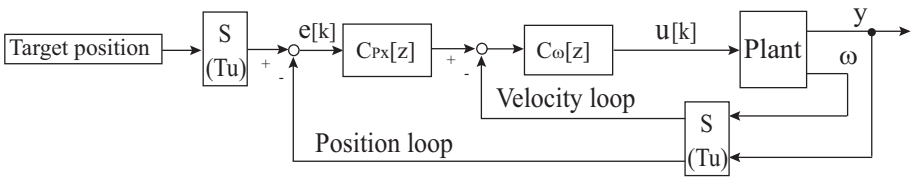

Figure 2.8: Feedback control system.

model. And, using the differential trajectory of the target trajectory $r(t)$, the output of controller $u_{FF}(t)$ is calculated as

$$u_{FF}(t) = h_2\ddot{r}(t) + h_1\dot{r}(t), \tag{2.9}$$

where the coefficients of h_2 and h_1 are theoretically equal to the mass and viscosity of a rigid model. However, in reality, they are determined through a trial and error process. As shown in Fig. 2.10, this controller is combined with previous feedback controller. As a result, the conventional control system is single rate control.

2.5.3 Singlerate Vibration Suppression PTC

First, PTC is designed in continuous time for two-inertia system model including the resonance mode. An inverse system of the plant P can be represented by

$$u_0 = N(s)\left(a_4 y_0^{(4)} + a_3 y_0^{(3)} + a_2 y_0^{(2)} + a_1 y_0^{(1)}\right), \tag{2.10}$$

$$N(s) = \frac{1}{b_1 s + b_0}, \tag{2.11}$$

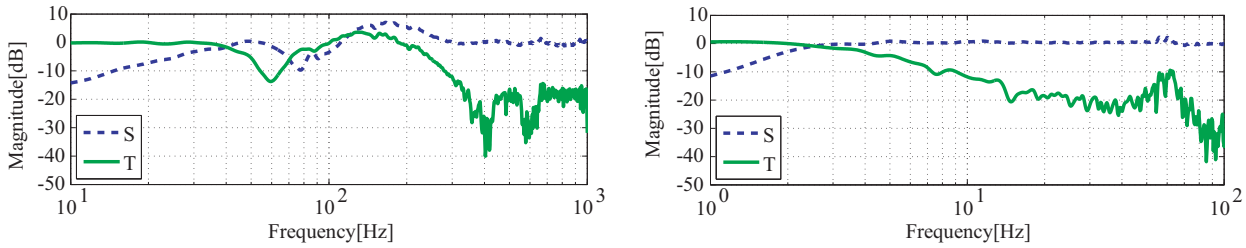

(a) Velocity loop (ω/ω_{ref}) (b) Position loop + Velocity loop (y/y_{ref})

Figure 2.9: Frequency responses of closed loop.

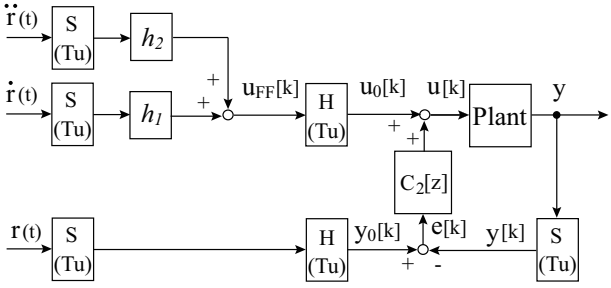

Figure 2.10: Conventional control system.

from (2.5). The feedforward input $u_0[k]$ can be given by the desired position trajectory $y_0(t)$. Here, $x^{(n)}$ is n order derivative of x. When the feedforward controller is implemented, $N(s)$ is discretized by Tustin transformation so that the discrete controller $N[z]$ is obtained.

Next, the nominal rotational velocity ω_0 is generated to be compared with the rotational velocity ω in the rotational velocity loop. The rotational plant model of (2.6) from input u to rotational velocity ω is discretized by zero-order hold so that the discrete rotational plant model $P_\omega[z]$ is obtained. The nominal rotational velocity ω_0 is represented by

$$\omega_0[k] = P_{\omega o}[z]u_0[k], \tag{2.12}$$

where, $P_{\omega o}[z]$ is the nominal plant model of $P_\omega[z]$. The singlerate vibration suppression PTC system is shown in Fig. 2.11. The references are fourth derivatives of the target position as shown in Fig. 2.11.

Here, note that the discretization error occurs because of a digital re-design of the feedforward controller $N[z]$ in singlerate vibration suppression PTC. Moreover, [23] indicate that the inverse system of the plant cannot be designed in discrete-time because unstable zero appears in the plant discretized by zero-order hold.

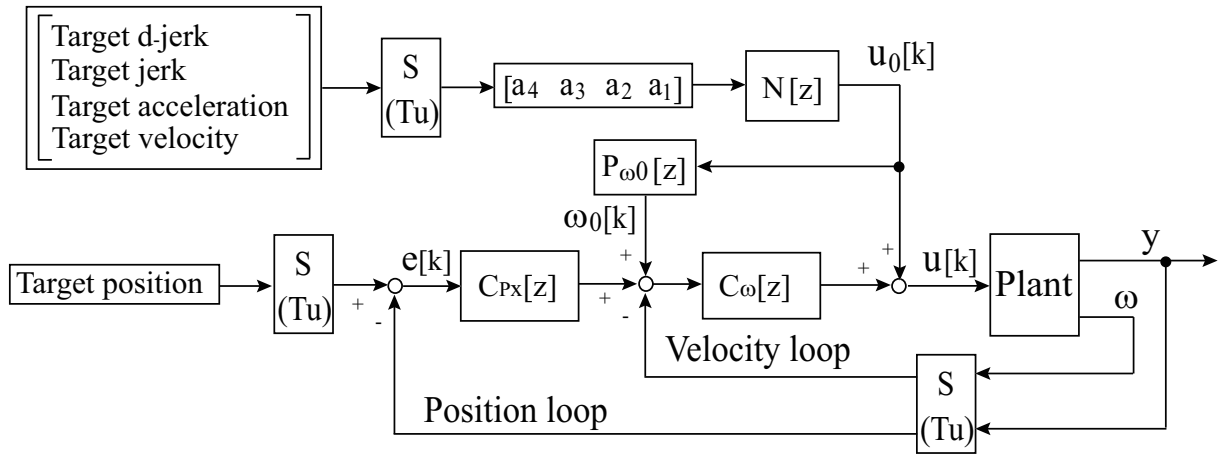

Figure 2.11: Singlerate vibration suppression PTC system (proposed method 1).

2.5.4 Multirate Vibration Suppression PTC

The inverse system of the plant cannot be designed in the singlerate control system as explained in section 2.5.3. Then, It is considered that PTC for two-inertia system model including the resonance mode in the multirate control system explained in section 2.3. The controllable canonical form of (2.5) with state variables $\boldsymbol{x} = [z,\, z^{(1)},\, z^{(2)},\, z^{(3)}]^T$ is represented by (2.14) and (2.15). z is called "virtual position" by [21].

$$\frac{z}{u} = \frac{b_0}{a_4 s^4 + a_3 s^3 + a_2 s^2 + a_1 s} \tag{2.13}$$

$$\dot{\boldsymbol{x}}(t) = \boldsymbol{A}_c \boldsymbol{x}(t) + \boldsymbol{b}_c u(t)\ ,\ y(t) = \boldsymbol{c}_c \boldsymbol{x}(t) \tag{2.14}$$

$$\left[\begin{array}{c|c} \boldsymbol{A}_c & \boldsymbol{b}_c \\ \hline \boldsymbol{c}_c & 0 \end{array}\right] = \left[\begin{array}{cccc|c} 0 & 1 & 0 & 0 & 0 \\ 0 & 0 & 1 & 0 & 0 \\ 0 & 0 & 0 & 1 & 0 \\ 0 & -\frac{a_1}{a_4} & -\frac{a_2}{a_4} & -\frac{a_3}{a_4} & \frac{b_0}{a_4} \\ \hline 1 & \frac{b_1}{b_0} & 0 & 0 & 0 \end{array}\right] \tag{2.15}$$

The discrete-time state equation (2.1) with zero-order hold is discretized with the sampling period T_u. Here, each sampling period is defined as $T_u = T_y = T_r/4$. Therefore, the multirate feedforward controller is obtained by (2.2).

The desired trajectories are given to all state variables $\boldsymbol{x}_d = [z_d,\, z_d^{(1)},\, z_d^{(2)},\, z_d^{(3)}]^T$. However, the state variables cannot be given directly as references because the virtual position z is not the real position y. The state variable $\boldsymbol{x}_d(t)$ is obtained from the target trajectory $\boldsymbol{r}_d(t)$ $= [y_d,\, y_d^{(1)},\, y_d^{(2)},\, y_d^{(3)}]^T(t)$. The transfer function from the translational position P_x to the state variable z is represented by

$$\frac{z}{y} = \frac{b_0}{b_1 s + b_0}, \tag{2.16}$$

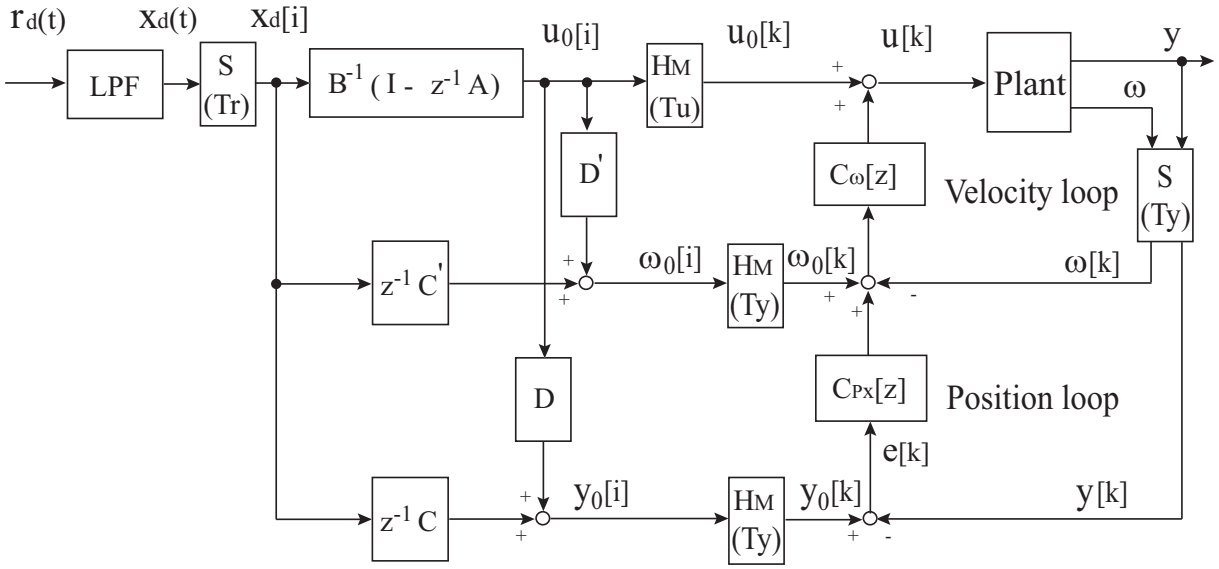

Figure 2.12: Multirate vibration suppression PTC system (proposed method 2).

from (2.5) and (2.13). Therefore, z_d can be obtained from y_d by inserting the LPF before the input of the references. The LPF is discretized by Tustin transformation in the case that the sampling period T_r is much shorter than the time constant of the LPF. On the other hand, the convolution of time function of the target trajectoy and time function of the LPF is calculated by off-line and it is saved in the memory table in the case that the discretization error is caused.

Moreover, to generate the nominal rotational velocity ω_0, the rotational plant model P_ω of (2.6) does not need to be inserted in multirate vibration suppression PTC. The state equation of (2.6) coincides with (2.15) if matrix $\boldsymbol{c}_c$ is only changed as

$$\boldsymbol{c}_c' = \left[\begin{array}{cccc} 0 & \frac{b_{\omega 1}}{b_0} & \frac{b_{\omega 2}}{b_0} & \frac{b_{\omega 3}}{b_0} \end{array} \right]. \tag{2.17}$$

It only has to design the matrices $\boldsymbol{C}$ and $\boldsymbol{D}$ of (2.2) to generate the nominal rotational velocity ω_0. These are defined as $\boldsymbol{C}'$ and $\boldsymbol{D}'$.

Therefore, the multirate vibration suppression PTC can be designed as shown in Fig. 2.12. The PTC system with cascade feedback for a servo motor was proposed by [25]. Note that the feedback controllers work only when errors between the nominal output and the actual output are caused by disturbances or modeling errors.

2.5.5 Disturbance Observer Design

The input disturbance by the nonlinear friction of the ball screw is regarded as step-type disturbace. The full-order state observer is designed in discrete-time to estimate and to

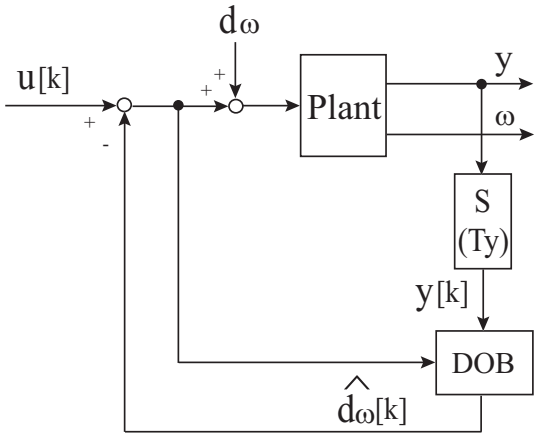

Figure 2.13: Plant with disturbance observer.

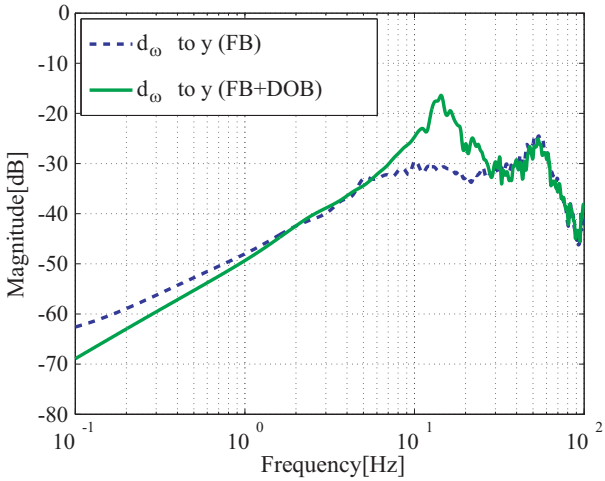

Figure 2.14: Frequency responses of disturbance suppression.

suppress the disturbance. The discrete state equation of the augmented plant is represented by

$$\boldsymbol{x}_e[k+1] = \boldsymbol{A}_f \boldsymbol{x}_e[k] + \boldsymbol{b}_f u[k] \ , \ y[k] = \boldsymbol{c}_f \boldsymbol{x}_e[k], \tag{2.18}$$

with the state variables $\boldsymbol{x}_e = [\omega,\ \theta,\ v_x,\ P_x,\ d_\omega]^T$ added input disturbance d_ω. The full-order state observer can be designed as

$$\hat{\boldsymbol{x}}_e[k+1] = (\boldsymbol{A}_f - \boldsymbol{H}_f \boldsymbol{c}_f)\hat{\boldsymbol{x}}_e[k] + \boldsymbol{b}_f u[k] + \boldsymbol{H}_f y[k] \tag{2.19}$$

$$\hat{\boldsymbol{x}}_e[k] = [\hat{\omega}[k] \quad \hat{\theta}[k] \quad \hat{v}_x[k] \quad \hat{P}_x[k] \quad \hat{d}_\omega[k]]^T. \tag{2.20}$$

The observer gain $\boldsymbol{H}_f$ is designed so that observer poles are located at 100 Hz. Here, estimated disturbance $\hat{d}_\omega$ is subtracted from input u to suppress the disturbance d_ω as shown in Fig. 2.13. The frequency responses of the disturbance suppression are shown in Fig. 2.14. The disturbance suppression is improved in the low frequency band below 1 Hz by the disturbance observer.

2.6 Simulations of Step Stage

The tracking responses of the feedforward controller of each control system are compared in the case that the plant model is nominal. Each sampling period is $T_u = T_y = T_r/4 = 1/6$ ms. The target position trajectory was generated by sixth-order polynomial equation. The specification of the target position trajectory is shown in Table 2.1, where the target position is A^{ref}, the acceleration time is t_{acc}, the constant velocity time is t_{con}, the decelerating time is t_{dec}, and the positioning time is t_d $(= t_{acc} + t_{con} + t_{dec})$. The target positional trajectory

Table 2.1: Specifications of target trajectory.

A^{ref}	t_{acc}	t_{con}	t_{dec}	t_d
0.1 m	0.25 s	0.0 s	0.25 s	0.5 s

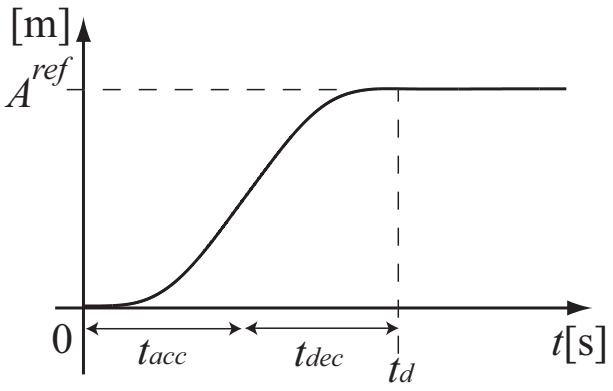

Figure 2.15: Target trajectory of step stage.

is shown in Fig. 2.15. The target velocity and acceleration and jerk trajectories are given by derivation of the target position trajectory.

The target specification is the tracking error tolerance 0.5 μm in the positional settling time 150 ms. Here, the positional settling time is the time in which the tracking error converges in the tolerance after the positioning time t_d.

The nominal simulation results of the comparison only with the feedforward controller are shown in Fig. 2.16. After 0.5 s, the tracking error of the singlerate vibration suppression PTC is over 0.5 μm by the influence of the discretization error of the feedforward controller. On the other hand, the tracking error of the multirate vibration suppression PTC is perfectly zero at sampling points.

2.7 Experiments of Step Stage

The tracking response of each control system is compared in the actual experiment. The sampling periods and the target trajectories are the same as those of the simulation. Moreover, the disturbance observer is implemented in the experiment. The experimantal results are shown in Fig. 2.17. The tracking errors of five time experiments are overwritten for the confirmation of reproducibility. The tracking error tolerance 0.5 μm was achieved over the positional settling time 200 ms in the singlerate vibration suppression PTC. On the other hand, the tracking error tolerance 0.5 μm was achieved in the positional settling time 15 ms

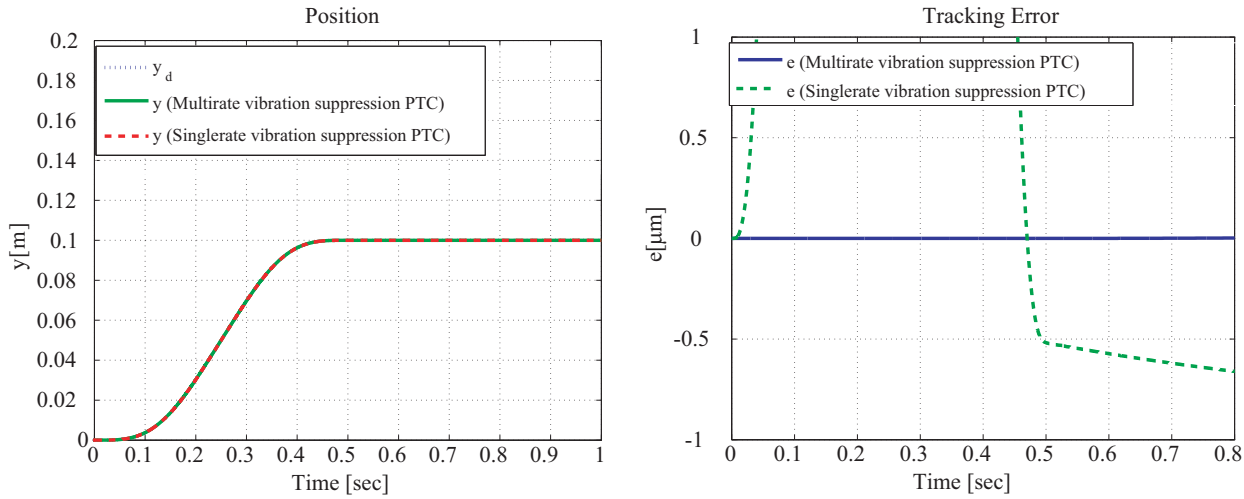

(a) Position response

(b) Tracking error

Figure 2.16: Nominal simulation results (only with feedforward controller).

in the multirate vibration suppression PTC.

2.8 Experiments of Gantry Stage

Each sampling period of the controller is $T_y = T_u = 1/3$ ms, which is the same as the actual controller.

For the proposed feedforward controller, the target position trajectory is given. In addition, the target velocity, acceleration, and jerk trajectories are given by differentiating target position trajectory. Fig. 2.18 shows target position and velocity trajectories. Here, t_{acc} is the time between the beginning of acceleration and the point where the acceleration becomes zero. In other words, it is the time taken for the velocity to become constant. Then, the constant velocity is defined as v_{const}. After the time of the end of t_{acc}, v_{const} does not change. The settling time t_{set} is the time it takes for a tracking error to be within a desired range s_{range}. The total time t_{total} is represented by

$$t_{total} = t_{acc} + t_{set}. \tag{2.21}$$

t_{set} and t_{total} are very important specification for the high-speed and high-precision tracking stage because t_{set} and t_{total} should be shortened as much as possible to improve throughput.

The specifications of the target trajectory and the settling range s_{range} are shown in Table 2.2(a). This value of the s_{range} indicates that the precision is on the order of sub-micron.

The frequency responses of the position loop are shown in Fig. 2.19. The time responses are shown in Fig. 2.20.

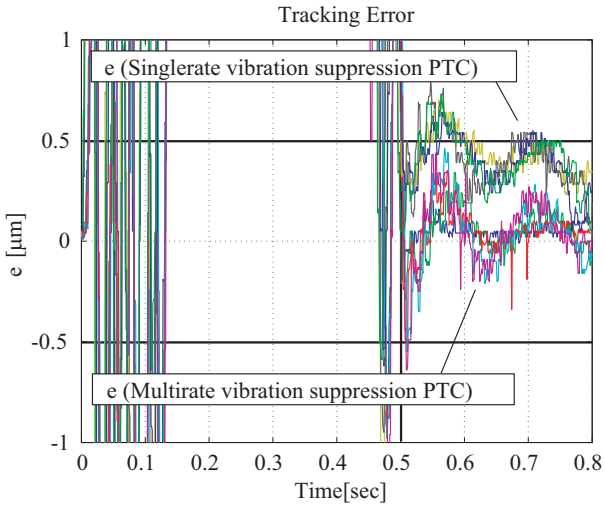

Figure 2.17: Experimental results.

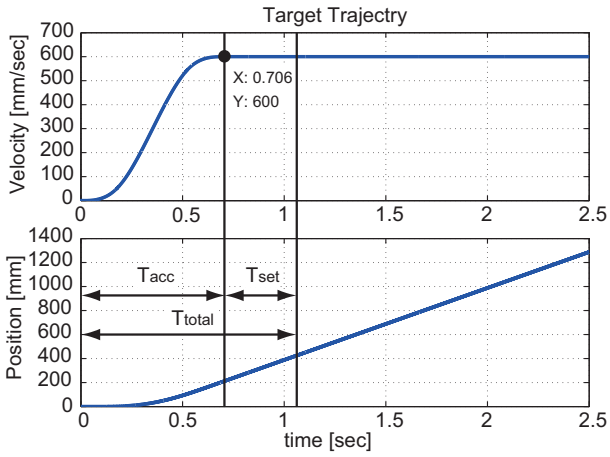

Figure 2.18: Target trajectories of gantry stage.

The error of the conventional method is below 6×10^4 count. However, the error of the proposed method is only 1×10^3 count. Furthermore, t_{set} and t_{total} were shortened as shown in Table 2.2(b).

2.9 Improvement of Feedback Controller of Step Stage

The conventional feedback system was designed by the traditional double loop controller with fine-tuning. Since it is not very theoretical and systematic, the feedback performance has to depend on tuning of engineers. Then, a feedback controller which consists of the observer and the regulator is applied to improve the feedback system.

In order to regulate the plant state and reject the disturbance, the regulator is designed

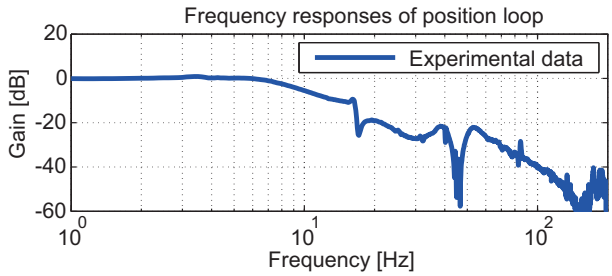

Figure 2.19: Frequency responses of position loop.

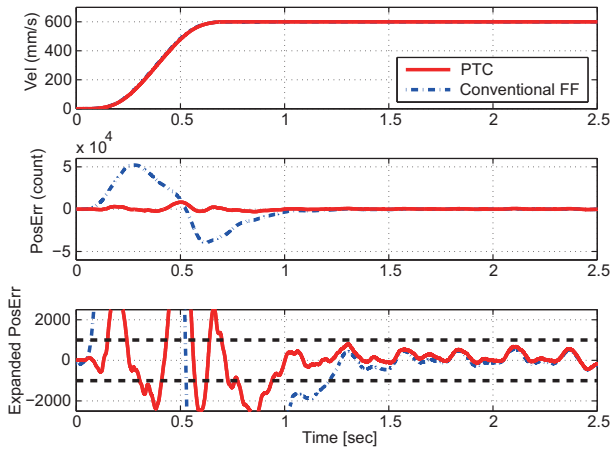

Figure 2.20: Experimental results of time response.

by

$$u[k] = \boldsymbol{F}\hat{\boldsymbol{x}}_e[k] = \boldsymbol{F}_p\hat{\boldsymbol{x}}_p[k] + F_d\hat{x}_d[k], \tag{2.22}$$

where the states $\hat{\boldsymbol{x}}_p[k] = [\hat{\omega}[k] \;\; \hat{\theta}[k] \;\; \hat{v}_x[k] \;\; \hat{P}_x[k]]^T$, $\hat{x}_d[k] = \hat{d}_\omega[k]$ and the state feedback gain $\boldsymbol{F} = [\boldsymbol{F}_p \;\; F_d]$. The feedback type controller which consists of the observer and the regulator is obtained by

$$u[k] = \left[\begin{array}{c|c} \boldsymbol{A}_f - \boldsymbol{H}_f\boldsymbol{c}_f + \boldsymbol{b}_f\boldsymbol{F} & \boldsymbol{H}_f \\ \hline \boldsymbol{F} & 0 \end{array}\right] y[k], \tag{2.23}$$

with (2.20) and (2.22). Therefore, the feedback controller can be applied in PTC system shown in Fig. 2.1 as

$$\begin{aligned} u[k] &= C_2[z](y_o[k] - y[k]) \\ &= C_2[z]e[k] \\ &= \left[\begin{array}{c|c} \boldsymbol{A}_f - \boldsymbol{H}_f\boldsymbol{c}_f + \boldsymbol{b}_f\boldsymbol{F} & -\boldsymbol{H}_f \\ \hline \boldsymbol{F} & 0 \end{array}\right] e[k]. \end{aligned} \tag{2.24}$$

Table 2.2: Specification of experiment of gantry stage

(a) Specification of target trajectory and settling range

v_{const} [mm/s]	t_{acc} [sec]	s_{range} [count]
600	0.706	$\pm$1000

(b) Experimental results of t_{set} and t_{total}

Method	t_{set} [sec]	t_{total} [sec]
Conventional	0.6	1.3
Proposed	0.3	1.0

The feedback controller can be designed systematically in comparison with the conventional feedback controller.

Frequency responses of one design example are shown in Fig. 2.21 and 2.22. The observer and the regulator are designed by pole placement to suppress the resonance mode of the plant. The figures show that the bandwidth and the disturbance suppression performance are extremely improved in comparison with the conventional feedback controller because the proposed controller is designed with considering resonance mode of the plant.

The experimental results of the time responses of the conventional feedback and the proposed feedback are shown in Fig. 2.23. The target trajectory values are the same as those of the simulation in Table 2.1. In the experiment of Fig. 2.17, the multirate feedforward controller is sufficiently adjusted. In the experiment of Fig. 2.23, however, the multirate feedforward controller is not very adjusted.

The tracking error in the acceleration and deceleration time ($0 \sim 0.5$ sec) is dramatically suppressed in Fig. 2.23(a) and (c) because of the high bandwidth of the feedback system. However, the positional settling time is not shortened. It seems that the reason for the result is a nonlinear characteristic of the ball screw. The group of balls rolls over linearly in the acceleration and deceleration time. The group of balls acts as a non-linear spring in the positional settling time because this does not roll over. Therefore, if the high bandwidth of the feedback system is achieved, the feedback performance is not always brought out in the positional settling time.

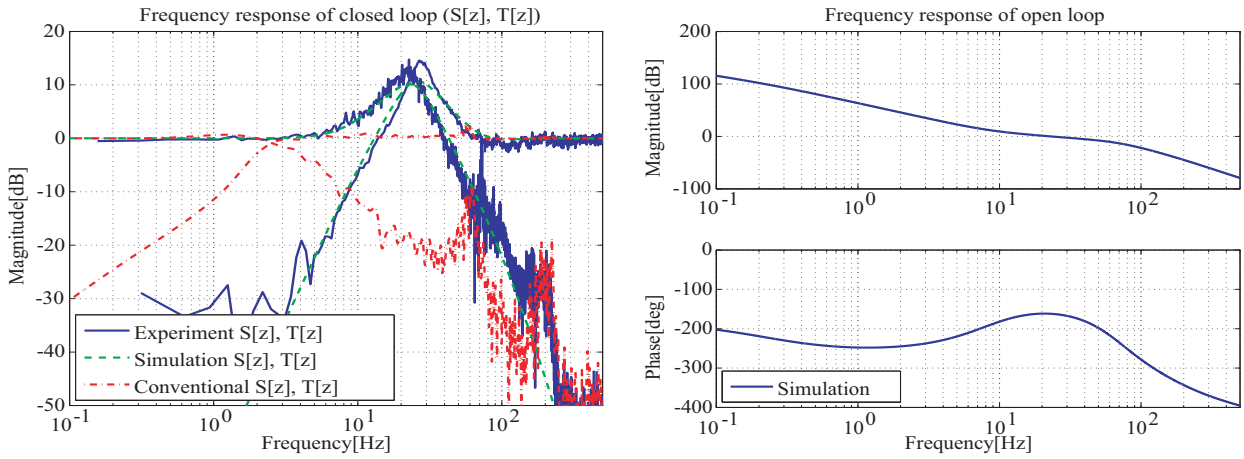

(a) Closed loop (b) Open loop

Figure 2.21: Frequency responses (Improvement).

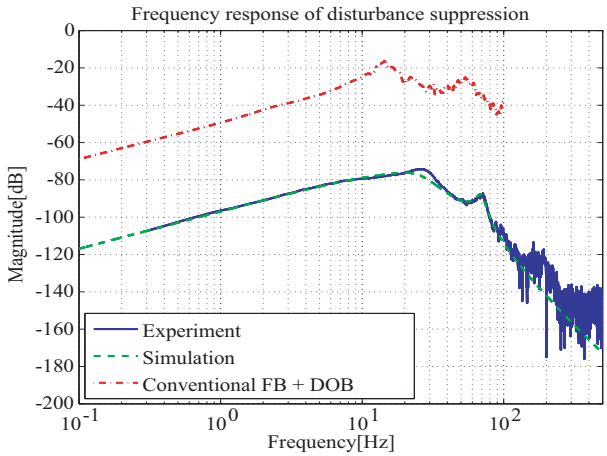

Figure 2.22: Frequency response of disturbance suppression (Improvement).

2.10 Summary

Vibration suppression PTC (VSPTC) was applied for fast and precise positioning of the two types of large-scale high-precision stages which are the step stage and gantry stage. It was shown that the control performance can be improved by VSPTC in simulations and experiments. Moreover, the improvement of feedback controller which can be designed systematically was shown. The transient response of the positioning is dramatically improved by the feedback controller.

In section 2.9, it is regarded that the feedback controllers suppress variation of viscosity and nonlinear friction caused by the ball screw. Iwasaki et al. [26] proposed a modeling of the nonlinear friction. Higher precise positioning can be expected by the feedforward

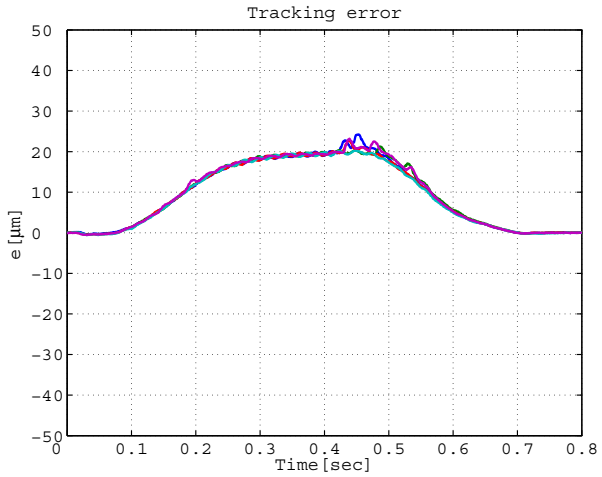

(a) Conventional FB

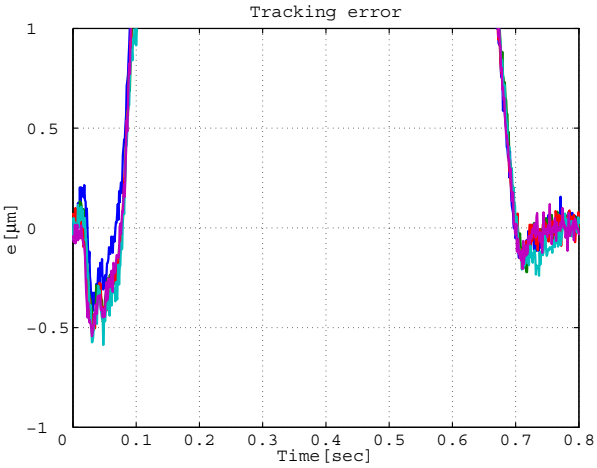

(b) Conventional FB (expanded)

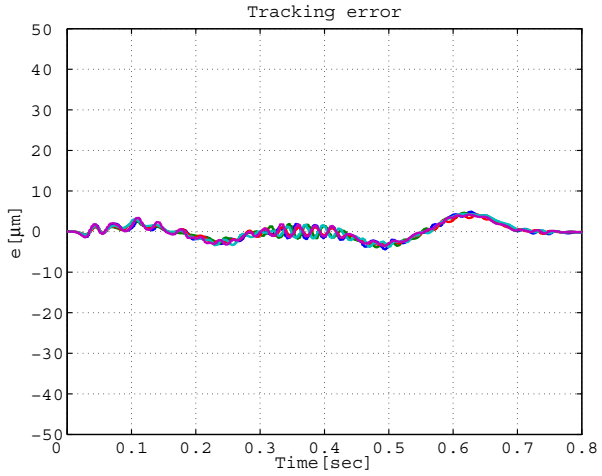

(c) Proposed FB

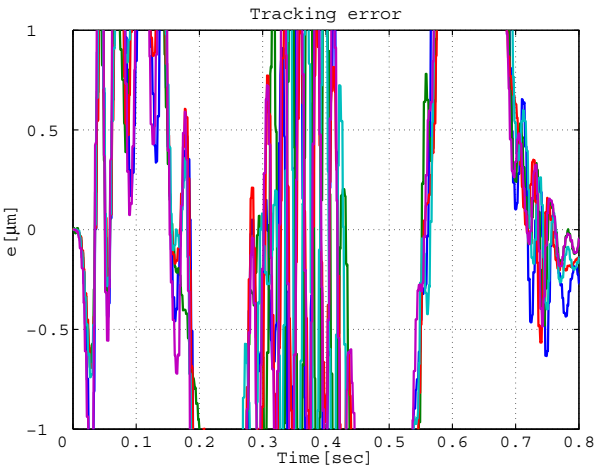

(d) Proposed FB (expanded)

Figure 2.23: Experimental results of time response (Improvement).

compensation of the nonlinear friction.

Chapter 3

Synchronous Position Control based on Multirate Control

3.1 Abstract

A synchronous position control system based on master-slave method is often required in industrial equipment, for example, NC machine tools, exposure systems, and so on. The authors' research group has achieved precise positioning whose error tolerance is in sub-micrometer range for a large-scaled high-precision stage with perfect tracking control (PTC). In this chapter, a novel synchronous position control system is proposed for a pair of precision stages based on multirate control and dead-time compensation. Finally, simulations and experiments with experimental precision stages are performed to show the advantages of the proposed control system.

3.2 Introduction

The synchronous position control method for multi servo systems is divided into two main classes. One is the method in which dynamic and response characteristics of each servo system are matched and the references of each servo system are put out in synchronization. However, it is difficult to match the control characteristic of each servo system perfectly. Moreover, it is impossible to synchronize positions of each system precisely. The other is master-slave method in which the output of one servo system with slow response characteristic (Master) is the reference of the other servo system with fast response characteristic (Slave). In this method, designing 2-degrees of freedom control system for Slave, the synchronous position control system is achieved more precisely [27].

A synchronous position control system based on a master-slave method is often required in industrial equipment, for example, NC machine tools, exposure systems, and so on [28].

The author's research group has achieved precise positioning whose error tolerance is in sub-micrometer range for a large-scaled high-precision stage with perfect tracking control (PTC) [20], [29] and [38].

In this chapter, a synchronous position control system for two precision stages is proposed. Then, it is assumed that PTC which is explained in next section has been designed for each precision stage. The control system can synchronize two nominal precision stages perfectly. However, there are not only disturbances but also dead-times in the system. These obstacles influence the synchronization accuracy. The proposed synchronous position control system can be more robust to the disturbance of master stage and plant variations by applying an observer which compensates dead-times [30] in the system. Finally, simulations and experiments with experimental precision stages are performed to show the advantages of the proposed control system.

3.3 Constitution of Synchronous Position Systems

Control sampling periods are defined as T_{um} and T_{us}. Output sampling periods are defined as T_{ym} and T_{ys}. Plant orders are defined as n_m and n_s. Here, the subscript m represents Master, and the subscript s represents Slave. PTC has been designed for both master and slave stage. Each constitution of synchronous position system is explained as follows.

3.3.1 Ver. 1: Real Position FB

The control system in which the real position of Master is fed back is a general master-slave control system as shown in Fig. 3.1(a). However, in this constitution, the tracking accuracy depends on the feedback controller performance of Slave. The constitution in Fig. 3.1(a) is not adapted for high-speed and high-precise synchronous control.

3.3.2 Ver. 2: Independent PTC

In Fig. 3.1(b), both Master and Slave are controlled by PTC, and are given same references. The system can achieve the syncronization between Master and Slave perfectly if the plant is nominal. However, disturbances or plant variations influence the tracking accuracy directly.

3.3.3 Ver. 3: Real Position FB + PTC

In Fig. 3.1(c), above two methods are combined. The system can achieve the syncronization between Master and Slave perfectly if the plant is nominal. Moreover, the system can be robust to the disturbance of master stage and plant variations because the real position of

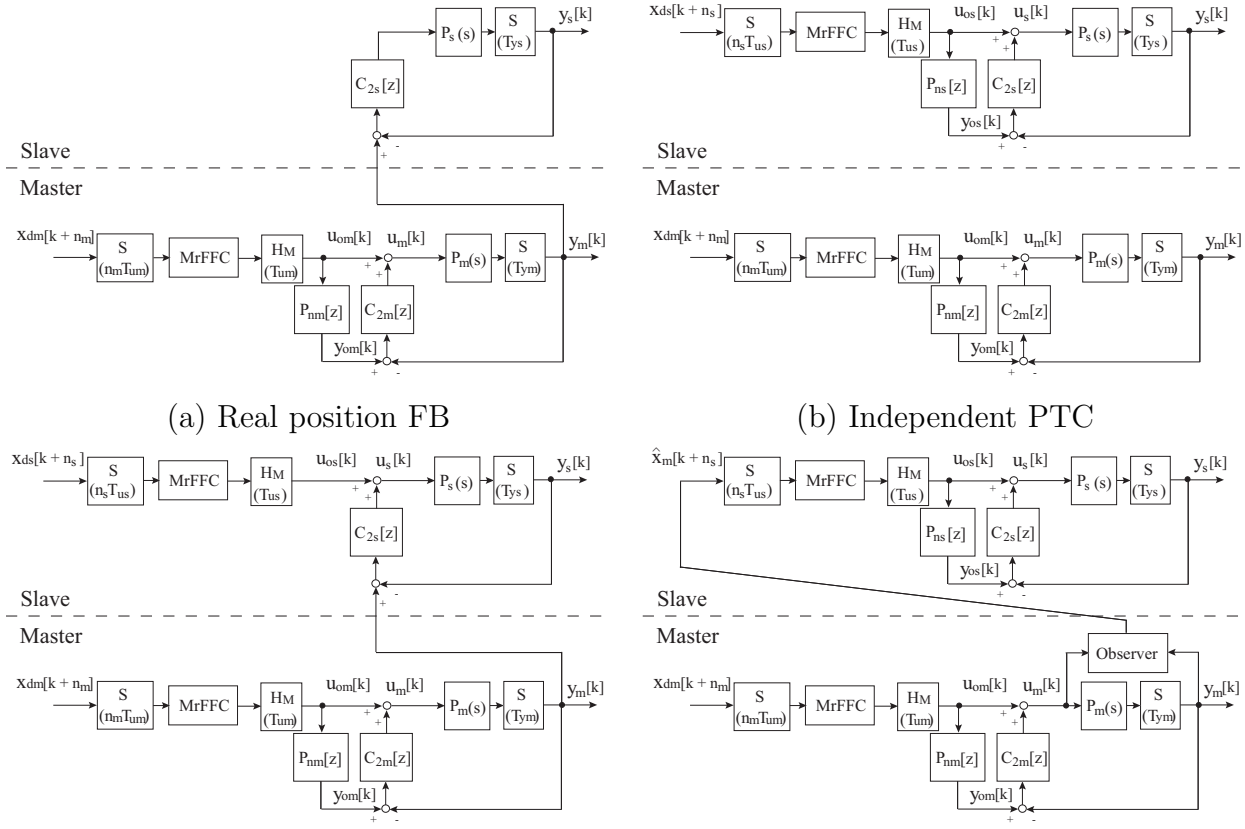

(a) Real position FB

(b) Independent PTC

(c) Real position FB + PTC

(d) Proposed system

Figure 3.1: Synchronous position systems.

Master is fed back. Though the system is adapted for an ideal system without dead-times, dead-times of the system influence the tracking accuracy in a real system.

3.3.4 Ver. 4: Observer Compensating Dead-times (Proposed)

Therefore, the system with an observer considering dead-times of the system is proposed. the proposed system is shown in Fig. 3.1(d). Since the state variables (position, velocity, $\cdots$) n_s sample ahead of Master are given to the references of PTC per n_s sampling period in Slave, the system can be more robust to the disturbance of master stage and plant variations. The key point of the control system is how to estimate the state variables n_s sample ahead of Master with the observer.

3.4 Consideration of Dead-time

The class of the problem is assumed as $T_{um} = T_{us} = T_{ym} = T_{ys} = T_u = T_y$ easily though many various cases are considered about sampling periods of Master and Slave. Dead-times

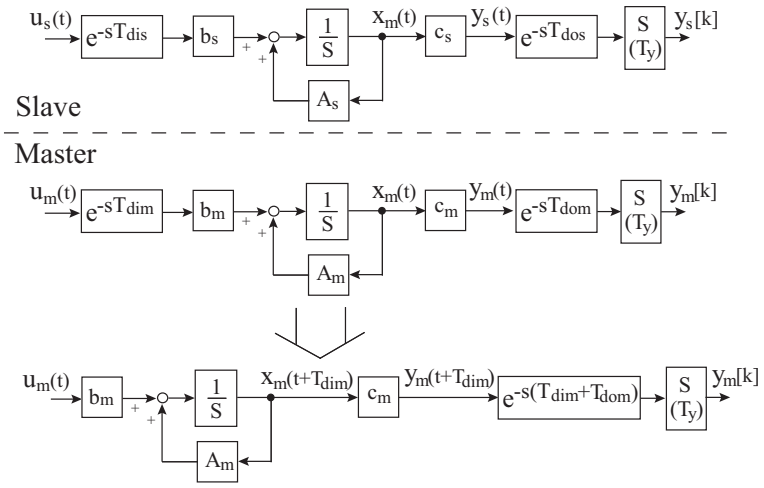

Figure 3.2: Plant with dead-times.

which occur in Master and Slave are discussed.

Dead-times which occur in the plants are defined as T_{dim} and T_{dis}. Dead-times which occur in the sensors are defined as T_{dom} and T_{dos} as a delay exists in the output. Fig. 3.2 shows the plant with dead-times. Here, the state $\boldsymbol{x}_m(kT_y + T_{dim})$ of Master can be estimated at a time kT_y because the dead-times of Master are summed up in the output of Master as shown in Fig. 3.2. Since the state $\boldsymbol{x}_m(kT_y + n_s T_u + T_{dis})$ of Master is needed to synchronize the real position $y_s(t)$ of Slave and the real position $y_m(t)$ of Master, the estimated state $\hat{\boldsymbol{x}}_m(kT_y + T_{dim})$ has to be stepped for $n_s T_u + T_{dis} - T_{dim}$ periods moreover.

3.4.1 Definition of State Equations of Plants

The continuous time state equation of the plant of Master except dead-times is represented by

$$\begin{cases} \dot{\boldsymbol{x}}_{pm}(t) = \boldsymbol{A}_{cpm}\boldsymbol{x}_{pm}(t) + \boldsymbol{b}_{cpm}(u_m(t) - d_m(t)) \\ y_m(t) = \boldsymbol{c}_{cpm}\boldsymbol{x}_{pm}(t) \end{cases}, \tag{3.1}$$

as a controllable canonical form. The continuous time state equation of the disturbance of Master is represented by

$$\begin{cases} \dot{\boldsymbol{x}}_{dm}(t) = \boldsymbol{A}_{cdm}\boldsymbol{x}_{dm}(t) \\ d_m(t) = \boldsymbol{c}_{cdm}\boldsymbol{x}_{dm}(t) \end{cases}. \tag{3.2}$$

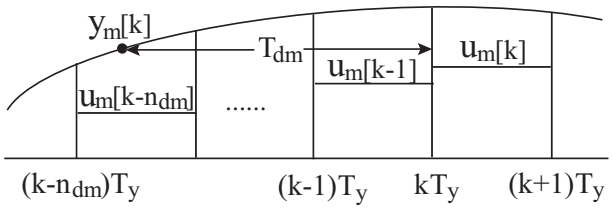

Figure 3.3: Time chart of dead-time.

The augmented continuous time state equation of Master can be represented by

$$\begin{cases} \dot{\boldsymbol{x}}_m(t) = \boldsymbol{A}_{cm}\boldsymbol{x}_m(t) + \boldsymbol{b}_{cm}u_m(t) \\ y_m(t) = \boldsymbol{c}_{cm}\boldsymbol{x}_m(t) \end{cases}, \tag{3.3}$$

$$\left[\begin{array}{c|c} \boldsymbol{A}_{cm} & \boldsymbol{b}_{cm} \\ \hline \boldsymbol{c}_{cm} & \boldsymbol{0} \end{array}\right] \triangleq \left[\begin{array}{cc|c} \boldsymbol{A}_{cpm} & -\boldsymbol{b}_{cpm}\boldsymbol{c}_{cdm} & \boldsymbol{b}_{cpm} \\ \boldsymbol{0} & \boldsymbol{A}_{cdm} & \boldsymbol{0} \\ \hline \boldsymbol{c}_{cpm} & \boldsymbol{0} & \boldsymbol{0} \end{array}\right], \tag{3.4}$$

where $\boldsymbol{x}_m = [\boldsymbol{x}_{pm}, \boldsymbol{x}_{dm}]^T$. Then, the augmented discrete time state equation of (3.3) per T_u is represented by

$$\begin{cases} \boldsymbol{x}_m[k+1] = \boldsymbol{A}_{zm}\boldsymbol{x}_m[k] + \boldsymbol{b}_{zm}u_m[k] \\ y_m[k] = \boldsymbol{c}_{zm}\boldsymbol{x}_m[k] \end{cases}. \tag{3.5}$$

In Slave, these equations are defined similarly as the subscript m is changed into s.

3.4.2 Estimation of States of Master

The dead-time of Master summed up in the output of Master is defined as

$$T_{dm} = T_{dim} + T_{dom}. \tag{3.6}$$

Thus, the output of Master delays for the dead-time T_{dm} as Fig. 3.3.

Here, the state $\boldsymbol{x}_m(kT_y + T_{dim})$ of Master at the time kT_y is estimated as the state $\hat{\boldsymbol{x}}_m[k]$ by an observer.

In the case of $T_{dm} = 0$

The state $\boldsymbol{x}_m[k]$ of the plant of Master can be estimated by the general observer as

$$\hat{\boldsymbol{x}}_m[k] = \boldsymbol{A}_{zm}\hat{\boldsymbol{x}}_m[k-1] + \boldsymbol{b}_{zm}u_m[k-1] + \boldsymbol{H}(y_m[k-1] - \boldsymbol{c}_{zm}\hat{\boldsymbol{x}}_m[k-1]), \tag{3.7}$$

$$\begin{aligned} \boldsymbol{e}_m[k] &= \boldsymbol{x}_m[k] - \hat{\boldsymbol{x}}_m[k] \\ &= (\boldsymbol{A}_{zm} - \boldsymbol{H}\boldsymbol{c}_{zm})\boldsymbol{e}_m[k-1]. \end{aligned} \tag{3.8}$$

In the case of $(n_{dm}-1)T_y < T_{dm} \leq n_{dm}T_y \quad (n_{dm} = 1, 2, \cdots)$

At the time kT_u, the available output signal $y_m[k]$ is represented by

$$
\begin{aligned}
y_m[k] &= \boldsymbol{c}_{dm}\boldsymbol{x}_m[k-n_{dm}] + \boldsymbol{d}_{dm}u_m[k-n_{dm}], && (3.9)\\
\boldsymbol{c}_{dm} &= \boldsymbol{c}_{cm}e^{\boldsymbol{A}_{cm}(n_{dm}T_y - T_{dm})}, && (3.10)\\
\boldsymbol{d}_{dm} &= \int_0^{n_{dm}T_y - T_{dm}} \boldsymbol{c}_{cm}e^{\boldsymbol{A}_{cm}\tau}\boldsymbol{b}_{cm}d\tau. && (3.11)
\end{aligned}
$$

The state $\boldsymbol{x}_m[k]$ of the plant of Master can be estimated by the equation as follows:

$$
\begin{aligned}
\hat{\boldsymbol{x}}_m[k] &= \boldsymbol{A}_{zm}^{n_{dm}}\hat{\boldsymbol{x}}_m[k-n_{dm}] + [\boldsymbol{A}_{zm}^{n_{dm}-1}\boldsymbol{b}_{zm}, \boldsymbol{A}_{zm}^{n_{dm}-2}\boldsymbol{b}_{zm}, \cdots, \boldsymbol{b}_{zm}]\begin{bmatrix} u_m[k-n_{dm}] \\ \vdots \\ u_m[k-1] \end{bmatrix}\\
&\quad + \boldsymbol{A}_{zm}^{n_{dm}-1}\boldsymbol{H}(y_m[k] - \boldsymbol{c}_{dm}\hat{\boldsymbol{x}}_m[k-n_{dm}] - \boldsymbol{d}_{dm}u_m[k-n_{dm}]), && (3.12)\\
&\quad \boldsymbol{e}_m[k] = (\boldsymbol{A}_{zm}^{n_{dm}} - \boldsymbol{A}_{zm}^{n_{dm}-1}\boldsymbol{H}\boldsymbol{c}_{dm})\boldsymbol{e}_m[k-n_{dm}]. && (3.13)
\end{aligned}
$$

3.4.3 Generation of References for Slave

Since the state $\hat{\boldsymbol{x}}_m[k]$ of Master at kT_y has been estimated, the state $\hat{\boldsymbol{x}}_m[i+N+\sigma]$ which is stepped $n_sT_y + T_{dis} - T_{dim}$ periods ahead is to be estimated per n_s periods. Here, $[i] = (i \cdot n_sT_y)$, $N = 0, 1, \cdots$ and $0 \leq \sigma < 1$.

In the case that $n_sT_y + T_{dis} - T_{dim} < 0$, $\hat{\boldsymbol{x}}_m[k]$ has only to be delayed for this period.

In the case that $n_sT_y + T_{dis} - T_{dim} \geq 0$, the state $\hat{\boldsymbol{x}}_m[i+N+\sigma]$ is estimated as

$$
\begin{aligned}
&\hat{\boldsymbol{x}}_m[i+n_s+\sigma] = \boldsymbol{A}_{dm}\hat{\boldsymbol{x}}_m[i] + \boldsymbol{B}_{dm}\boldsymbol{u}_m[i], && (3.14)\\
&\boldsymbol{A}_{dm} = e^{\boldsymbol{A}_{cm}(N+\sigma)T_y}, && (3.15)\\
&\boldsymbol{B}_{dm} = [\boldsymbol{b}_{dm1}, \cdots, \boldsymbol{b}_{dmN}, \boldsymbol{b}_{dm(N+1)}], && (3.16)\\
&\boldsymbol{u}_m[i] = [u_{m1}, \cdots, u_{mN}, u_{m(N+1)}]^T[i], && (3.17)
\end{aligned}
$$

where,

$$
\begin{cases}
\boldsymbol{b}_{dmj} = \boldsymbol{A}_{zm}^{j-1}\boldsymbol{b}_{zm} \quad (j \leq N) \\
\boldsymbol{b}_{dm(N+1)} = \int_0^{\sigma T_y} e^{\boldsymbol{A}_{cm}\tau}\boldsymbol{b}_{cm}d\tau
\end{cases}, \qquad (3.18)
$$

$$
\begin{cases}
u_{m1} = u_m[k] \\
u_{mj} = u_{om}[k+j-1] \quad (2 \leq j \leq N+1)
\end{cases}. \qquad (3.19)
$$

Here, u_{om} represents a nominal input calculated by the multirate feedforward controller previously.

Thus, the elements of the state $\hat{\boldsymbol{x}}_m[i+N+\sigma]$ from first to n_mth are obtained as the references for Slave, where $n_s \leq n_m$.

3.5 Experimental Precision Stages

Fig. 3.4 shows the experimental precision stages applied in the synchronous control. The stage which consists of the AC-motor and the ball-screw in Fig. 3.4(a) is called "Ball-screw stage." The stage which consists of the linear-motor and the air-guide in Fig. 3.4(b) is called "Nano-stage."

Ball-screw stage is identified as Master. Nano-stage is identified as Slave. Frequency responses of the stages are shown in Fig. 3.5(a) and (b).

Each sampling period is

$$T_{um} = T_{us} = T_{ym} = T_{ys} = T_u = T_y = 1 \text{ ms}. \tag{3.20}$$

Each plant is

$$P_m(s) = \frac{b_{pm0}}{s^2 + a_{pm1}s}, \tag{3.21}$$

$$P_s(s) = \frac{b_{ps0}}{s^2 + a_{ps1}s}. \tag{3.22}$$

Both Master and Slave are 2-order plants. Thus,

$$n_m = 2,\ n_s = 2. \tag{3.23}$$

Here, Each state of plants is represented by

$$\boldsymbol{x}_m = [y_m,\ \dot{y}_m]^T, \tag{3.24}$$

$$\boldsymbol{x}_s = [y_s,\ \dot{y}_s]^T. \tag{3.25}$$

Each dead-time which occurs in the system is

$$T_{dim} = T_y,\ T_{dom} = T_{dis} = T_{dos} = 0. \tag{3.26}$$

3.6 Simulations

Each control system is compared by simulations for the models of the experimental precision stages. Both feedback controllers $C_{2m}[z]$ and $C_{2s}[z]$ are constrained as PID controllers. The controller $C_{2m}[z]$ of Master is designed by pole placement as the bandwidth is 30 Hz, and the controller $C_{2s}[z]$ of Slave is designed by pole placement as the bandwidth is 60 Hz. Moreover, the observer gain $\boldsymbol{H}$ is designed as eigenvalues of $(\boldsymbol{A}_{zm}^{n_{dm}} - \boldsymbol{A}_{zm}^{n_{dm}-1}\boldsymbol{H}\boldsymbol{c}_{dm})$ are multiple roots of 100 Hz.

Target trajectories are shown in Fig. 3.6(a). The target position trajectory was generated by the 5th-order polynomial. The specification is shown in Table. 3.1. T_{acc}, T_{con}, T_{dec} and A^{ref} represent the acceleration time, the constant velocity time, the deceleration time and

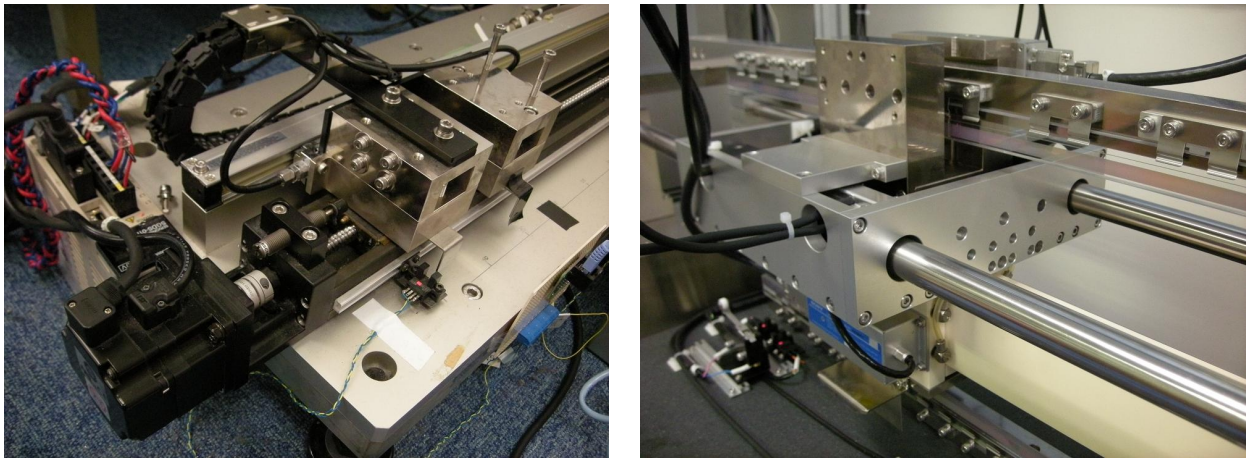

(a) Ball-screw stage (Master) (b) Nano-stage (Slave)

Figure 3.4: Experimental precision stages.

Table 3.1: Specification of target trajectory.

T_{acc}	T_{con}	T_{dec}	A^{ref}
0.2 sec	0.2 sec	0.2 sec	0.04 m

the target position in the trajectory, respectively. Each control system is evaluated by the position error between the real position y_m of Master and the real position y_s of Slave.

Fig. 3.6(b) shows the position error $(y_m - y_s)$ when the plants are nominal. Perfect tracking is achived in each control system except for real position FB.

Next, Fig. 3.6(c) and 3.6(d) show the position error $(y_m - y_s)$ when the input disturbance 0.01 Nm occurs in Master. Comparing with real position FB + PTC, the proposed system is better because the states of Master considering dead-time is obtained as references for Slave faster.

3.7 Experiments

Each control system is compared by experimental precision stages. The specification of target trajectories and controllers is similar to one of the simulation. Experimental results of position error $(y_m - y_s)$ for each control system are shown in Fig. 3.7.

A plant variation occurs in Master because of the non-linear friction characteristic caused by the ball-screw. Therefore, the position error occurs widely in independent PTC not using the output of Master as the input of Slave.

For the same reason, the feedforward controller of Master does not work effectively. How-

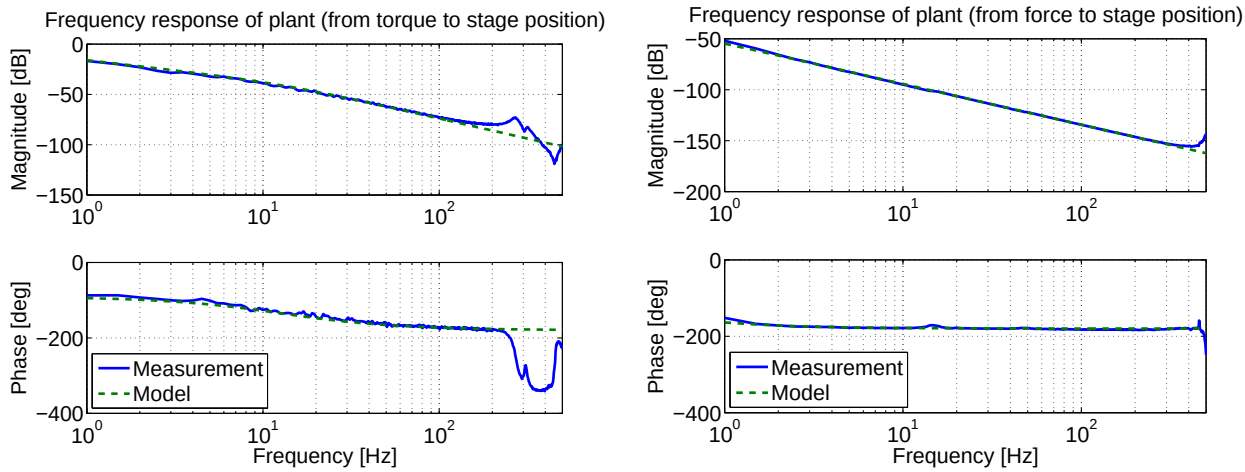

(a) Ball-screw stage (Master) (b) Nano-stage (Slave)

Figure 3.5: Frequency responses of experimental stages.

ever, real position FB + PTC is a little bit better than real position FB in the acceleration and deceleration time.

On the other hand, the proposed system can achieve the precise synchronous positioning. The proposed system can be more robust to the disturbance of master stage and plant variations because the state of Master considering with dead-time is obtained as references for Slave.

3.8 Summary

A synchronous position control system was proposed for a master-slave system required in industrial equipment. The synchronous position control system can be more robust to the disturbance of master stage and plant variations by applying an observer, which compensates dead-times in the system. Simulations and experiments with experimental precision stages are performed to show the advantages of the proposed control system.

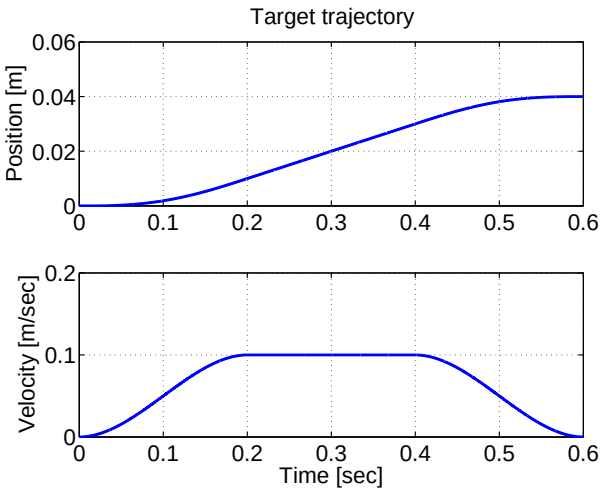

(a) Target trajectories

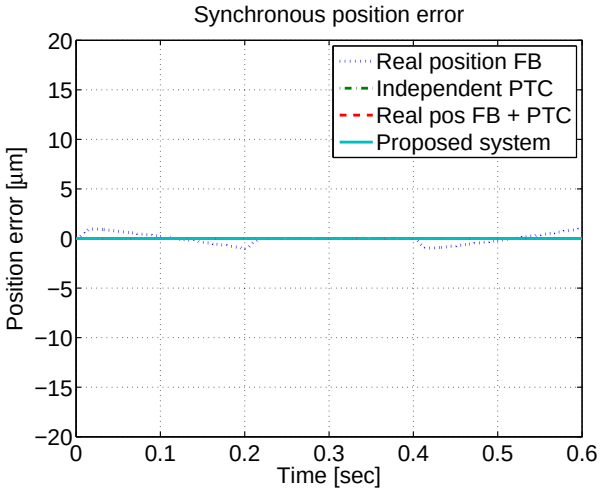

(b) Nominal

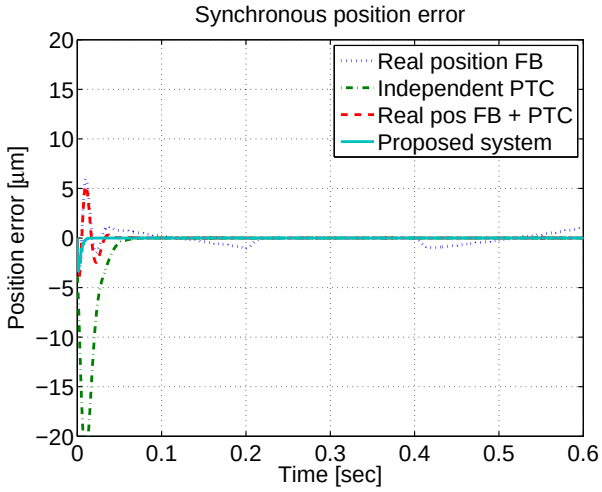

(c) Disturbance 0.01 Nm

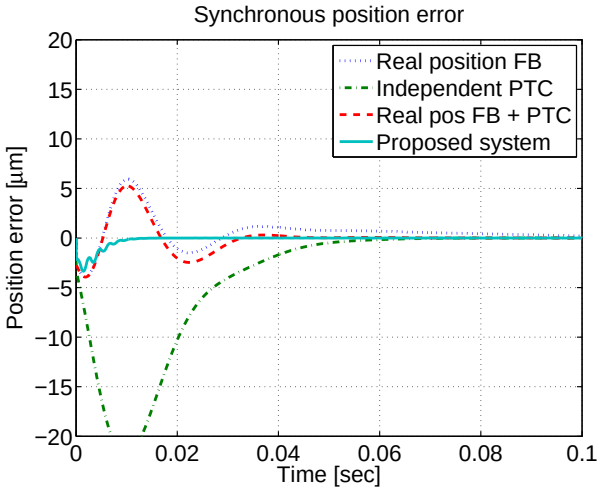

(d) Disturbance 0.01 Nm (expanded)

Figure 3.6: Simulation results.

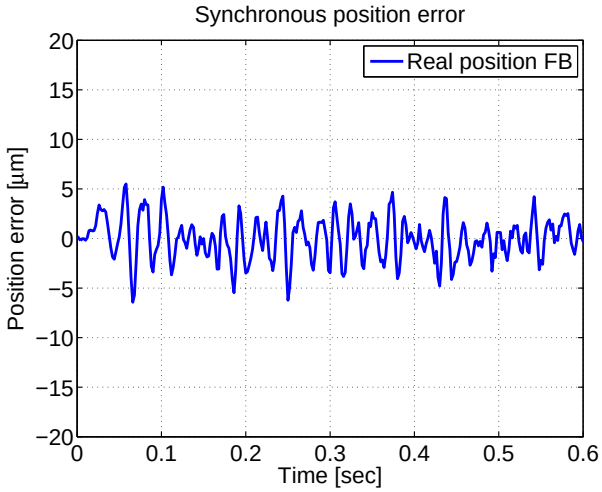

(a) Real position FB

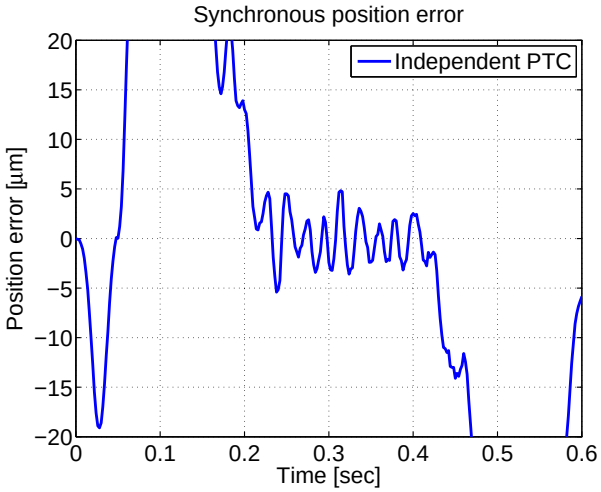

(b) Independent PTC

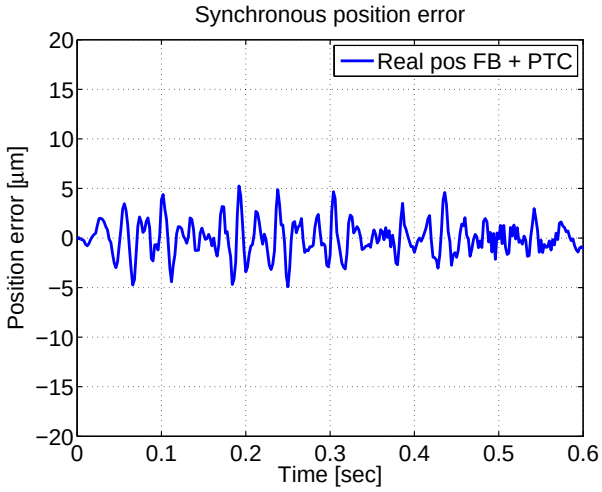

(c) Real position FB + PTC

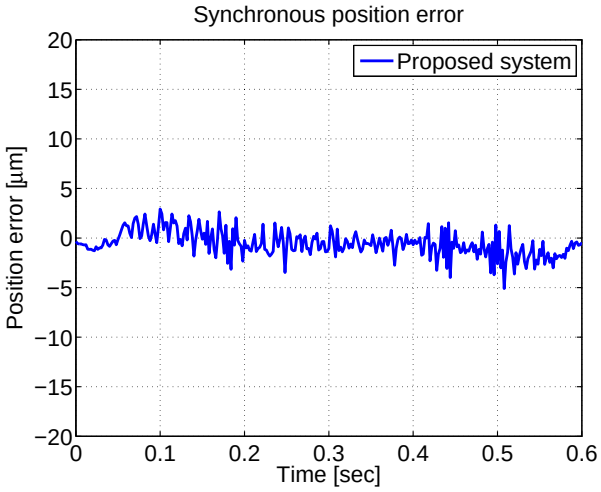

(d) Proposed system

Figure 3.7: Experimental results.

Chapter 4

Attitude Control based on Multirate Control

4.1 Abstract

The large-scale high-precision scan-stage is industrial equipment for microfabrication. The scan-stage needs not only fast and precise positioning but also the attitude control of the stage. The attitude of the stage is disturbed by the stage thrust in scanning. However, the sampling time of output is much longer than the sampling time of control input by DSP because image sensors are employed in the output encoder. It is difficult to reject the disturbances by single-rate feedback system. In this chapter, the attitude control based on PTC (perfect tracking control) using driving force and surface shape of the stage is proposed. Finally, simulations and experiments are performed to show the advantages of the proposed control system.

4.2 Introduction

In exposure systems which have lens, the focus range of lens narrows for microfabrication of products every year. These systems require scanning drive on keeping the attitude of the stage in the focus range. Thus, the positions, in not only the translation direction but also the attitude of the stage, must be controlled in scanning. However, disturbances via driving force in the translation direction influence the pitching, the rolling and the height directions.

Nowadays, active anti-vibration apparatuses are applied in order to suppress vibrations of the pitching and the rolling actively in high-precision stages[31]. However, enough accuracy in scanning cannot be achieved only by the anti-vibration apparatus. Attitude control mechanism is required. In this chapter, the attitude control is called auto focus and leveling (AF/LV) control.

Moreover, the sampling time of output is much longer than the sampling time of control input by DSP because image sensors are employed in the output encoder[32]. It is difficult to reject the disturbances by single-rate feedback system. In this chapter, disturbances via driving force in the translation direction and the surface shape of the stage are modeled, and then the multirate control system in which the disturbance information is utilized as the target trajectory is proposed.

4.3 Modeling of AF/LV

In this section, auto focus and leveling (AF/LV) of the scan stage are explained. The pitching and the rolling occur by the acceleration in driving of the scan stage like Fig. 4.1. Moreover, the distance from the image sensor to the surface shape of the stage can be changed in several ten micron meters because the stage is large. Therefore, the stage has the leveling control mechanism which consists of three actuators driven in the z direction. The leveling control mechanism can control the pitching, the rolling and the height of the stage independently. The pitching, the rolling and the height of the stage can be detected by the image sensor. The characteristic from the leveling control mechanism to the image sensor is called auto focus (AF). Here, Fig. 4.1 shows the driving in the X direction, then the scan stage has mechanism which can drive in the X and Y direction independently.

The block diagram of AF/LV is shown in Fig. 4.2. In this chapter, the pitching of the stage is only explained because the pitching, the rolling and the height of the stage can be represented by the same block diagram respectively. $P_{LV}(s)$ and $P_{AF}(s)$ represent the block of the leveling control system and the block of the auto focus, respectively. The whole AF/LV control system is the plant. The summation of the disturbances from the thrust of the stage and the surface of the stage is input to the output side of the plant. Here, H, S in Fig. 4.2 represent the holder and the sampler, respectively, and $G_d(s)$ represents the transfer characteristic from the thrust of the stage to the disturbance. The output disturbance $d(t)$ can be represented by almost the same trajectory in every driving if the thrust of the stage, the scanning velocity and the position are the same in every driving.

Next, the plant $P(s)$ which represents the transfer characteristic from control input to the image sensor is explained. The input to the leveling control system is the reference of the pitching. The output of the leveling control system is the pitching based on Y carriage which can be controlled by the Z actuators. $P_{LV}(s)$ which represents the transfer characteristic of the leveling control system is the second order delay system. Then, the auto focus $P_{AF}(s)$ which represents the transfer characteristic from the output of the leveling control system to the pitching based on global coordinate system is the second order. The auto focus $P_{AF}(s)$ has the primary resonance mode because of the reaction force by the Z actuators. Thus, the

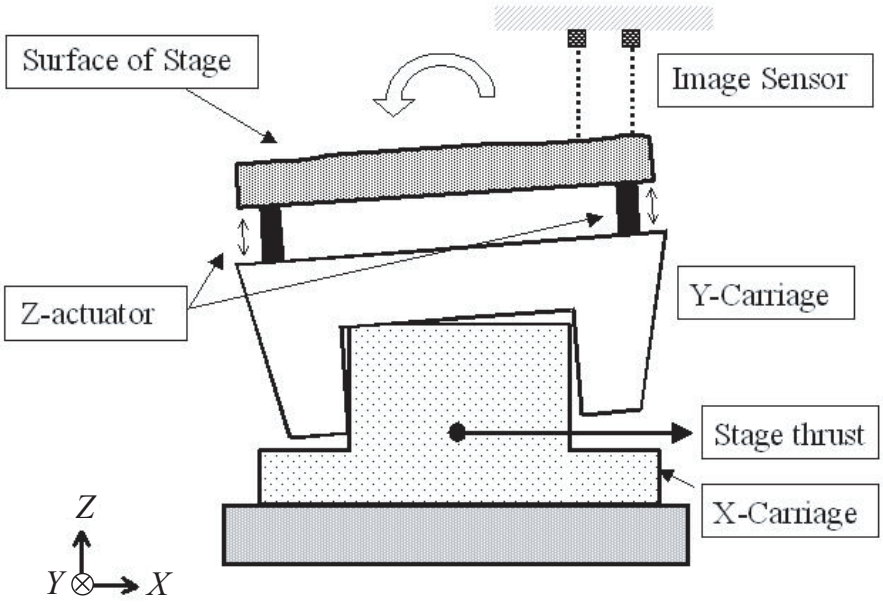

Figure 4.1: Large-scale high-precision scan-stage model.

transfer functions of AF/LV are represented by

$$P_{LV}(s) = \frac{b_{LV0}}{s^2 + a_{LV1}s + a_{LV0}}, \tag{4.1}$$

$$P_{AF}(s) = \frac{b_{AF2}s^2 + b_{AF1}s + b_{AF0}}{s^2 + a_{AF1}s + a_{AF0}}. \tag{4.2}$$

The transfer function of the plant is represented by

$$P(s) = P_{LV}(s)P_{AF}(s) \tag{4.3}$$

$$= \frac{b_2s^2 + b_1s + b_0}{s^4 + a_3s^3 + a_2s^2 + a_1s + a_0}. \tag{4.4}$$

The relative degree of the plant is two. The frequency responses of the plant are shown in Fig. 4.3. It is assumed that the nominal model of the plant is minimum phase system because the bandwidth, in which AF/LV is controlled, is until 20 Hz.

4.4 Multirate Feedback Control

In this section, the design of multirate feedback controller [33] is explained. The continuous-time controller based on the regulator and the disturbance observer is discretized as the characteristic of the closed loop corresponds every M times. M is defined as N/n. Here, N is determined by the hardware restriction, and n is the plant order.

The continuous-time plant model is defined as

$$\begin{cases} \dot{\boldsymbol{x}}_p(t) = \boldsymbol{A}_{cp}\boldsymbol{x}_p(t) + \boldsymbol{b}_{cp}(u(t) - d(t)) \\ y(t) = \boldsymbol{c}_{cp}\boldsymbol{x}_p(t) \end{cases}, \tag{4.5}$$

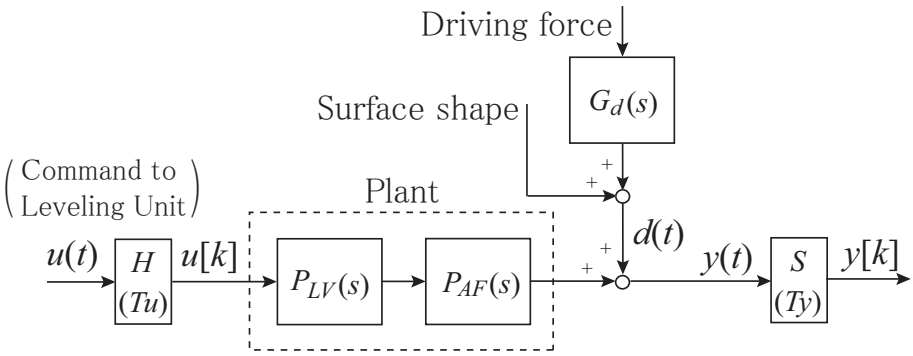

Figure 4.2: Block diagram of AF/LV.

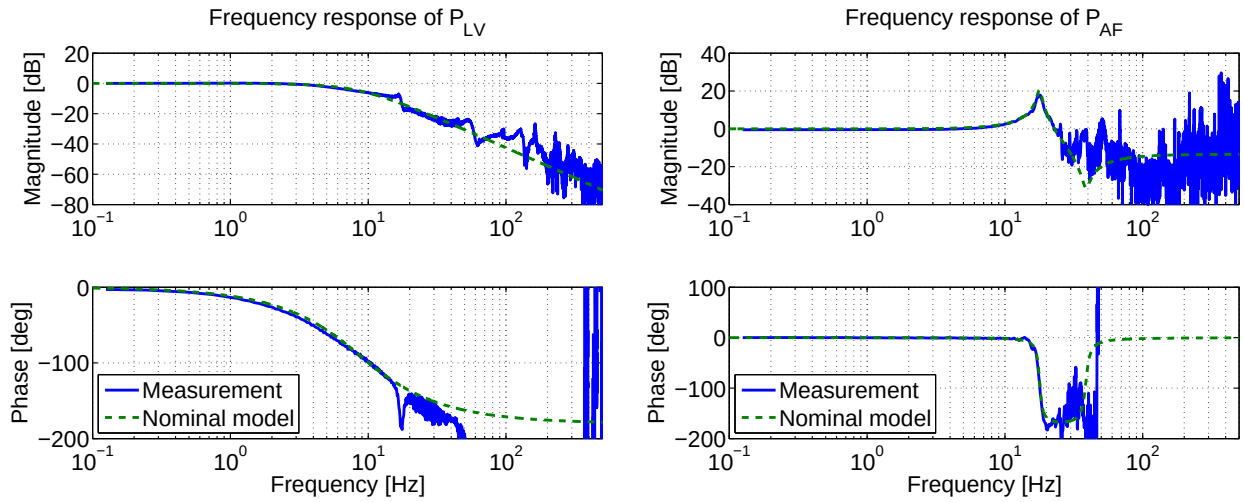

(a) P_{LV} (b) P_{AF}

Figure 4.3: Frequency responses of plants.

where $d(t)$ is the disturbance input. The disturbance model is defined as

$$\begin{cases} \dot{\boldsymbol{x}}_d(t) = \boldsymbol{A}_{cd}\boldsymbol{x}_d(t) \\ d(t) = \boldsymbol{c}_{cd}\boldsymbol{x}_d(t) \end{cases}. \tag{4.6}$$

The augmented continuous-time plant model can be represented by

$$\dot{\boldsymbol{x}}(t) = \boldsymbol{A}_c\boldsymbol{x}(t) + \boldsymbol{b}_c u(t), y(t) = \boldsymbol{c}_c\boldsymbol{x}(t), \tag{4.7}$$

$$\left[\begin{array}{c|c} \boldsymbol{A}_c & \boldsymbol{b}_c \\ \hline \boldsymbol{c}_c & \boldsymbol{0} \end{array}\right] \triangleq \left[\begin{array}{cc|c} \boldsymbol{A}_{cp} & -\boldsymbol{b}_{cp}\boldsymbol{c}_{cd} & \boldsymbol{b}_{cp} \\ \boldsymbol{0} & \boldsymbol{A}_{cd} & \boldsymbol{0} \\ \hline \boldsymbol{c}_{cp} & \boldsymbol{0} & \boldsymbol{0} \end{array}\right], \tag{4.8}$$

where $\boldsymbol{x} = [\boldsymbol{x}_p{}^T, \boldsymbol{x}_d{}^T]^T$. For the plant (4.7), the continuous-time observer and regulator

Table 4.1: Sampling periods (s).

T_u	T_r	T_y
1/3000	4/3000	16/3000

designed from the Gopinath's method by

$$\begin{cases} \dot{\hat{\boldsymbol{v}}}(t) = \hat{\boldsymbol{A}}_c\hat{\boldsymbol{v}}(t) + \hat{\boldsymbol{b}}_c y(t) + \hat{\boldsymbol{J}}_c\boldsymbol{u}(t) \\ \hat{\boldsymbol{x}}(t) = \hat{\boldsymbol{C}}_c\hat{\boldsymbol{v}}(t) + \hat{\boldsymbol{d}}_c y(t) \end{cases}, \tag{4.9}$$

$$u(t) = \boldsymbol{f}_{cp}\hat{\boldsymbol{x}}_p(t) + \boldsymbol{c}_{cd}\hat{\boldsymbol{x}}_d(t) = \boldsymbol{f}_c\hat{\boldsymbol{x}}(t). \tag{4.10}$$

Here, for the plant (4.7) discretized by multirate N, the discrete-time observer and regulator on the sampling points is obtained by

$$\begin{cases} \hat{\boldsymbol{v}}[i+1] = \hat{\boldsymbol{A}}\hat{\boldsymbol{v}}[i] + \hat{\boldsymbol{b}}y[i] + \hat{\boldsymbol{J}}_c\boldsymbol{u}[i] \\ \hat{\boldsymbol{x}}[i] = \hat{\boldsymbol{C}}\hat{\boldsymbol{v}}[i] + \hat{\boldsymbol{d}}y[i] \end{cases}, \tag{4.11}$$

$$u[i] = \boldsymbol{F}_p\hat{\boldsymbol{x}}_p[i] + \boldsymbol{F}_d\hat{\boldsymbol{x}}_d[i] = \boldsymbol{F}\hat{\boldsymbol{x}}[i]. \tag{4.12}$$

The state feedback gain $\boldsymbol{F}$ is determined as the characteristic of the closed loop corresponds every M times.

Thus, the multirate feedback controller can be represented as follows:

$$\boldsymbol{u}[i] = \left[\begin{array}{c|c} \hat{\boldsymbol{A}} + \hat{\boldsymbol{J}}\boldsymbol{F}\hat{\boldsymbol{C}} & \hat{\boldsymbol{b}} + \hat{\boldsymbol{J}}\boldsymbol{F}\hat{\boldsymbol{d}} \\ \hline -\boldsymbol{F}\hat{\boldsymbol{C}} & -\boldsymbol{F}\hat{\boldsymbol{d}} \end{array}\right] e[i], \tag{4.13}$$

$$e[i] = y_0[i] - y[i]. \tag{4.14}$$

4.5 Control Design for AF/LV

In the block diagram of AF/LV shown in Fig. 4.2, the disturbance $d(t)$ cannot be suppressed well by singlerate control system because output period T_y is 16 times as long as control period T_u. Therefore, the proposed control system which consists of VSPTC and the multirate feedback control is designed.

The output disturbance trajectory measured in a scanning trajectory is shown in Fig. 4.4. Suppression of the output disturbance improves the accuracy directly because the output disturbance can be measured by the sensor. Therefore, the output disturbance can be suppressed positively every the target period T_r which is 4 times as fast as the output period T_y by using VSPTC in which $-d(t)$ is applied to the target trajectory. Sampling periods are shown in Table 4.1.

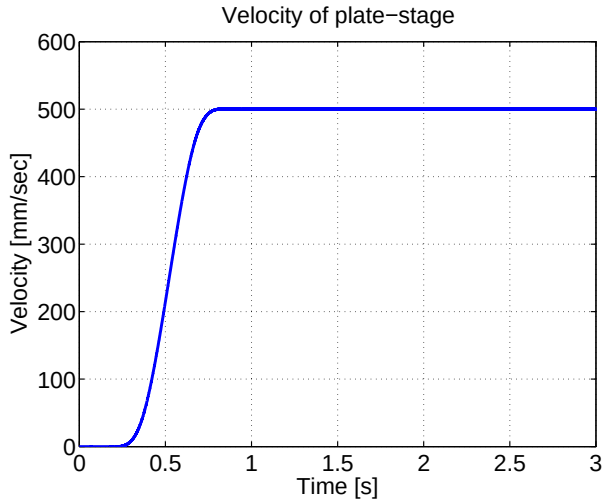

(a) Scan-velocity trajectory of the stage

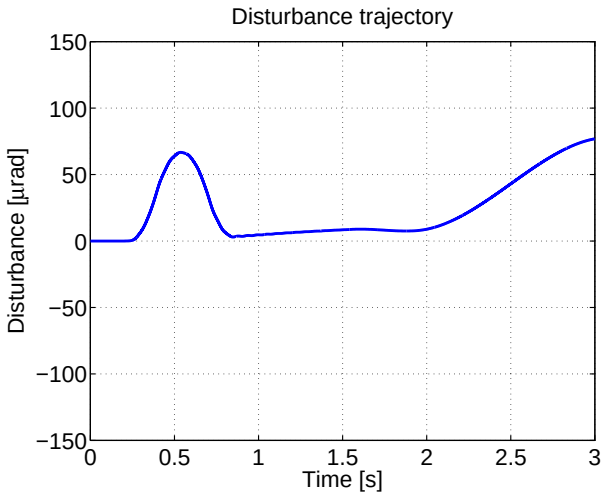

(b) Output disturbance

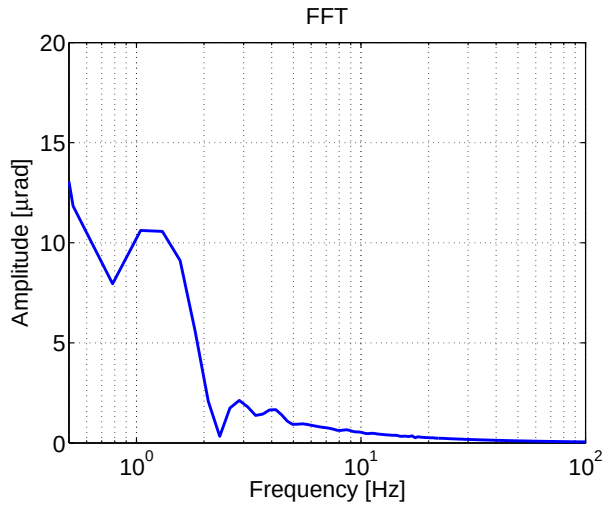

(c) Spectrum of output disturbance

Figure 4.4: Output disturbance trajectory (measured value).

VSPTC requires the target trajectory $\boldsymbol{r}(t)$ which consists of the disturbance trajectory one sample ahead $-d(t+T_r)$ and the derivations until $n-1$ times. Therefore, the target trajectory is described by

$$\boldsymbol{r}(t) = [-d(t), -d^{(1)}(t), -d^{(2)}(t), -d^{(3)}(t)]^T, \tag{4.15}$$

where $d^{(n)}(t)$ is the n times derivation of $d(t)$. The target trajectory due to the thrust of the stage is developed by inputting the thrust to the time function and the derivations of the transfer characteristic $G_d(s)$. The target trajectory due to the surface shape of the stage is developed by difference of the trajectory of the surface shape.

Moreover, the target trajectory filter $R[z]$ is required in order to transform the target trajectories into the states in VSPTC. Fig. 4.5 shows the target trajectory filter in both

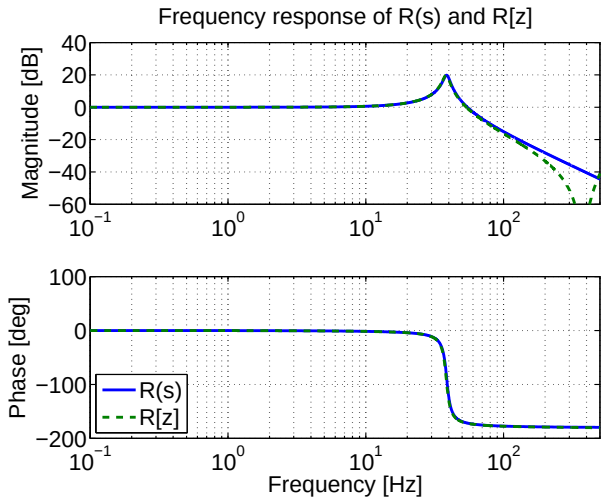

Figure 4.5: Frequency response of R(s) and R[z].

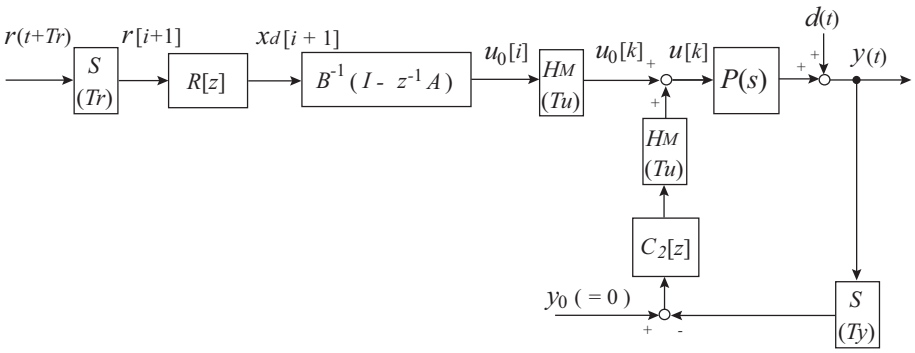

Figure 4.6: Proposed AF/LV control system with vibration suppression PTC.

continuous-time system and discrete-time system. The discretized target trajectory can be applied without discretization error against the frequency components of the disturbance because the target sampling frequency is 750 Hz. The proposed AF/LV control system is shown in Fig. 4.6.

4.6 Simulations

4.6.1 High Bandwidth Design by Multirate Feedback Control

The closed loop characteristic was evaluated when the multirate feedback controller was applied to $C_2[z]$. The pole placement base on multiple poles was not always appropriate because of the resonance mode of the plant. Therefore, the continuous-time controller which consists of the PID controller and the notch filter is designed, and then the observer and

Table 4.2: Phase margin.

Continuous	Multirate FB	Single-rate Tustin
60.0 deg	45.3 deg	Unstable

the regulator are designed as the characteristic of the closed loop corresponds. Thus, the multirate feedback controller can be designed by Section 4.4.

It is possible to perfectly suppress the frequency components which the disturbance model has. However, if the disturbance model becomes high order model in order to match the real disturbance, not only the multirate feedback controller becomes high order but also the stability margin of the system becomes small. Therefore, the disturbance is modeled by simple first order model, and then high bandwidth which is not achieved by singlerate feedback is performed.

The PID controller $C_{PID}(s)$ and the filter $C_f(s)$ are designed as follows:

$$C(s) = C_{PID}(s)C_f(s), \tag{4.16}$$

$$C_{PID}(s) = \frac{b_{c2}s^2 + b_{c1}s + b_{c0}}{s^2 + a_{c1}s}, \tag{4.17}$$

$$C_f(s) = \frac{1}{P_{AF}(s)}. \tag{4.18}$$

Here, $C_{PID}(s)$ is designed by pole placement base on multiple poles, and $C_f(s)$ is the inverse system of $P_{AF}(s)$.

The continuous-time feedback, the multirate feedback and the singlerate Tustin feedback are designed as low frequency characteristic of sensitivity function corresponds respectively. The bandwidth of the feedback is about 30 Hz, and Nyquist frequency is 93.75 Hz. The frequency responses are shown in Fig. 4.7. The phase margins are shown in Table 4.2.

As the result, the system of the singlerate Tustin feedback is unstable in the case of high bandwidth near Nyquist frequency because of the discretization error. On the other hand, the system of the multirate feedback keeps the characteristic of the continuous-time system enough, and the phase margin is kept for the system to be stable.

4.6.2 Disturbance Predictive Control by VSPTC

In the case that the output disturbance shown in Fig. 4.4, the disturbance predictive control by VSPTC in which the disturbance information is applied to the target trajectory is verified. Here, the plant model is nominal.

The simulation results by using only the multirate feedforward controller are shown in Fig. 4.8. The multirate feedforward controller can suppress the output disturbance enough if the plant is nominal and the disturbance is predicted.

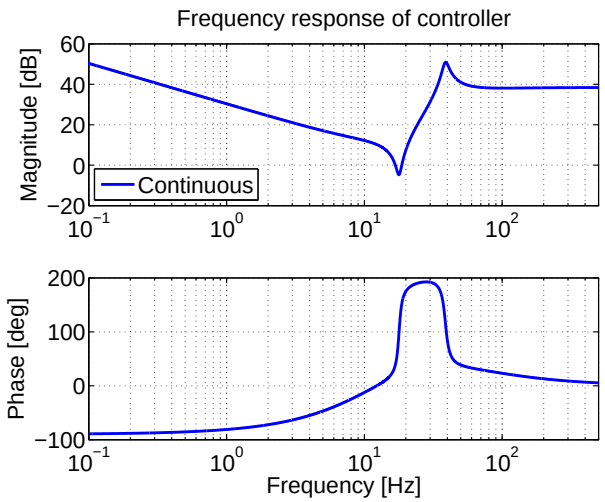

(a) Frequency response of controller

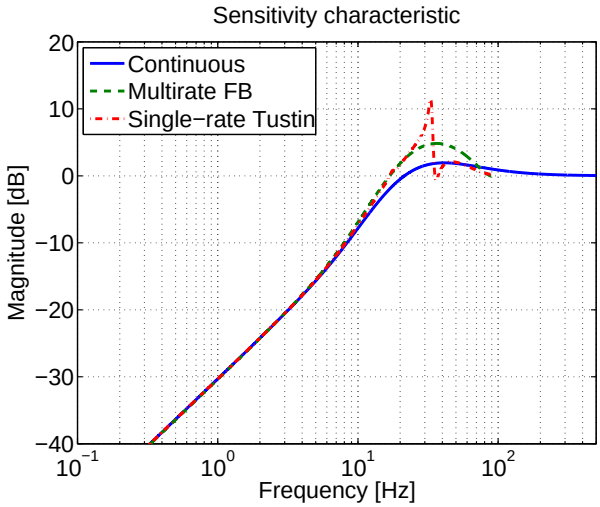

(b) Sensitivity characteristic

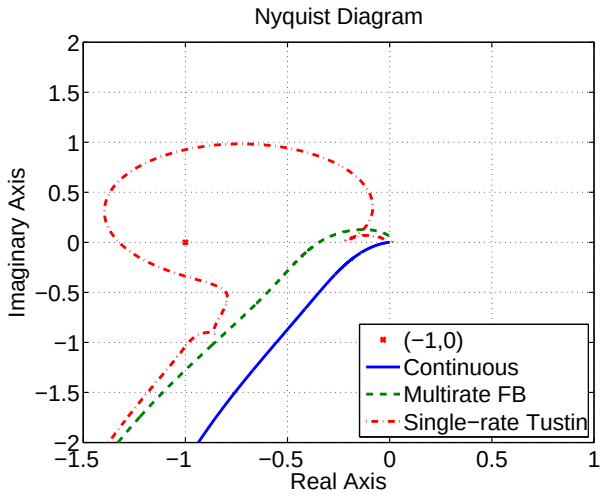

(c) Nyquist diagram

Figure 4.7: Frequency responses.

4.7 Experiments

The experiments of the disturbance predictive control by VSPTC are performed by the actual equipment. Here, the feedback controller $C_2[z]$ is PI controller discretized by the period T_y. 1 DOF control system which consists of the PI controller only is compared with VSPTC in which the disturbance information is applied to the target trajectory. The closed loop characteristics by the feedback controller $C_2[z]$ are shown in Fig. 4.9. The bandwidth of the feedback system is about 1 Hz.

The experimental results of the pitching control are shown in Fig. 4.10. The frequency components of the disturbance in more than 1 Hz exist mainly from Fig. 4.4(c). However, the disturbance cannot be suppressed enough because the bandwidth of the feedback system

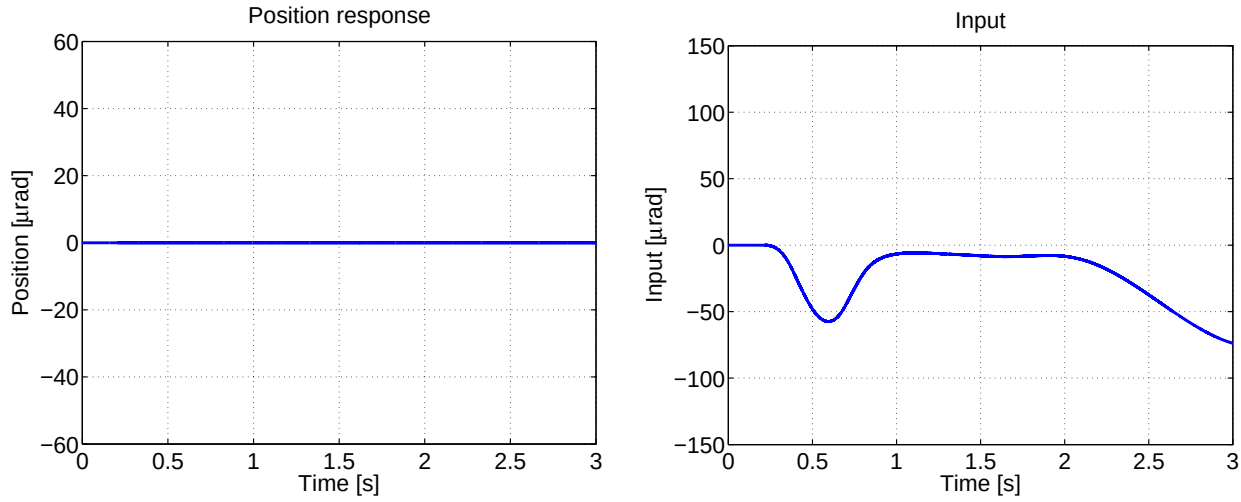

(a) Pitching (b) Input

Figure 4.8: Simulation results of vibration suppression PTC (multirate feedforward controller only).

Table 4.3: Evaluation of experiment.

	3σ w/o VSPTC	3σ with VSPTC	Improvement rate
Pitching	31.81 μrad	13.82 μrad	56.6 % off
Height	18.04 μm	6.01 μm	66.7 % off

is about 1 Hz. As the result, in the case of the PI controller only, the big position error exists in acceleration time at 0.5 s especially.

On the other hand, VSPTC can suppress the predicted output disturbance by feedforward control. Here, the position error which exists at 0.8 s, 1.2 s, 1.6 s, 2.0 s and $\cdots$ is caused by the periodical asperity of the stage surface. This periodical asperity is not included in the target trajectory because this is the disturbance which should not be tracked.

The standard deviation 3σ of position response including the acceleration time from 0.0 s to 3.0 s and the improvement rate (based on the conventional standard deviation) are shown in Table 4.3. The position error is improved by 56.6 % in the pitching control.

Then, the experimental results of the height control are shown in Fig. 4.11. In Table 4.3, the position error is improved by 66.7 % in the height control.

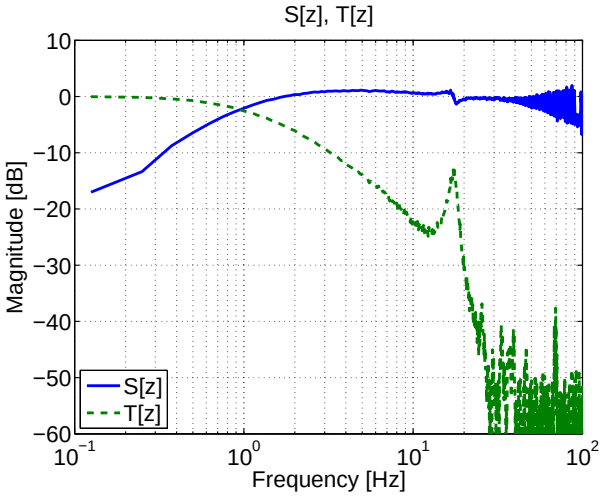

Figure 4.9: Closed loop characteristics.

4.8 Summary

VSPTC which applies the disturbance information to AF/LV control positively was proposed. The perfect tracking control system by the feedforward control by the fast control period T_u (= 1/3000 s) was designed as the disturbance detected per the period T_y (= 16/3000 s) was applied to the target trajectory directly. Moreover, in the system in which the output period is 16 times as long as the control period, the multirate feedback control can achieve the high bandwidth of the feedback system. Finally, simulations and experiments are performed to show the advantages of the proposed control system.

It is expected that the proposed control system can be applied to not only AF/LV control of the stage but also the system in which the long output period is the problem of the control performance.

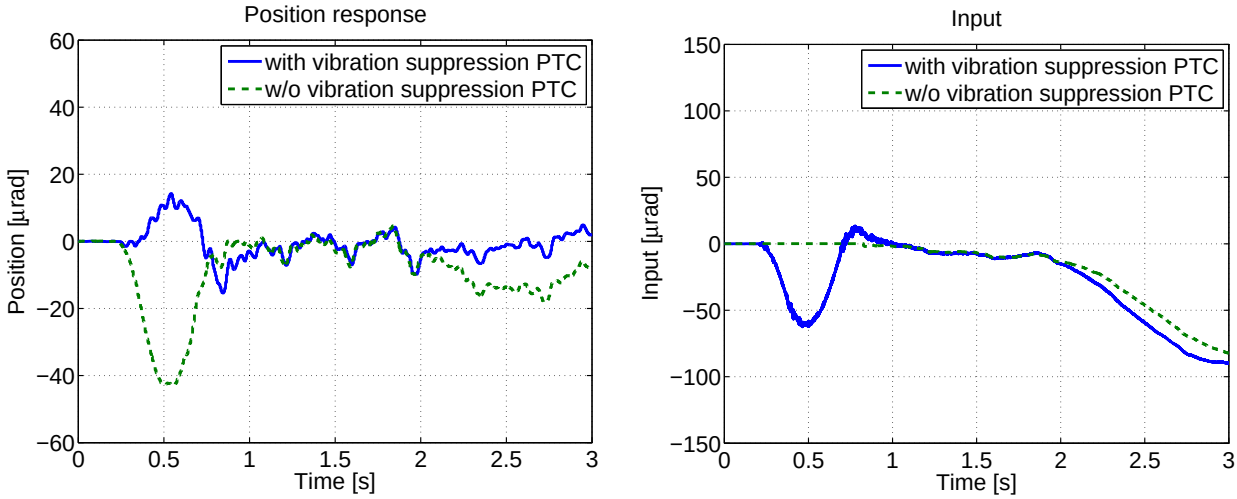

(a) Pitching (b) Control input

Figure 4.10: Experimental results of pitching control.

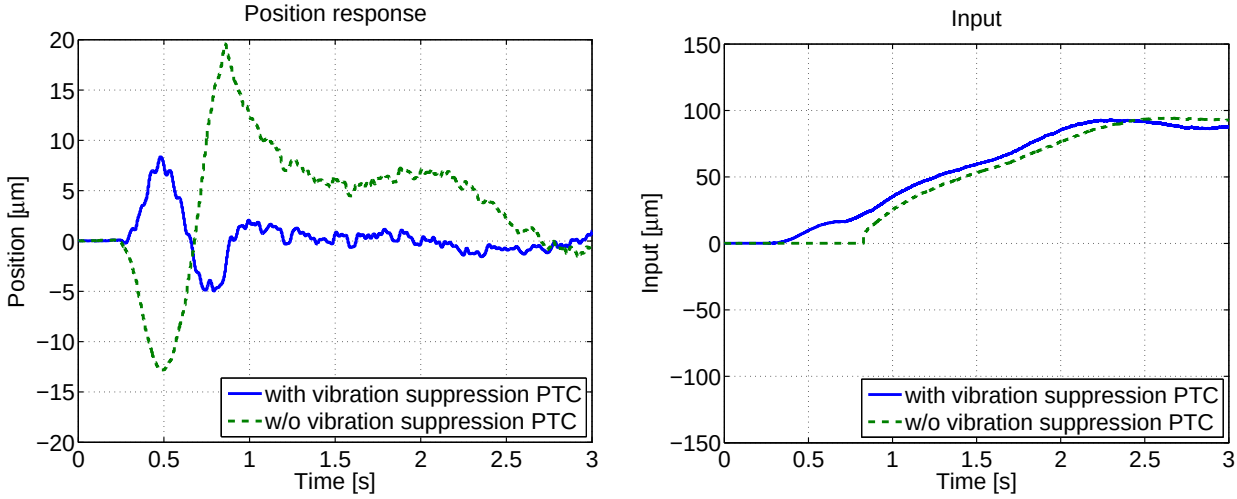

(a) Height (b) Control input

Figure 4.11: Experimental results of height control.

Part II

Advanced Multirate Control Techniques

Chapter 5

Ultrahigh-Speed Nanoscale Positioning based on Multirate PWM Control

5.1 Abstract

Motion control techniques are employed on nanoscale positioning in industrial equipments, for example, NC machine tools, exposure systems, and so on. The advanced motion control techniques are based on the precise current control. However, speed-up of the precise current response has a serious limitation because of the carrier period of an inverter. In addition, the position response has to be slower than the current response. Then, novel ultrahigh-speed nanoscale positioning based on multirate PWM control is proposed. Finally, simulations and experiments are performed to show the advantages of the proposed method.

5.2 Introduction

Digital control of servomotors has been researched actively thanks to high-speed switching of PWM inverter and improved arithmetic processing of digital signal processor (DSP). Nowadays, motion control techniques are employed on nanoscale positioning in precision mechanical equipment, for example, NC machine tools, exposure systems, and so on. Especially, the high-precision motion control is required to achieve nanoscale positioning for stages of exposure systems.

The high-precision motion control is founded on precise current control of the motor. The performance of the current control is very important. However, speed-up of the precise current response has a serious limitation because of the carrier period of an inverter. In addition, the position response has to be slower than the current response. There is a

research that field programmable gate array (FPGA) is developed for motor drives to solve the problem of the limitation of the carrier period [34]. In the other way of approach with control technology, there are advantages of reduction of cost and switching loss.

In [25], the author's research group proposed multirate PWM control, and achieved a positioning in 20 ms by using a brushless DC-motor with a rough encoder. The proposed method has a novel feedforward controller considering the PWM pulse of the inverter and the current loop.

This chapter illustrates ultrahigh-speed nanoscale positioning based on the proposed method with an experimental precision stage. The position error is in 100 nm. The positioning time is 2 ms which was only 10 times as long as the carrier period. In section 5.3, the constitution and characteristics of the stage are shown. In section 5.4, multirate PWM position control is described. In addition, a simple and effective suppression filter for the primary resonance mode is designed in order to achieve ultrahigh-speed nanoscale positioning. Finally, simulations and experiments are performed to show the advantages of the proposed method.

5.3 Nano-stage

An experimental high-precision stage was designed and fabricated to research ultrahigh-speed nanoscale positioning. The experimental stage is called "Nano-stage," as shown in Fig. 5.1.

5.3.1 Constitution of Nano-stage

Nano-stage driven by linear motor is the stage whose friction is almost zero because of using the air guide. Moreover, Nano-stage has two linear encoders to measure both the motor part, which is the drive, and the stage part, which is the load. The resolution of the linear encoders is 1 nm/pulse respectively to achieve nanoscale positioning.

Nano-stage can be switched to two modes of the rigid mode and the two-inertia mode. In the two-inertia mode, the motor and the stage parts are connected by leaf springs. The resonance characteristic can be changed by replacing the leaf springs. Then, Nano-stage can be switched to the rigid mode because the motor and the stage parts are fixed by plates. In this chapter, Nano-stage is treated as the rigid mode. Then, calculating the barycentric position of the stage with upper and lower encoders, the position is assumed as the real position of the stage.

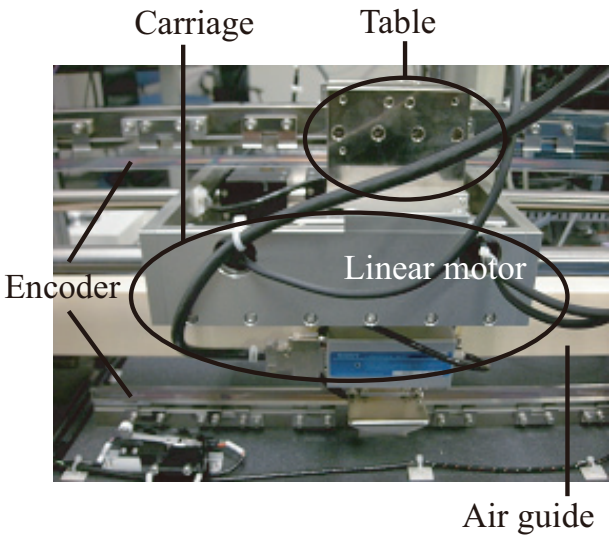

Figure 5.1: Nano-stage.

Table 5.1: Parameters of Nano-stage.

Inductance L	6.4	mH
Resistance R	13.1	Ω
Mass M	14.3	kg
Viscosity B	22.8	N/(m/s)
Thrust coefficient K_t	28.5	N/A
Back-EMF constant K_e	9.5	V/(m/s)
Size	22×23×21	cm^3

5.3.2 Characteristics of Nano-stage

Pole-zero canceling proportional-integral current controller was designed for the current loop to be first-order system whose band frequency was 1 kHz. Table 5.1 shows parameters of Nano-stage. Fig. 5.2 shows the frequency response from the current reference to the velocity of the stage. Here, the solid line is the plant model involved the primary resonance and the anti-resonance mode $G_{vib}(s)$ as follows:

$$\frac{\dot{y}}{i^{ref}} = \frac{1}{\tau s + 1} \cdot \frac{1}{Ms + B} \cdot G_{vib}(s), \tag{5.1}$$

where $\tau = 1/(2\pi 1000)$. Note that there is the resonance mode in spite of the stage of the rigid mode. The resonance mode is considered in section 5.5.

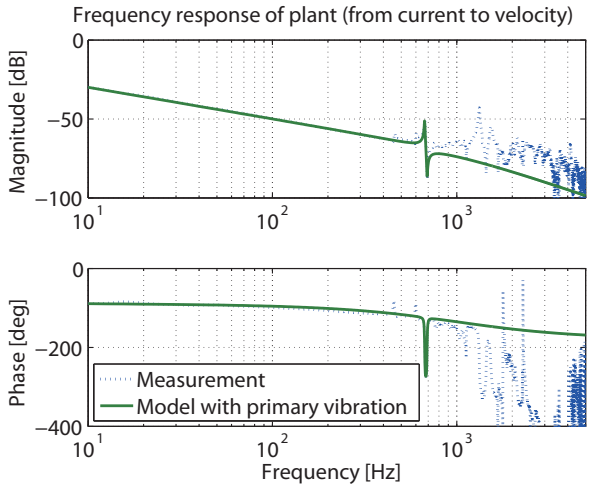

Figure 5.2: Frequency response of Nano-stage.

5.4 Multirate PWM Position Control

Multirate PWM control system is a kind of perfect tracking control (PTC) system [20] which is designed for a plant model discretized based on PWM hold. Multirate PWM control is designed considering a current loop and instantaneous values of PWM pulse precisely. High-speed positioning in several carrier sampling periods, which are shorter than the response of the current loop, can be achieved. In output voltage control of a single-phase inverter, a high performance control, which tracks the output voltage on an arbitrary waveform, was achieved [35].

5.4.1 Discrete Model Based on PWM-hold

In order to discretize a plant model, a zero-order hold is applied generally. However, in the case that a single-phase inverter (or a four-quadrant chopper), shown in Fig. 5.3, actuates DC-motor, and then the inverter generates not arbitrary output vector $V[k]$ but only 0 or $\pm E$[V] as Fig. 5.4. Therefore, in order to control instantaneous values precisely, the zero-order hold is unsuitable because the precise discrete model is based on the PWM hold of Fig. 5.4. The plant model of a motor actuated by an inverter can be discretized based on the PWM hold as follows [36].

A continuous-time state equation of a plant is represented by

$$\begin{cases} \dot{\boldsymbol{x}}(t) = \boldsymbol{A}_c \boldsymbol{x}(t) + \boldsymbol{b}_c u(t) \\ y(t) = \boldsymbol{c}_c \boldsymbol{x}(t) \end{cases} . \tag{5.2}$$

The precise discrete model in which the input $u[k]$ is the switching time $\Delta T[k]$ is obtained

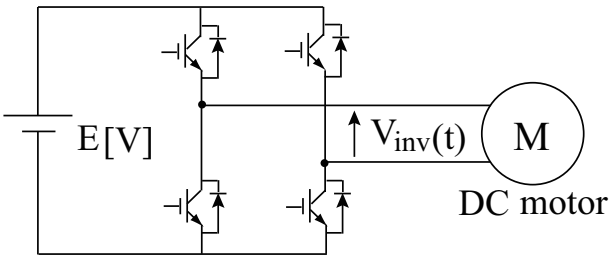

Figure 5.3: Single-phase inverter.

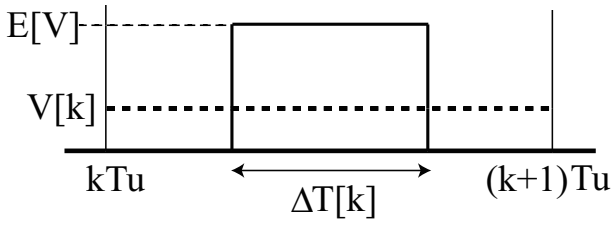

Figure 5.4: PWM hold.

as

$$\begin{cases} \boldsymbol{x}[k+1] = \boldsymbol{A}_s\boldsymbol{x}[k] + \boldsymbol{b}_s\Delta T[k] \\ y[k] = \boldsymbol{c}_s\boldsymbol{x}[k] \end{cases}, \tag{5.3}$$

where

$$\boldsymbol{A}_s = e^{\boldsymbol{A}_{cT_u}}\ ,\ \boldsymbol{b}_s = e^{\boldsymbol{A}_{cT_u/2}}\boldsymbol{b}_cE\ ,\ \boldsymbol{c}_s = \boldsymbol{c}_c. \tag{5.4}$$

When $\Delta T[k]$ is negative, $-E$[V] is output. (5.3) can be applied for AC-servo system driven by 3-phase inverter with vector control.

5.4.2 Original PTC System

PTC is designed for the third-order plant having the ideal first-order current dynamics. This method is named "Conventional 2." The design method for the second-order plant ignored current loop is named "Conventional 1."

The plant of "Conventional 1" is described by

$$\frac{y}{i^{ref}} = \frac{1}{Ms^2 + Bs}. \tag{5.5}$$

The plant of "Conventional 2" is described by

$$\frac{y}{i^{ref}} = \frac{1}{\tau s + 1} \cdot \frac{1}{Ms^2 + Bs}. \tag{5.6}$$

These plants are discretized by zero-order hold, and then PTC is designed.

5.4.3 Constitution of Multirate PWM Position Control System

In the rigid mode, q axis model of Nano-stage is shown in Fig. 5.5. Therefore, a control system can be designed for the model with vector control. The transfer function from V_{inv} to y is described by

$$\frac{y}{V_{inv}} = \frac{K_t}{MLs^3 + (MR + LB)s^2 + (BR + K_eK_t)s}. \tag{5.7}$$

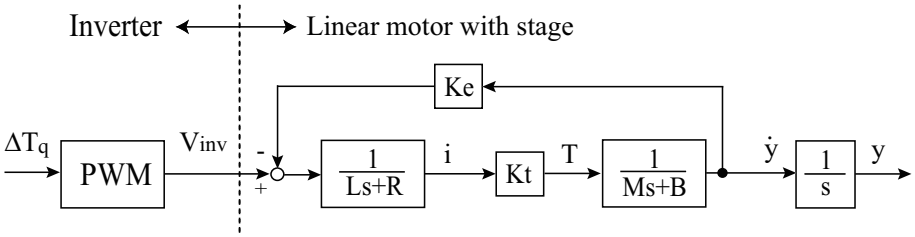

Figure 5.5: q axis model of rigid mode.

The controllable canonical form of (5.7) is given by

$$\left[\begin{array}{c|c} \boldsymbol{A}_c & \boldsymbol{b}_c \\ \hline \boldsymbol{c}_c & 0 \end{array}\right] = \left[\begin{array}{ccc|c} 0 & 1 & 0 & 0 \\ 0 & 0 & 1 & 0 \\ 0 & -\frac{BR+K_eK_t}{ML} & -\frac{MR+LB}{ML} & \frac{K_t}{ML} \\ \hline 1 & 0 & 0 & 0 \end{array}\right], \tag{5.8}$$

according to (5.2), where $\boldsymbol{x} = [\, y \;\; \dot{y} \;\; \ddot{y} \,]^T$.

Also, the transfer function from V_{inv} to i is described by

$$\frac{i}{V_{inv}} = \frac{Ms^2 + Bs}{MLs^3 + (MR + LB)s^2 + (BR + K_eK_t)s}. \tag{5.9}$$

The output equation of (5.9) is represented by

$$y = \boldsymbol{c}_c'\boldsymbol{x} \;,\; \boldsymbol{c}_c' = \left[\begin{array}{ccc} 0 & \frac{B}{K_t} & \frac{J}{K_t} \end{array}\right]. \tag{5.10}$$

The multirate PWM position control system considering PWM hold can be designed as Fig. 5.6. The current controller $C_{PI}[z]$ and the position controller $C_2[z]$ operate only when the errors between the nominal outputs and the actual outputs exist.

5.4.4 Input Generation of Three-phase Inverter

In the case that the plant is AC motor like a liner motor, inputs are the switching times ΔT_d and ΔT_q because the control system is designed by the dq-model. However, in order to apply the three-phase inverter, the input for PWM pulse of the three-phase system has to be generated. The generation method is explained. Here, coordinate transform matrices are represented by absolute transforms.

The input voltage of the three-phase inverter is defined as V_{dc}. The discrete model of (5.3) for the dq system is designed as $E = V_{dc}$ in (5.4). ΔT_d and ΔT_q are transformed into ΔT_α and ΔT_β by the dq/2-phase transform as follows:

$$\left[\begin{array}{c} \Delta T_\alpha \\ \Delta T_\beta \end{array}\right] = \left[\begin{array}{cc} \cos\theta & -\sin\theta \\ \sin\theta & \cos\theta \end{array}\right] \left[\begin{array}{c} \Delta T_d \\ \Delta T_q \end{array}\right]. \tag{5.11}$$

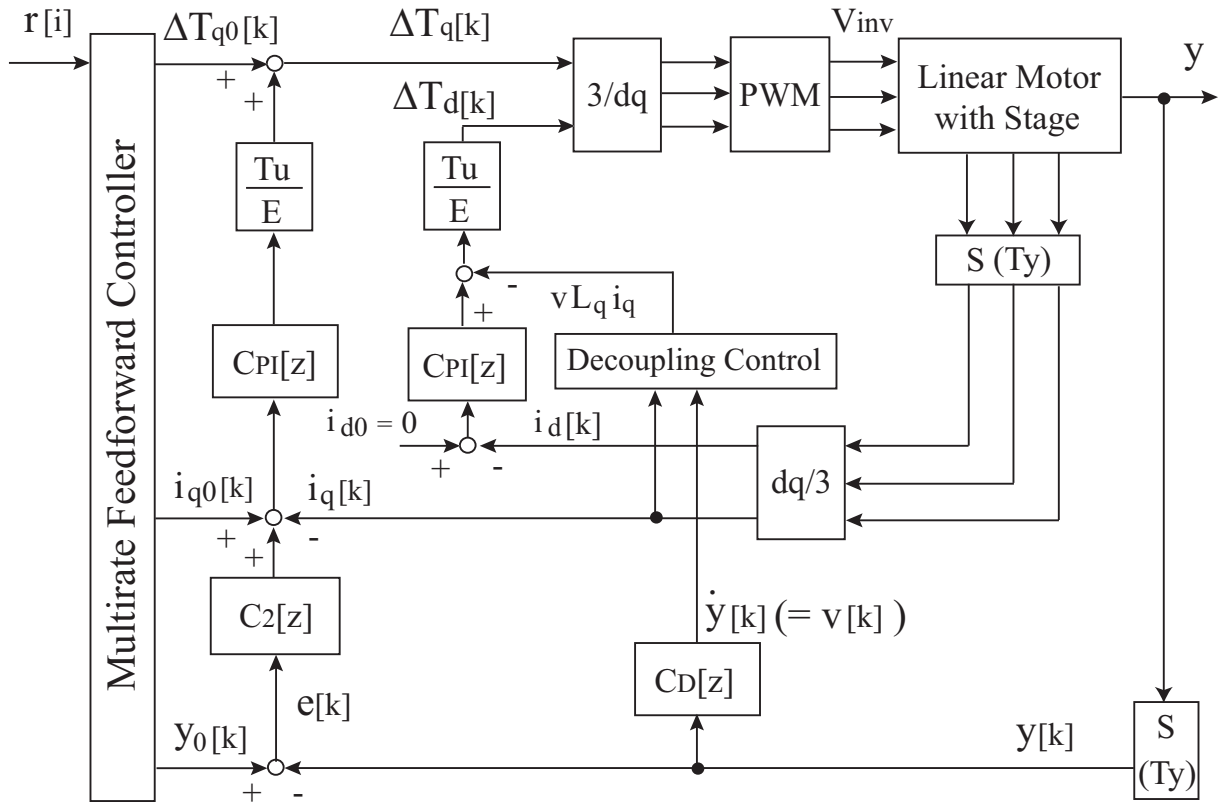

Figure 5.6: Multirate PWM position control system.

Then, ΔT_α and ΔT_β are transformed into ΔT_{uv}, ΔT_{vw}, and ΔT_{wu} by the 2-phase/3-phase absolute transform. The symmetric pulses like Fig. 5.7 are outputs. It can be available to control precisely by (5.3). As below, the order of generation of the pulses is shown.

The region is decided by ΔT_α and ΔT_β in Fig. 5.8. The order and the switching times $\sqrt{3/2}\Delta T_{i,j}$ of the output vectors $V_{i,j}$ in each regions are decided by Table 5.2 and 5.3. Here, $\sqrt{3/2}$ is the coefficient to transform two-phase into three-phase, and the output order is decided for the number of switching times to be fewer.

For example, the pulses of Fig. 5.7 are outputs in the region VI. In this case, the switching time which is $\Delta\ T_1 = \sqrt{3/2}\Delta\ T_i$ and $\Delta\ T_6 = \sqrt{3/2}\Delta\ T_j$ is shared as Table 5.3.

5.4.5 Design of Feedback Control

A proportional-integral-derivative position controller was designed, as band frequency of the position loop was 100 Hz. The sensitivity characteristic is shown in Fig. 5.9. The steady-state position error is shown in Fig. 5.10. The standard deviation 3σ of the steady-state position error is 59.7 nm.

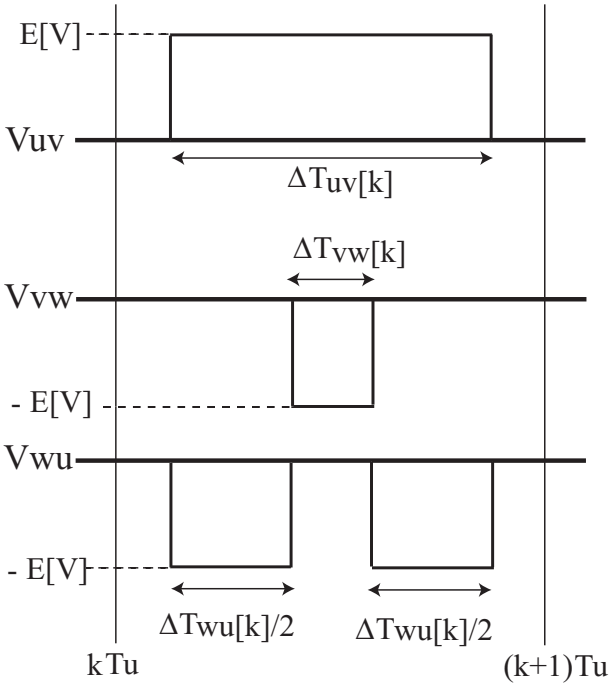

Figure 5.7: Pulse of line voltage.

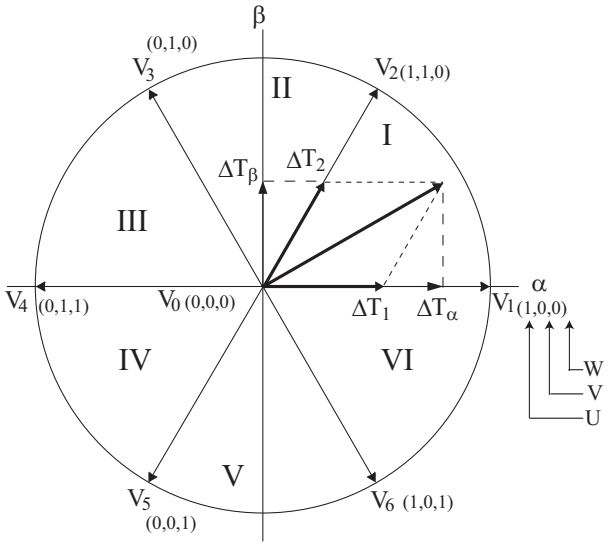

Figure 5.8: Space vector modulation.

5.5 Considering Resonance Mode

Generally, the plant has resonance modes caused by pitching in positioning of a stage. In a large-scaled stage, a lot of resonance modes exist from several Hz to several kilo Hz. Moreover, most of the resonance modes have the anti-resonance modes. Nano-stage has the primary resonance mode at 670 Hz and the anti-resonance mode at 690 Hz in Fig. 5.2.

The characteristic $G_{vib}(s)$ of the primary resonance mode and the anti-resonance mode is represented by

$$G_{vib}(s) = \frac{0.9429s^2 + 32.53s + 17720000}{s^2 + 33.5s + 17720000}. \tag{5.12}$$

It is the biproper minimum phase system. Therefore, the stable inverse model of $G_{vib}(s)$ can be designed. The inverse model is defined as the vibration suppression filter (VSF).

$$VSF(s) = G_{vib}^{-1}(s) \tag{5.13}$$

$VSF[z]$, which is discretized by shorter period T_u with Prewarp-tustin transformation, is applied in multirate PWM position control system as Fig. 5.11. The resonance mode can be suppressed with the feedforward controller.

This method can suppress the resonance modes in just proportion because inverse model of the resonance modes is applied. It is not necessary to previously give target trajectories which do not have the primary vibration characteristic as MPVT (minimizing the primary vibration trajectory) in [37].

Table 5.2: Output vector and switching time.

Region	I	II	III
$V_{i,j}$	$V_{1,2}$	$V_{3,2}$	$V_{3,4}$
ΔT_i	$\Delta T_\alpha - \frac{\Delta T_\beta}{\sqrt{3}}$	$-\Delta T_\alpha + \frac{\Delta T_\beta}{\sqrt{3}}$	$\frac{2\Delta T_\beta}{\sqrt{3}}$
ΔT_j	$\frac{2\Delta T_\beta}{\sqrt{3}}$	$\Delta T_\alpha + \frac{\Delta T_\beta}{\sqrt{3}}$	$-\Delta T_\alpha - \frac{\Delta T_\beta}{\sqrt{3}}$
Region	IV	V	VI
$V_{i,j}$	$V_{5,4}$	$V_{5,6}$	$V_{1,6}$
ΔT_i	$-\frac{2\Delta T_\beta}{\sqrt{3}}$	$-\Delta T_\alpha - \frac{\Delta T_\beta}{\sqrt{3}}$	$\Delta T_\alpha + \frac{\Delta T_\beta}{\sqrt{3}}$
ΔT_j	$-\Delta T_\alpha + \frac{\Delta T_\beta}{\sqrt{3}}$	$\Delta T_\alpha - \frac{\Delta T_\beta}{\sqrt{3}}$	$-\frac{2\Delta T_\beta}{\sqrt{3}}$

Table 5.3: Order of output vector.

Region	Order of output vector
I	$V_0 \to V_1 \to V_2 \to V_1 \to V_0$
II	$V_0 \to V_3 \to V_2 \to V_3 \to V_0$
III	$V_0 \to V_3 \to V_4 \to V_3 \to V_0$
IV	$V_0 \to V_5 \to V_4 \to V_5 \to V_0$
V	$V_0 \to V_5 \to V_6 \to V_5 \to V_0$
VI	$V_0 \to V_1 \to V_6 \to V_1 \to V_0$

Moreover, PTC method assures output errors are perfectly zeros per longer period T_r in ideal condition as the nominal plant. The period T_r of the system applied VSF is shorter than one of vibration suppression PTC in [38] by $n_v T_u$ (n_v: the order of considering resonance modes). It is very important in the case of positioning in several sampling periods.

As above, vibration suppression control can be achieved easily and efficiently by considering the anti-resonance mode.

5.6 Simulations

In the specification of Table 5.4, simulations of ultrahigh-speed nanoscale positioning are performed. In the table, t_d is the positioning time, and A^{ref} is the target position. The target position trajectory is based on a 5-order polynomials. Here, position error tolerance is defined as 100 nm. Multirate PWM position control was compared with original PTC based on the discrete model by zero-order hold. The input voltage V_{dc} of the three-phase

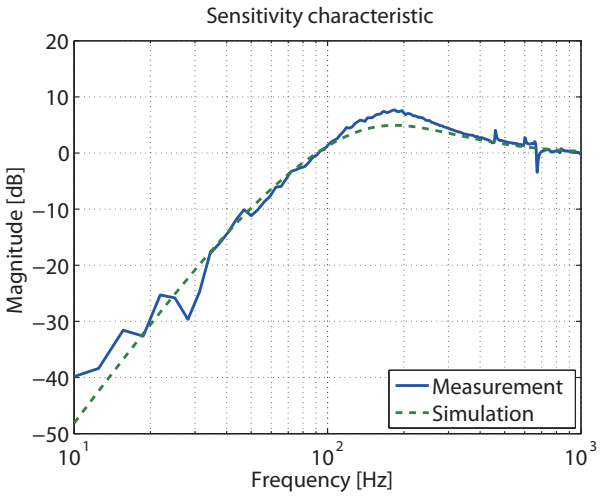

Figure 5.9: Sensitivity characteristic.

inverter is 60 V.

Simulation results of Spec. 1 are shown in Fig. 5.12. In Spec. 1 of 20 ms positioning, all methods can achieve the position error tolerance. Especially, "Proposed" is better in transient response.

Simulation results of Spec. 2 are shown in Fig. 5.13 and 5.14. In Spec. 2 of 2 ms positioning, all methods can achieve the position error tolerance as Spec. 1. Considering more precise plant model, the transient response is better. However, residual vibrations exist in all methods because of resonance mode at 670 Hz.

In Fig. 5.14 with VSF, good positioning can be achieved without residual vibrations. "Proposed + VSF" can achieve the best tracking control in transient and after positioning. Then, these PWM pulses in q axis are shown in Fig. 5.15. The difference between these PWM pulses occures as the modeling error.

In simulation, the primary resonance and the anti-resonance mode are only considered. In the real stage, a lot of high-order resonance modes exist. These resonance modes influence the positioning in experiments.

5.7 Experiments

In the specification of Table 5.4, experiments of ultrahigh-speed nanoscale positioning are performed.

Experimental results of Spec. 1 are shown in Fig. 5.16. In Spec. 1 of 20 ms positioning, all methods can achieve the position error tolerance.

Experimental results of Spec. 2 are shown in Fig. 5.17 and 5.18. In Spec. 2 of 2 ms positioning, "Proposed" and "Conventional 2" can achieve the position error tolerance.

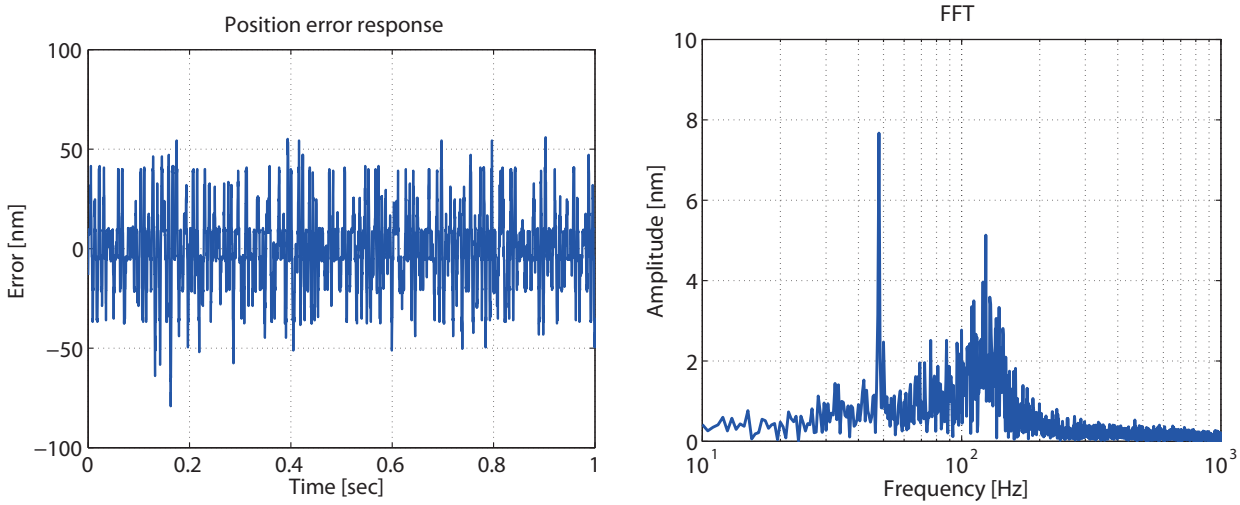

(a) Time response

(b) Spectrum

Figure 5.10: Steady-state error.

However, residual vibrations exist in all methods because of resonance mode at 670 Hz.

In Fig. 5.18 with VSF, good positioning can be achieved without residual vibrations as simulations. Moreover, "Proposed" is better than "Conventional 2" in Fig. 5.17 and 5.18 because of considering the PWM hold and the current loop in the same way as the simulation.

The motor drive has also the problem of dead-time effects in PWM inverters [39]. In the experiments, the dead-time compensation is applied in the current control input [39]. In practice, plant variations and the resonance mode influence the position error sensitively.

5.8 Summary

In this chapter, multirate PWM control considering resonance mode for more precise positioning is proposed. Simulations and experiments are performed to show the advantages of the proposed method. The proposed method can achieve vibration suppression control easily and efficiently by considering the anti-resonance mode.

The proposed method can also cut down the positioning time if the input saturation does not occure in theory. It is expected that this method is applied to high-rigid stages like IC exposure systems.

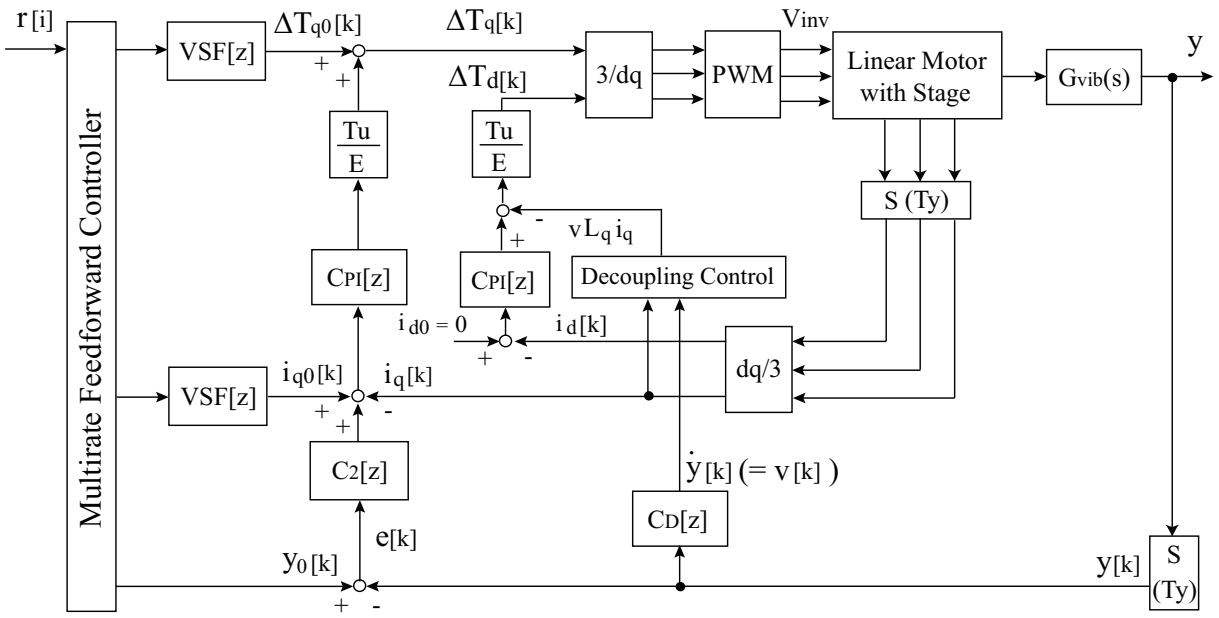

Figure 5.11: Multirate PWM position control system with VSF.

Table 5.4: Sampling periods and target trajectory.

Spec. 1

	T_r	T_u	T_y	t_d	A^{ref}
Conventional 1	0.4 ms	0.2 ms	0.2 ms	20 ms	1.5 μm
Conventional 2	0.6 ms	0.2 ms	0.2 ms	20 ms	1.5 μm
Proposed	0.6 ms	0.2 ms	0.2 ms	20 ms	1.5 μm

Spec. 2

	T_r	T_u	T_y	t_d	A^{ref}
Conventional 1	0.4 ms	0.2 ms	0.2 ms	2 ms	1.5 μm
Conventional 2	0.6 ms	0.2 ms	0.2 ms	2 ms	1.5 μm
Proposed	0.6 ms	0.2 ms	0.2 ms	2 ms	1.5 μm

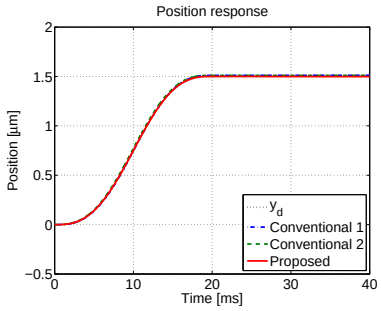

(a) Position response

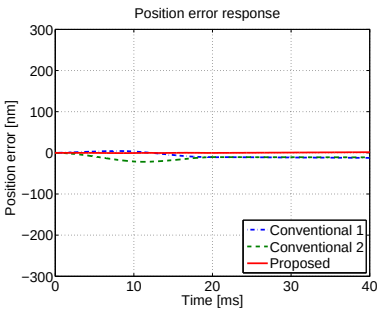

(b) Position error response

Figure 5.12: Simulation results of Spec. 1.

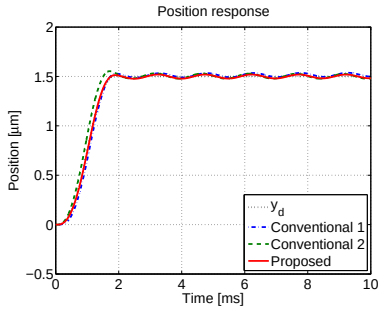

(a) Position response

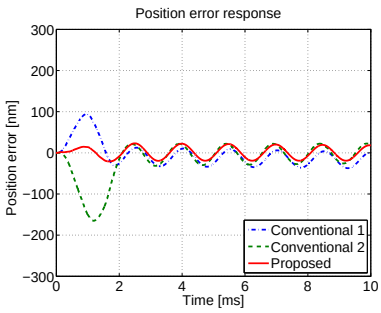

(b) Position error response

Figure 5.13: Simulation results 1 of Spec. 2.

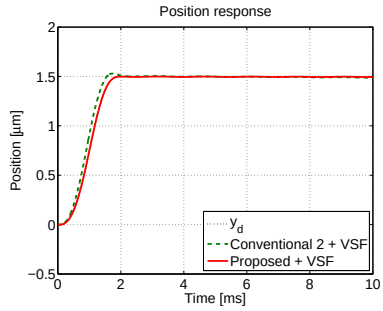

(a) Position response

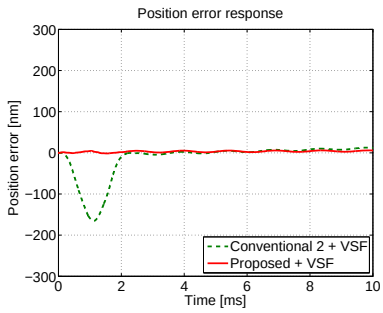

(b) Position error response

Figure 5.14: Simulation results 2 of Spec. 2.

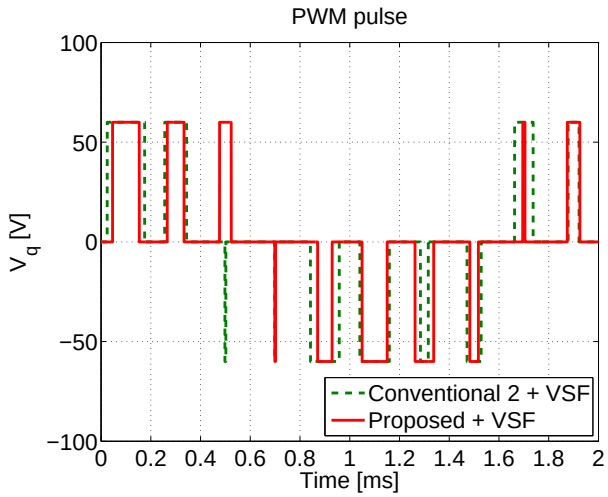

Figure 5.15: PWM pulse of simulation results 2 of Spec. 2.

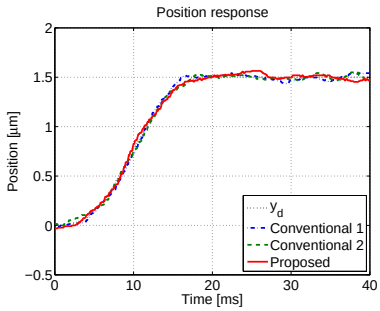

(a) Position response

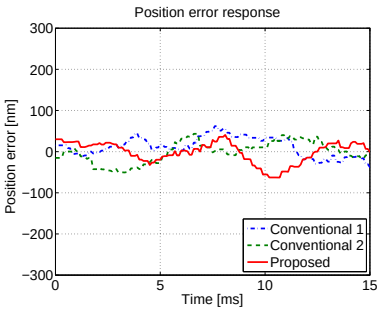

(b) Position error response

Figure 5.16: Experimental results of Spec. 1.

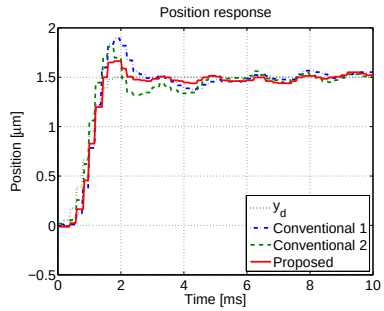

(a) Position response

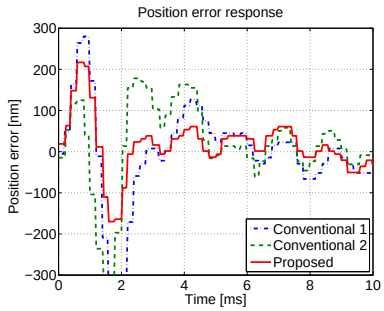

(b) Position error response

Figure 5.17: Experimental results 1 of Spec. 2.

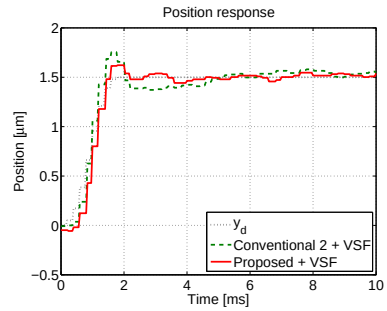

(a) Position response

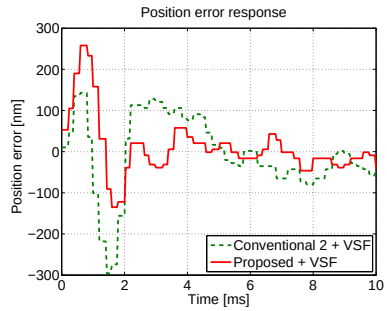

(b) Position error response

Figure 5.18: Experimental results 2 of Spec. 2.

Chapter 6

Enhanced Speed and Current Control by PTC and Robustness Theoretical Analysis

6.1 Abstract

Speed and current closed loops control represent the heart of any advanced AC servo drive. These inner loops usually feature high-dynamic feedback control, with possible axes decoupling and a straight feedforward action of the back-electromotive force (back-EMF). More sophisticated techniques such as single-rate or multirate control could be applied for both speed and current closed loops, and their performances are compared to those of the classic cascade feedback controllers. This represents the goal of the present work, focusing on permanent magnet synchronous motor (PMSM) drives.

6.2 Introduction

PMSM drives for industrial applications usually feature a classic cascade structure, with an inner current control loop and an outer speed control loop. Usually, the regulators are simple PI controllers, designed in order to satisfy the specific requirements such as bandwidth and phase margin.

In the recent past years, new keen control strategies and approaches emerged. Robust control using a disturbance observer [40] and adaptive control using a self-tuning regulator [41] have improved the speed control. The current control has also been improved [42]. These are all feedback approaches.

Then, two-degrees-of-freedom (2-DOF) systems which consist of not only feedback controllers but also feedforward controllers are capable of superior tracking performances with

respect to classical cascade systems. One example is represented by the perfect tracking control (PTC) strategy [20], which is a well-known theory for the design of 2-DOF systems.

Performances of the PTC for the outer control loops, such as the speed loop, have been reported in previous works as [20] and [29]. Usually, since the controlled system is described by a transfer function with relative degree equal or greater than two, a multirate approach is needed to design a feedforward controller and guarantee perfect tracking [20]. No extended investigations are reported so far for the case of single-rate feedforward approaches, where the relative degree of the transfer function is equal to one. This is the case of the inner current control loop of a PMSM drive.

The hypothesis being presented in this work is that some of the advantages of PTC can be profitably shifted to the inner control loop, namely the current one. The combination of single-rate feedforward for the control loop and multirate feedforward for the speed loop can improve performances with respect to classical cascade feedback approaches. The chapter gives the evidence of unabated speed and current tracking capability of the proposed approach with reduced PWM carrier frequency, with evident energy saving with respect to a high-bandwidth cascade feedback controller with higher PWM carrier frequency.

The chapter illustrates the mathematical passages and the needed background on PTC single-rate and multirate approaches, and it contains experimental results on a PMSM drive. First, the cascade current feedback control is redesigned based on pole placement theory. Then, a single-rate feedforward controller is designed for the current control. The carrier frequency is decreased for the system with the feedforward controller, showing that tracking performances are the same as the classical cascade approach with higher carrier frequency. The PMSM drive is completed with the PTC multirate control applied to the outer speed loop. The robustness of the PTC multirate feedforward controller is verified both theoretically and experimentally.

6.3 Improvements of q Axis Current Control

In the first part of the work, a single-rate feedforward controller along with a classic feedback controller were applied for the q-axis control of a PMSM, whose data are shown in Table 6.1. A block scheme of a 2-DOF control system, composed by a single-rate feedforward controller $C_1[z]$ and a feedback controller $C_2[z]$, is shown in Fig. 6.1. The S block represents the sample-and-hold operation where T_s is the PWM sample time, while the presence of the delay between $r[k]$ and $y_d[k]$ will be cleared in the next Section 6.3.2.

Table 6.1: PMSM parameters.

Inductance L	130	mH
Resistance R	5.15	Ω
Inertia J	4.0×10^{-4}	kg·m^2
Viscosity B	3.0×10^{-3}	kg/(m·s)
Torque coefficient K_t	0.44	mN·m/A
Back-EMF constant K_e	0.22	V· s/rad

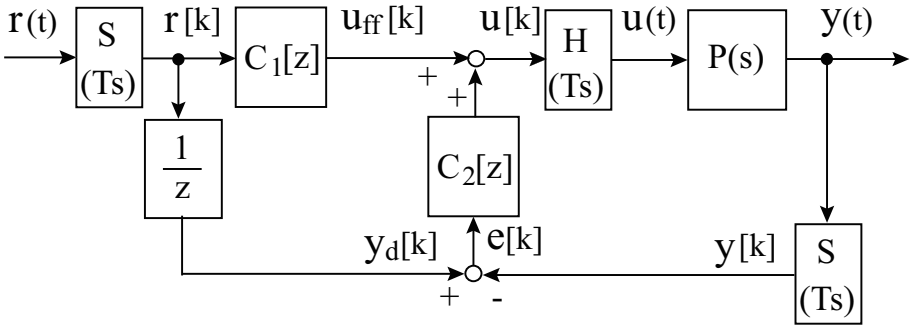

Figure 6.1: 2-DOF control system in singlerate.

6.3.1 Design of Feedback Controller

A block diagram which comprises the current q axis of a PMSM and the mechanical system is shown in Fig. 6.2.

Usually, the feedback controller is designed without taking into account the back-EMF term, so that the considered plant model for the design of $C_2[z]$ is:

$$P_{i1}(s) = \frac{i}{V} = \frac{1}{Ls + R}. \tag{6.1}$$

Here, a feedback controller is designed as

$$C_{i2}(s) = \frac{Ls + R}{\tau_i s}, \tag{6.2}$$

so that the closed-loop transfer function from the reference current and the actual current, neglecting the back-EMF term, is equal to

$$\frac{i}{i^{ref}} = \frac{1}{\tau_i s + 1}, \tag{6.3}$$

where $\tau_i = 1/(2\pi f_i)$. The parameter f_i is selected as the bandwidth of the current loop. In the classic approach, the coupling term due to the back-EMF is rejected by a general decoupling control, which consists of adding to the voltage V a term equal to $K_e\omega$.

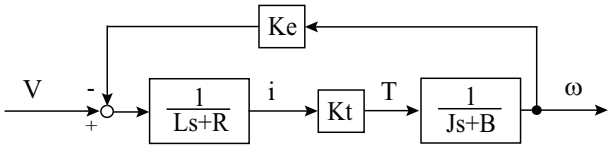

Figure 6.2: Plant model of PMSM in q axis.

6.3.2 Design of Feedforward Controller

The feedforward component $C_1[z]$ of Fig. 6.1 was designed with a current model that considers the back-EMF effect. In this case, the transfer function from voltage to current, described in Fig. 6.2, is:

$$P_i(s) = \frac{i}{V} = \frac{Js + B}{LJs^2 + (RJ + LB)s + RB + K_t K_e}. \tag{6.4}$$

The plant model $P_i(s)$ is discretized by a zero-order-hold (ZOH) discretization without unstable zeros, obtaining a discrete plant model named $P_i[z]$. The feedforward controller is then designed as:

$$C_{i1}[z] = \frac{1}{zP_i[z]}, \tag{6.5}$$

where one delay operator z is needed for the feedforward controller $C_1[z]$ to be a biproper transfer function. Thus, when plant is nominal,

$$y[k] = \frac{1}{z} r[k]. \tag{6.6}$$

Here, if the reference $r[k]$ of $C_1[z]$ is equal to the desired output $y_d[k+1]$ of Fig. 6.1, perfect tracking is achieved as

$$y_d[k] = y[k], \tag{6.7}$$

in singlerate.

In the previous literature [43], a multirate feedforward controller was designed from the precise plant model including back-EMF term. However, in this case a stable single-rate feedforward controller can be designed and applied. The reason is that a single-rate approach is not only easier, but it can also guarantee perfect tracking for a smaller sample time.

6.3.3 Experiments

First, the target trajectory of the current was set as a sinusoidal wave with a frequency of 100 Hz. Two control systems consisting of only feedback controls were performed, one with a bandwidth of 1000 Hz and the other with a bandwidth of 100 Hz. Here, the decoupling

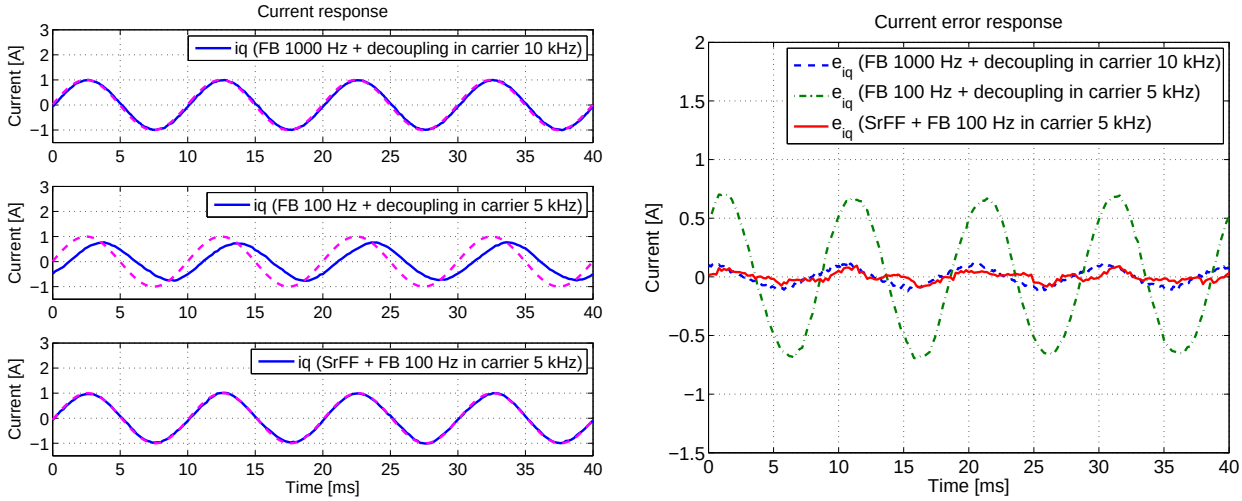

(a) Currents (b) Current errors

Figure 6.3: Current control experimental results: sinusoidal reference.

control to suppress the back-EMF term is employed in both control systems. Results are shown in the two upper plots of Fig. 6.3.

The tracking performance of the feedback control, whose bandwidth is 1000 Hz, is remarkable, while that with a 100-Hz bandwidth is poor. A delay of 45 degrees and an attenuation of 3 dB are observed, as theoretically predictable because of the reference frequency of 100 Hz. Carrier frequencies were also artificially modified, using a 10 kHz carrier for the 1000-Hz bandwidth system and a 5 kHz carrier for the 100-Hz bandwidth system.

In the third plot of Fig. 6.3, a 2-DOF system which consists of the 100-Hz-bandwidth feedback controller and the single-rate feedforward controller was applied. Carrier frequency was set to 5 kHz. Performances of the 2-DOF system are comparable or better than those of the system with the 1000-Hz-bandwitdh feedback controller.

The same experiment was repeated using a different current reference, that was a first-order delayed step-type trajectory, in order to test the transient response. The time constant of the trajectory is equal to 1 ms. Results are shown in Fig. 6.4.

Again, the performances of the 2-DOF system with low-bandwidth feedback and feedforward are superior with respect to the low-bandwidth case. As before, they are comparable to those of the feedback controller with high bandwidth. The main advantage, however, is that the carrier frequency was halved, with evident energy saving. A bandwidth of 1000 Hz for the classic feedback controller cannot be practically achieved for a system with 5-kHz carrier frequency, so performances of the classic approach would have not been the same as the ones of the feedforward approach.

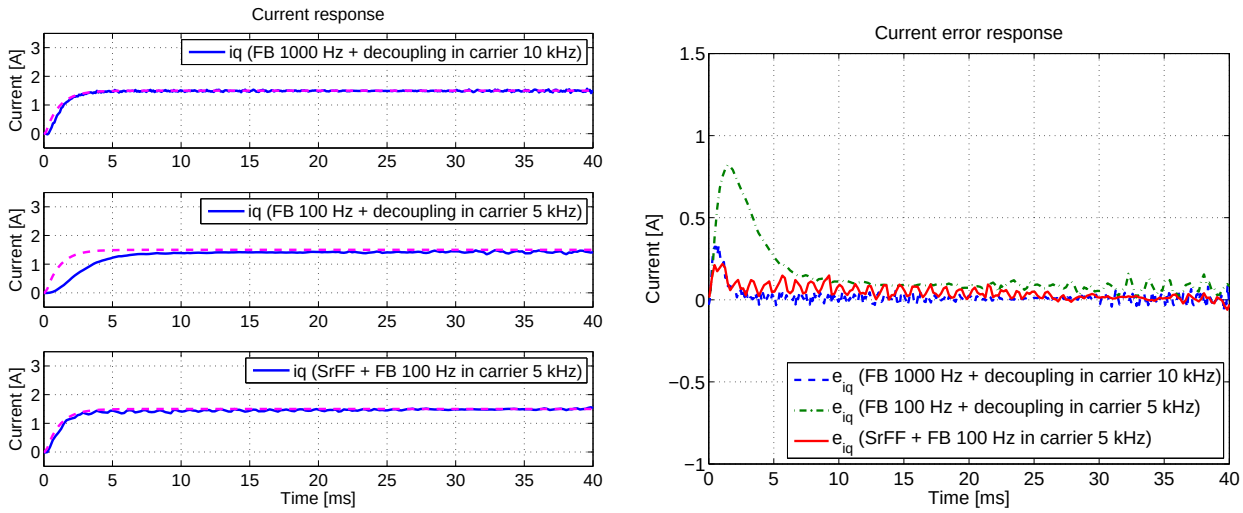

(a) Currents (b) Current errors

Figure 6.4: Experimental results 2 of current control.

6.4 Improvement of Speed Control

Considering again Fig. 6.2, the transfer function from the voltage V to the mechanical speed w is:

$$P_\omega(s) = \frac{\omega}{V} = \frac{K_t}{LJs^2 + (RJ + LB)s + RB + K_t K_e}. \tag{6.8}$$

Here, the discrete plant by ZOH has an almost unstable zero, because the relative degree of the transfer function is equal to two. If a single-rate feedforward controller was designed, the input would have led to vibrations and unwanted oscillations. The inverse system of the plant cannot be applied in single-rate discrete-time [23]. Therefore, the multirate technique is needed to design a feedforward controller for perfect tracking.

6.4.1 Design of Feedback Controller

Considering a perfect tracking from the current reference to the actual current, the speed plant model is:

$$P_{\omega 1}(s) = \frac{\omega}{i^{ref}} = \frac{K_t}{Js + B}. \tag{6.9}$$

The feedback controller is then designed as

$$C_{\omega 2}(s) = \frac{Js + B}{K_t \tau_\omega s}, \tag{6.10}$$

so that the closed-loop transfer function from the speed reference to the actual speed is

$$T_\omega(s) = \frac{\omega}{\omega^{ref}} = \frac{1}{\tau_\omega s + 1}, \tag{6.11}$$

where $\tau_\omega = 1/(2\pi f_\omega)$. The parameter f_ω is selected as the bandwidth of the speed loop.

6.4.2 Control System Design

PTC is applied to a control system which consists of a cascade feedback for the current loop and the velocity loop.

The controllable canonical form of (6.8) is given by

$$\dot{\boldsymbol{x}}(t) = \boldsymbol{A}_c\boldsymbol{x}(t) + \boldsymbol{b}_c u(t)\ ,\ y(t) = \boldsymbol{c}_c\boldsymbol{x}(t), \tag{6.12}$$

$$\left[\begin{array}{c|c} \boldsymbol{A}_c & \boldsymbol{b}_c \\ \hline \boldsymbol{c}_c & 0 \end{array}\right] = \left[\begin{array}{cc|c} 0 & 1 & 0 \\ -\dfrac{RB + K_tK_e}{LJ} & -\dfrac{RJ + LB}{LJ} & \dfrac{K_t}{LJ} \\ \hline 1 & 0 & 0 \end{array}\right], \tag{6.13}$$

where $\boldsymbol{x} = [\omega\ \dot{\omega}]^T$. The multirate feedforward controller is designed by discretizing (6.12) with sampling period T_u, and setting $T_u = T_y = T_r/2$. Matrices $\boldsymbol{A}$, $\boldsymbol{B}$, $\boldsymbol{C}$, and $\boldsymbol{D}$ are designed according to (2.2).

In order to obtain the the nominal current i_0 to feed the inner current feedback controller, two matrices $\boldsymbol{C'}$ and $\boldsymbol{D'}$ are introduced, using (2.2) and the output equation of the current plant model (6.4):

$$y = \boldsymbol{c}_c'\boldsymbol{x},\ \boldsymbol{c}_c' = \left[\begin{array}{cc} \frac{B}{K_t} & \frac{J}{K_t} \end{array}\right]. \tag{6.14}$$

Fig. 6.5 shows the complete proposed system. Again, feedback current controller $C_{i2}[z]$ and feedback velocity controller $C_{\omega 2}[z]$ work only when parameter mismatches occur.

6.4.3 Experiments

Experiments were performed in order to compare the proposed system with the conventional cascade feedback system. The target speed trajectory was set as a third-order polynomial, and carrier and control period were both set to 140 μs. Bandwidth of the current loop was set to 100 Hz, while that of the speed loop was set to 10 Hz.

Fig. 6.6 shows the experimental results. The proposed system shows better performances with respect to the conventional approach. In detail, two samples delay occurs in order to calculate the real speed by difference between two positions. Therefore, the target trajectory of Fig. 6.6 and the nominal speed $\omega_0[k]$ of Fig. 6.5 are delayed by two samples.

6.4.4 Robustness of multirate Feedforward Controller

The robustness of the multirate feedforward controller of PTC was experimentally verified. Each parameter used to design the multirate feedforward controller was changed from -50%

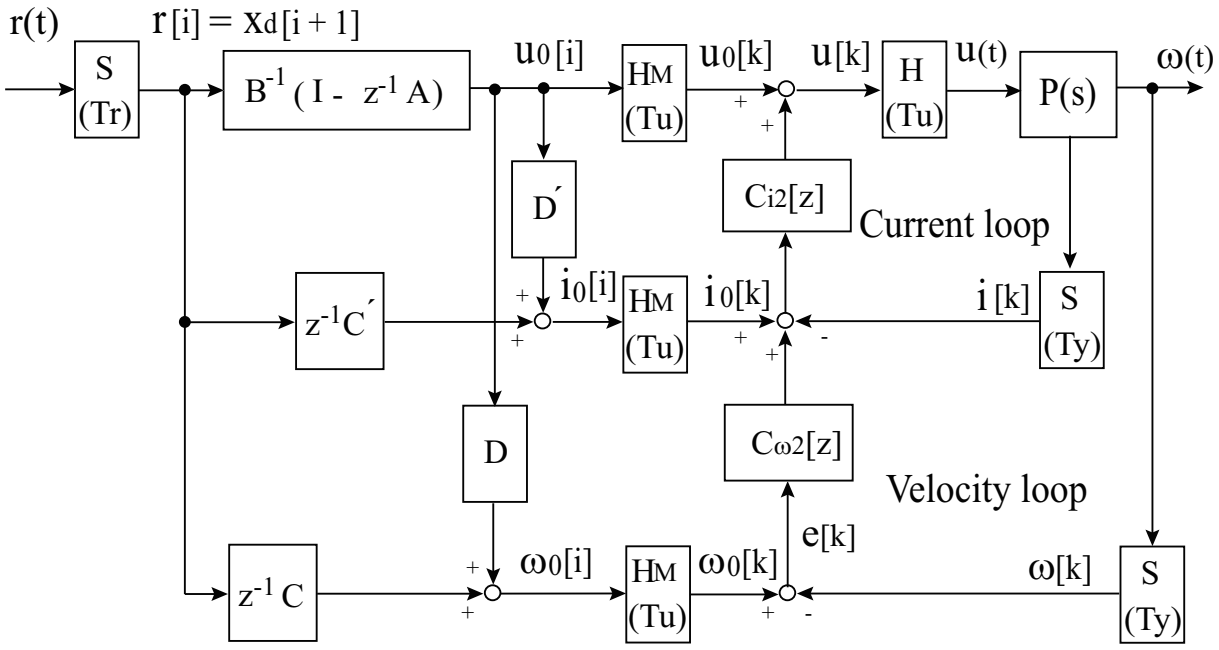

Figure 6.5: Proposed control system.

to +50% of its nominal value, while the feedback controllers were not changed. Fig. 6.7 shows the obtained results: the most sensitive parameter is the torque constant K_t ($= 2K_e$), while the load inertia J is second one. Variation of the inductance L is the third sensitive parameter, while the controller was robust against the variations of the viscosity B and the resistance R.

6.4.5 Robustness Theoretical Analysis

A theoretical approach to the robustness of the proposed control system was performed. Fig. 6.8 shows the block scheme of the control system simplified in the continuous time domain.

$P_{iu}(s)$ from the input to the current is equal to (6.4) and $P_{\omega i}(s)$ is equal to (6.9). It is assumed that nominal stable inverse systems $P_{iun}^{-1}(s)$ and $P_{\omega in}^{-1}(s)$ can be designed.

The tracking characteristic from the reference to the output is represented by (neglecting the dependence on s):

$$\frac{\omega}{r} = \frac{P_{\omega i}P_{iu}(C_iC_\omega + C_iP_{\omega in}^{-1} + P_{\omega in}^{-1}P_{iun}^{-1})}{P_{\omega i}P_{iu}C_iC_\omega + P_{iu}C_i + 1}. \tag{6.15}$$

If the plant is nominal ($P_{iu} = P_{iun}$ and $P_{\omega i} = P_{\omega in}$), perfect tracking is achieved ($\omega(t) = r(t)$). When parameter mismatches exist, parts of the feedforward inputs u_0 and i_0 are to be considered as disturbances. The input variations are defined as

$$\begin{aligned} \Delta i_0 &= (P_{\omega i}^{-1}(s) - P_{\omega in}^{-1}(s))r, \\ \Delta u_0 &= (P_{\omega i}^{-1}(s)P_{iu}^{-1}(s) - P_{\omega in}^{-1}(s)P_{iun}^{-1}(s))r. \end{aligned} \tag{6.16}$$

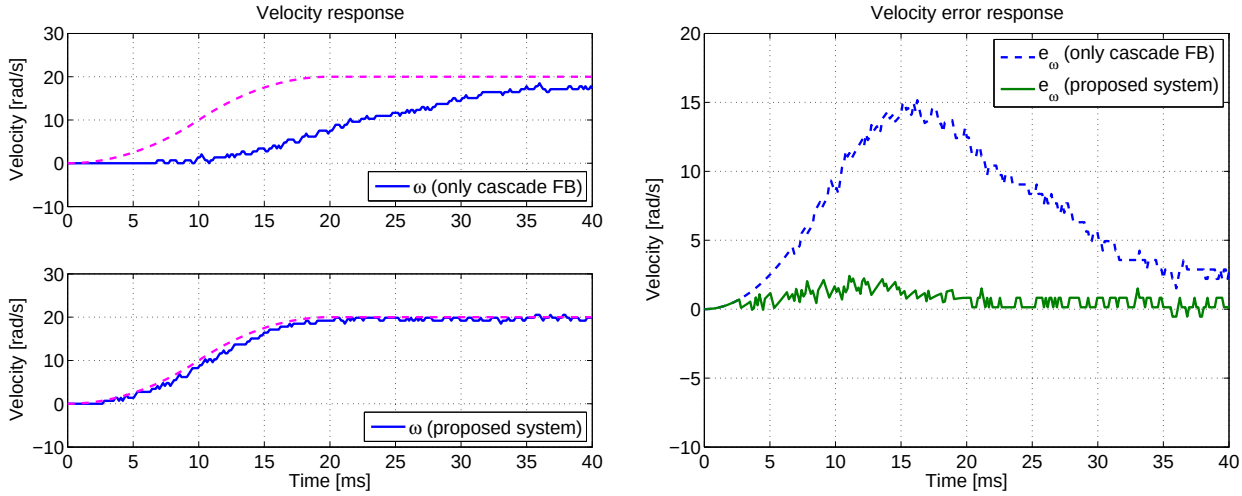

(a) Velocities (b) Velocity errors

Figure 6.6: Speed control experimental results.

In case of an inertia J variation of +50% with respect to its nominal value, the magnitude of the Bode diagrams of the variations (6.16) are shown in Fig. 6.9. Speed control and current control bandwidths have been set to 10 Hz and 100 Hz, respectively.

The transfer functions from the input variations to the speed are

$$\begin{aligned} \frac{\omega}{\Delta i_0} &= \frac{P_{\omega i}(s)P_{iu}(s)C_i(s)}{P_{\omega i}(s)P_{iu}(s)C_i(s)C_\omega(s)+P_{iu}(s)C_i(s)+1}, \\ \frac{\omega}{\Delta u_0} &= \frac{P_{\omega i}(s)P_{iu}(s)}{P_{\omega i}(s)P_{iu}(s)C_i(s)C_\omega(s)+P_{iu}(s)C_i(s)+1}. \end{aligned} \tag{6.17}$$

The Bode diagram magnitudes of the (6.17) are shown in Fig. 6.10 (a). The disturbance suppression could be better in plant-pole cancellation feedback control: this is due to the fact that the plant has a low mechanical pole (-J/B).

In order to improve robustness, the speed PI controller $C_{\omega 2}(s)$ of (6.10) is redesigned without plant-pole cancellation as in (6.9), using the following expressions:

$$C_{\omega 2}(s) = K_p + \frac{K_i}{s}, \tag{6.18}$$

$$K_p = \frac{2\zeta_{cl}\omega_{cl}J - B}{K_t} \ , \ K_i = \frac{J\omega_{cl}^2}{K_t}. \tag{6.19}$$

With this choice, the closed-loop characteristic polynomial of the speed loop is given by

$$A_{cl}(s) = s^2 + 2\zeta_{cl}\omega_{cl}s + \omega_{cl}^2. \tag{6.20}$$

where the damping factor ζ_{cl} was set to 1, and $\omega_{cl} = 2\pi f_\omega$ where f_ω is the bandwidth of the speed loop. The disturbance suppression responses without plant-pole cancellation are shown in Fig. 6.10 (b).

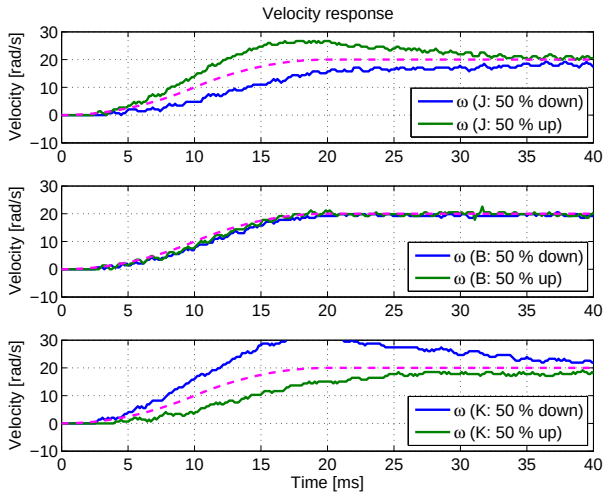

(a) Changed J, B and K_t ($= 2\ K_e$))

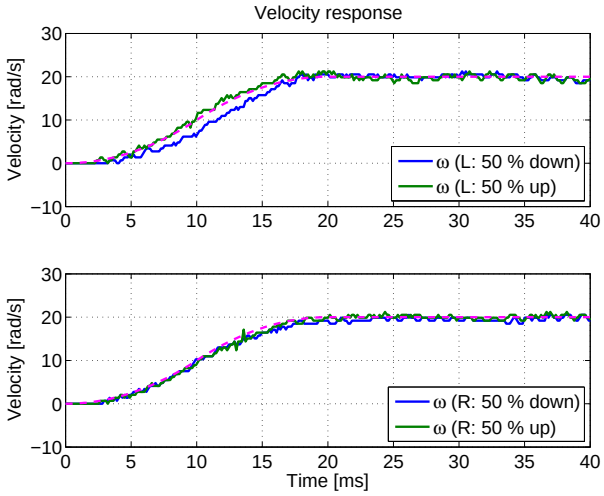

(b) Changed L and R)

Figure 6.7: Experimental robustness of the multirate feedforward control.

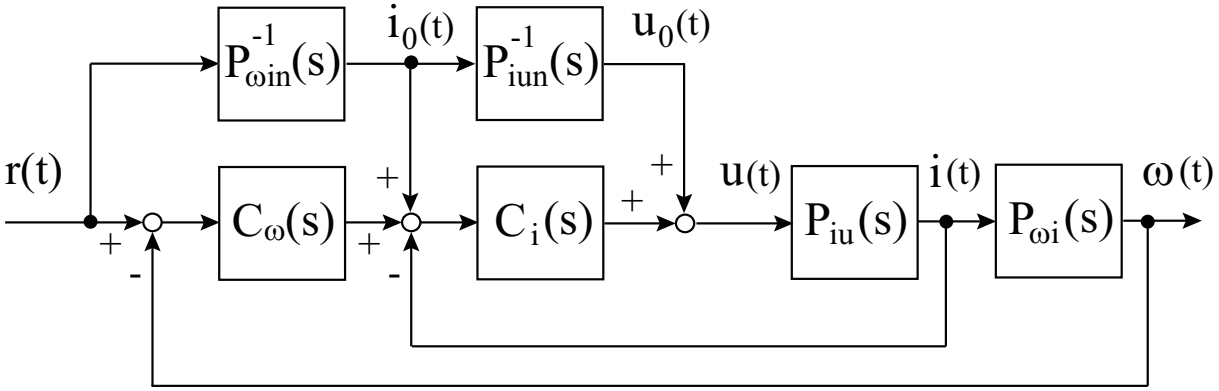

Figure 6.8: Proposed control system simplified in the continuous time domain.

The disturbance suppression is better than the one with plant-pole cancellation. This is also proved by comparing the time responses (Fig. 6.11).

Finally, although stability margin is worse as shown in Fig. 6.12 and 6.13, the feedback without plant-pole cancellation still has enough stability margin in the case of an inertia variation of +50% with respect to its nominal value.

6.5 Summary

A single-rate feedforward control has been designed, along with a classic feedback control, in order to achieve perfect tracking for the inner current control loop of a PMSM drive. Results shows that in case of single-rate feedforward control the carrier frequency could be decreased

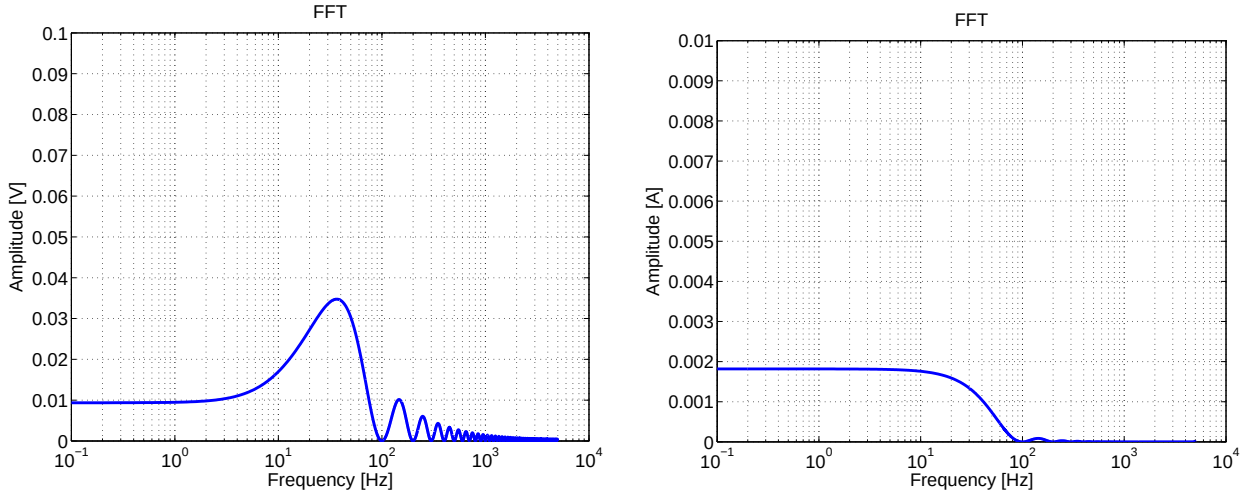

(a) Δu_0 (b) Δi_0

Figure 6.9: Bode diagram magnitude of Δu_0 and Δi_0 (J: +50% of nominal value).

to obtain the same performances of conventional cascade feedback approaches, with evident energy savings.

The speed loop was improved by adding a multirate feedforward controller. Tracking performances were dramatically enhanced with respect to the conventional approach. Robustness of the multirate control against parameter variations was tested experimentally, and some hints on the theoretical approach to the robustness analysis were provided.

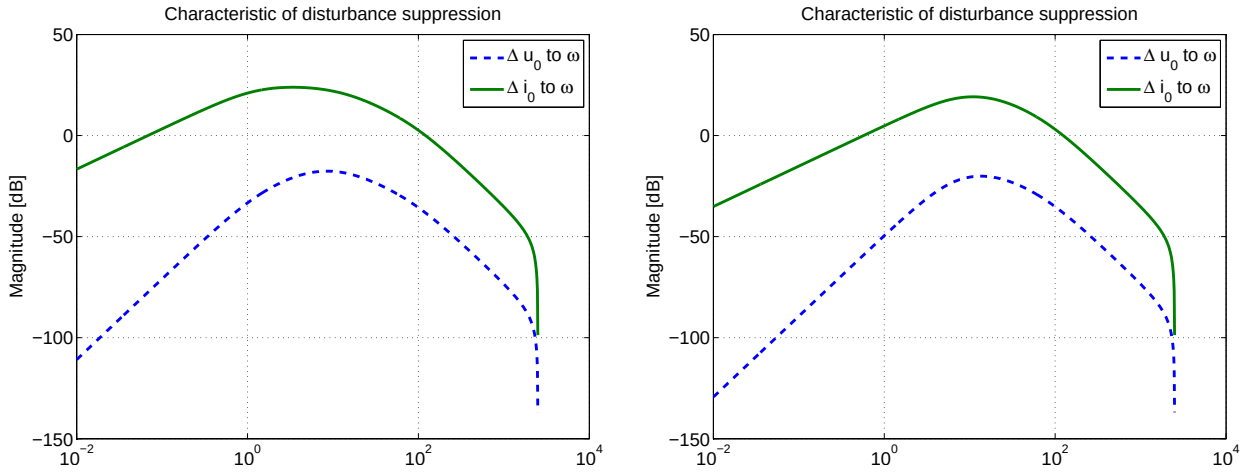

(a) with plant-pole cancellation (b) w/o plant-pole cancellation

Figure 6.10: Disturbance suppression transfer functions.

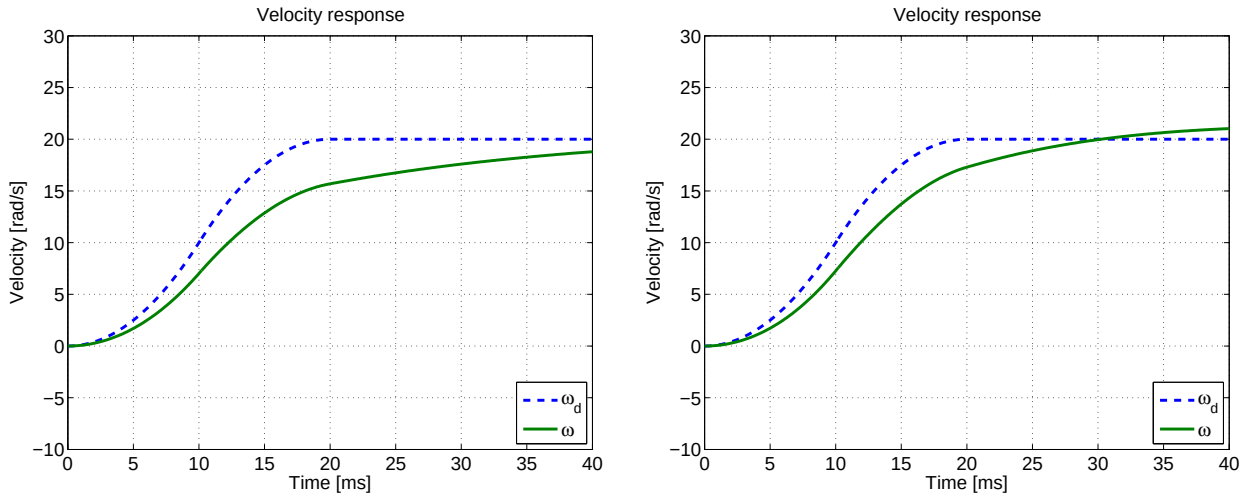

(a) With plant-pole cancellation (b) Without plant-pole cancellation

Figure 6.11: Time responses (J: +50% of nominal value).

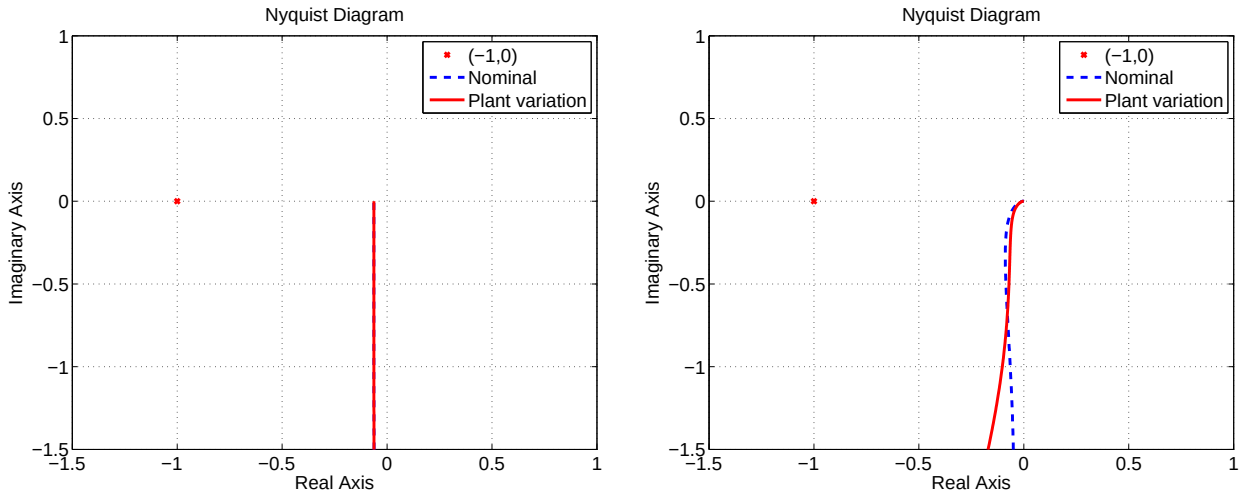

(a) Current loop (b) Velocity loop

Figure 6.12: Nyquist diagrams (with plant-pole cancellation).

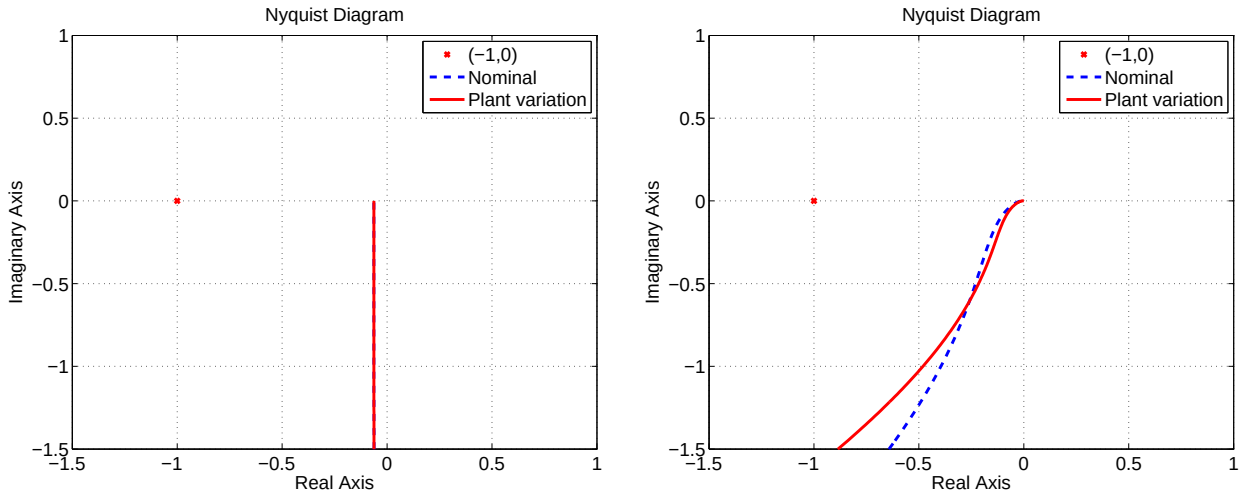

(a) Current loop (b) Velocity loop

Figure 6.13: Nyquist diagrams (without plant-pole cancellation).

Chapter 7

Quantization Error Reduction based on Multirate Control

7.1 Abstract

High resolution encoders are employed to industrial equipment which requires accuracy, for example, NC machine tools, exposure systems, and so on. Generally, the velocity of machines is calculated by the difference of the position given by the encoder. Although the high resolution encoder is employed, the quantization error and the half sample delay induced by the difference cannot be avoided. These can be problems in control systems requiring high precise velocity. In this chapter, an observer which can estimate state variables with reducing the quantization error is proposed. Finally, simulations and experiment with experimental precision stages are performed to show the advantages of the proposed observer.

7.2 Introduction

In robots and industrial equipment, the velocity is generally obtained from the positional information of the encoder. However, the quantization error of the encoder influences the control performance [44].

There are several common methods without plant model in order to measure a velocity from an encoder. T method measures periods between encoder pulses. M method measures encoder pulses generated in sampling periods. Moreover, M/T method [45], [46] combined with the two methods can measure the high precise velocity in the low speed range. S method [47], [48] which measures the velocity, synchronizing with the variation of the number of pulses has high accuracy in the all speed ranges. However, these methods measure the velocity delayed at least half sample because of the difference of the position information.

There are also methods with observer which can estimate velocity without delay [49].

Instantaneous speed observer [50] can estimate the velocity between the sampling periods based on the plant model in the long sampling period to keep high accuracy of reading the encoder information.

High resolution encoders are employed to industrial equipment which is required accuracy, for example, NC machine tools, exposure systems, and so on. Although the high resolution encoder is employed, the quantization error and the half sample delay induced by the difference cannot be avoided. These are problems in the case of required high precise velocity. In this chapter, an observer which can estimate state variables with reducing the quantization error is proposed. Finally, simulations and experiment with an experimental precision stage are performed to show the advantages of the proposed observer.

7.3 Derivation with Moving Difference

Half sample delay is occurred when the velocity is derived from difference between the sensor position of the current sample and the sensor position before one sample as follows:

$$v_{dif}[k] = \frac{z-1}{zT_u}y[k], \tag{7.1}$$

$$= \hat{v}\left[k-\frac{1}{2}\right]. \tag{7.2}$$

Here, the sensor position y can be separated into the real position y_{real} and the quantization error q as

$$y[k] = y_{real}[k] + q[k]. \tag{7.3}$$

Therefore, the characteristic from the quantization error to the velocity is also represented by the transfer function of (7.1).

$N/2$ sample delay is occurred when the velocity is derived from difference between the sensor position of the current sample and the sensor position before N sample in order to reduce the quantization error as follows:

$$v_{dif}[k] = \frac{z^N-1}{z^N NT_u}y[k], \tag{7.4}$$

$$= \hat{v}\left[k-\frac{N}{2}\right]. \tag{7.5}$$

7.4 Estimation with Observer

7.4.1 Definition of State Equations of Plant

The continuous time state equation of the plant in a controllable canonical form except dead-times is represented by

$$\begin{cases} \dot{\boldsymbol{x}}_p(t) = \boldsymbol{A}_{cp}\boldsymbol{x}_p(t) + \boldsymbol{b}_{cp}(u(t) - d(t)) \\ y(t) = \boldsymbol{c}_{cp}\boldsymbol{x}_p(t) \end{cases}. \tag{7.6}$$

The continuous time state equation of the disturbance is represented by

$$\begin{cases} \dot{\boldsymbol{x}}_d(t) = \boldsymbol{A}_{cd}\boldsymbol{x}_d(t) \\ d(t) = \boldsymbol{c}_{cd}\boldsymbol{x}_d(t) \end{cases}. \tag{7.7}$$

The augmented continuous time state equation can be represented by

$$\begin{cases} \dot{\boldsymbol{x}}(t) = \boldsymbol{A}_c\boldsymbol{x}(t) + \boldsymbol{b}_c u(t) \\ y(t) = \boldsymbol{c}_c\boldsymbol{x}(t) \end{cases}, \tag{7.8}$$

$$\left[\begin{array}{c|c} \boldsymbol{A}_c & \boldsymbol{b}_c \\ \hline \boldsymbol{c}_c & \boldsymbol{0} \end{array}\right] \triangleq \left[\begin{array}{cc|c} \boldsymbol{A}_{cp} & -\boldsymbol{b}_{cp}\boldsymbol{c}_{cd} & \boldsymbol{b}_{cp} \\ \boldsymbol{0} & \boldsymbol{A}_{cd} & \boldsymbol{0} \\ \hline \boldsymbol{c}_{cp} & \boldsymbol{0} & \boldsymbol{0} \end{array}\right], \tag{7.9}$$

where $\boldsymbol{x} = [\boldsymbol{x}_p^T, \boldsymbol{x}_d^T]^T$. Then, the augmented discrete time state equation of (7.8) per the sampling period T_u is represented by

$$\begin{cases} \boldsymbol{x}[k+1] = \boldsymbol{A}_s\boldsymbol{x}[k] + \boldsymbol{b}_s u[k] \\ y[k] = \boldsymbol{c}_s\boldsymbol{x}[k] \end{cases}. \tag{7.10}$$

7.4.2 Long Sampling Short Cycle Observer

Long sampling short cycle observer (LSSCO) which is proposed is designed based on a full-order observer. The multirate plant per N times is represented by

$$\boldsymbol{x}[k] = \boldsymbol{A}\boldsymbol{x}[k-N] + \boldsymbol{B}\begin{bmatrix} u[k-N] \\ \vdots \\ u[k-1] \end{bmatrix}, \tag{7.11}$$

where

$$\left[\begin{array}{c|c} \boldsymbol{A} & \boldsymbol{B} \end{array}\right] \triangleq \left[\begin{array}{c|ccc} \boldsymbol{A}_s^N & \boldsymbol{A}_s^{N-1}\boldsymbol{b}_s & \cdots & \boldsymbol{b}_s \end{array}\right], \tag{7.12}$$

from (7.10). The full-order observer can be designed for the multirate plant as

$$\hat{\boldsymbol{x}}[i+1] = \boldsymbol{A}\hat{\boldsymbol{x}}[i] + \boldsymbol{B}\boldsymbol{u}[i] + \boldsymbol{H}(y[i] - \boldsymbol{c}_s\hat{\boldsymbol{x}}[i]), \tag{7.13}$$

where the state $\hat{\boldsymbol{x}}[i]$ is updated per the long sampling NT_u. Here, the difference between sensor position including the quantization error and estimated position in the correction term of the observer is calculated per the long sampling NT_u. Therefore, The effect equivalent to the movement difference per the long sampling NT_u in order to reduce the quantization error is achieved. Besides, $N/2$ sample delay can be avoided.

However, sensor position between NT_u sampling periods is wasted because the information of the encoder is available per the short sampling T_u. Here, if the observer equation (7.13) is updated like moving difference in Fig. 7.1, all data of sensor position can be used effectively. The update equation is represented by

$$\hat{\boldsymbol{x}}[k] = \boldsymbol{A}\hat{\boldsymbol{x}}[k-N] + \boldsymbol{B}\begin{bmatrix} u[k-N] \\ \vdots \\ u[k-1] \end{bmatrix} + \boldsymbol{H}(y[k-N] - \boldsymbol{c}_s\hat{\boldsymbol{x}}[k-N]), \tag{7.14}$$

where the state $\hat{\boldsymbol{x}}[k]$ is updated per the short sampling T_u.

In the same way, LSSCO is designed based on a minimum-order observer. The minimum-order observer can be designed for the multirate plant as

$$\begin{cases} \boldsymbol{\xi}[i+1] = \hat{\boldsymbol{A}}\boldsymbol{\xi}[i] + \hat{\boldsymbol{B}}y[i] + \hat{\boldsymbol{J}}\boldsymbol{u}[i] \\ \hat{\boldsymbol{x}}[i] = \hat{\boldsymbol{C}}\boldsymbol{\xi}[i] + \hat{\boldsymbol{D}}y[i] \end{cases}, \tag{7.15}$$

where the state $\boldsymbol{\xi}[i]$ is updated per the long sampling NT_u. Moreover, The update equation is modified based on Fig. 7.1 as

$$\begin{cases} \boldsymbol{\xi}[k] = \hat{\boldsymbol{A}}\boldsymbol{\xi}[k-N] + \hat{\boldsymbol{B}}y[k-N] + \hat{\boldsymbol{J}}\begin{bmatrix} u[k-N] \\ \vdots \\ u[k-1] \end{bmatrix} \\ \hat{\boldsymbol{x}}[k] = \hat{\boldsymbol{C}}\boldsymbol{\xi}[k] + \hat{\boldsymbol{D}}y[k] \end{cases}, \tag{7.16}$$

where the state $\boldsymbol{\xi}[k]$ is updated per the short sampling T_u. LSSCO based on minimum-order observer is applied below.

7.4.3 Consideration of Dead-time

The output dead-time of the integral multiple n_{do} of the sampling period T_u is considered. In this chapter, the integral multiple case is only explained. In the non-integral multiple case, the output dead-time can be also considered [30]. The states estimated from the output

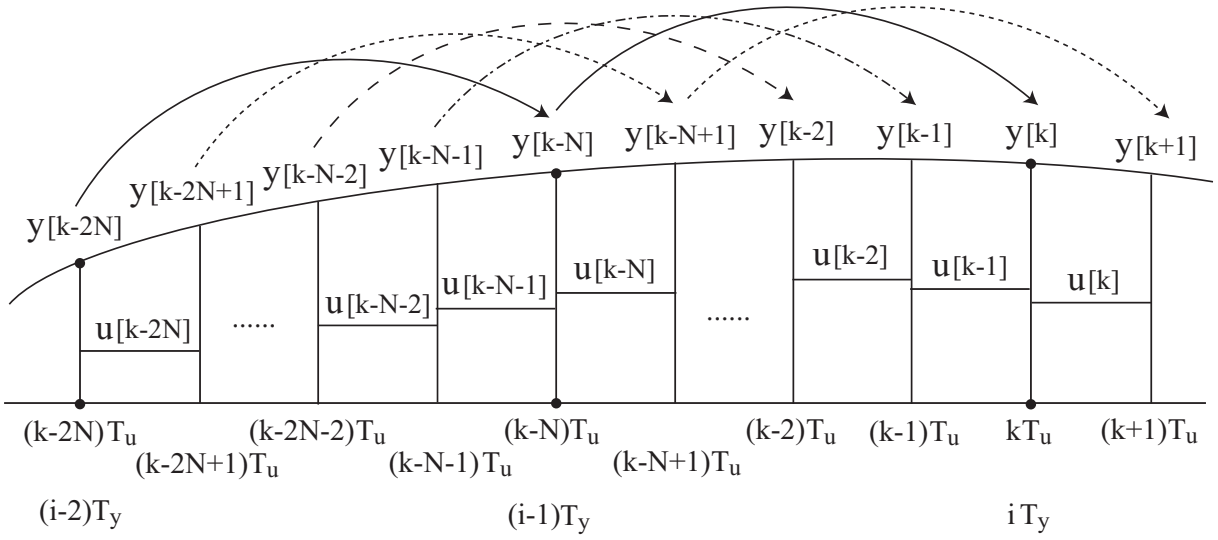

Figure 7.1: Sampling time.

$y[k-n_{do}]$ delayed n_{do} sample by the observer is just $\hat{\boldsymbol{x}}[k-n_{do}]$ delayed n_{do} sample as follows:

$$\begin{aligned}
\boldsymbol{\xi}[k-n_{do}] &= \hat{\boldsymbol{A}}\boldsymbol{\xi}[k-N-n_{do}] + \hat{\boldsymbol{B}}y[k-N-n_{do}] \\
&+ \hat{\boldsymbol{J}}\begin{bmatrix} u[k-N-n_{do}] \\ \vdots \\ u[k-1-n_{do}] \end{bmatrix}, \\
\hat{\boldsymbol{x}}[k-n_{do}] &= \hat{\boldsymbol{C}}\boldsymbol{\xi}[k-n_{do}] + \hat{\boldsymbol{D}}y[k-n_{do}].
\end{aligned} \tag{7.17}$$

Therefore, the estimated states $\hat{\boldsymbol{x}}[k]$ of the current sample can be estimated as

$$\hat{\boldsymbol{x}}[k] = \boldsymbol{A}_1\hat{\boldsymbol{x}}[k-n_{do}] + \boldsymbol{B}_1\begin{bmatrix} u[k-n_{do}] \\ \vdots \\ u[k-1] \end{bmatrix}, \tag{7.18}$$

where

$$\left[\begin{array}{c|c} \boldsymbol{A}_1 & \boldsymbol{B}_1 \end{array}\right] \triangleq \left[\begin{array}{c|cc} \boldsymbol{A}_s^{n_{do}} & \boldsymbol{A}_s^{n_{do}-1}\boldsymbol{b}_s & \cdots \quad \boldsymbol{b}_s \end{array}\right]. \tag{7.19}$$

The proposed LSSCO considering dead-time is shown in Fig. 7.2.

7.5 Simulations

7.5.1 Specifications

The block diagram of the system is shown in Fig. 7.3. The specifications of the plant are shown in Table 7.1. Here, input dead-time is one sampling period, and output dead-time is also one sampling period.

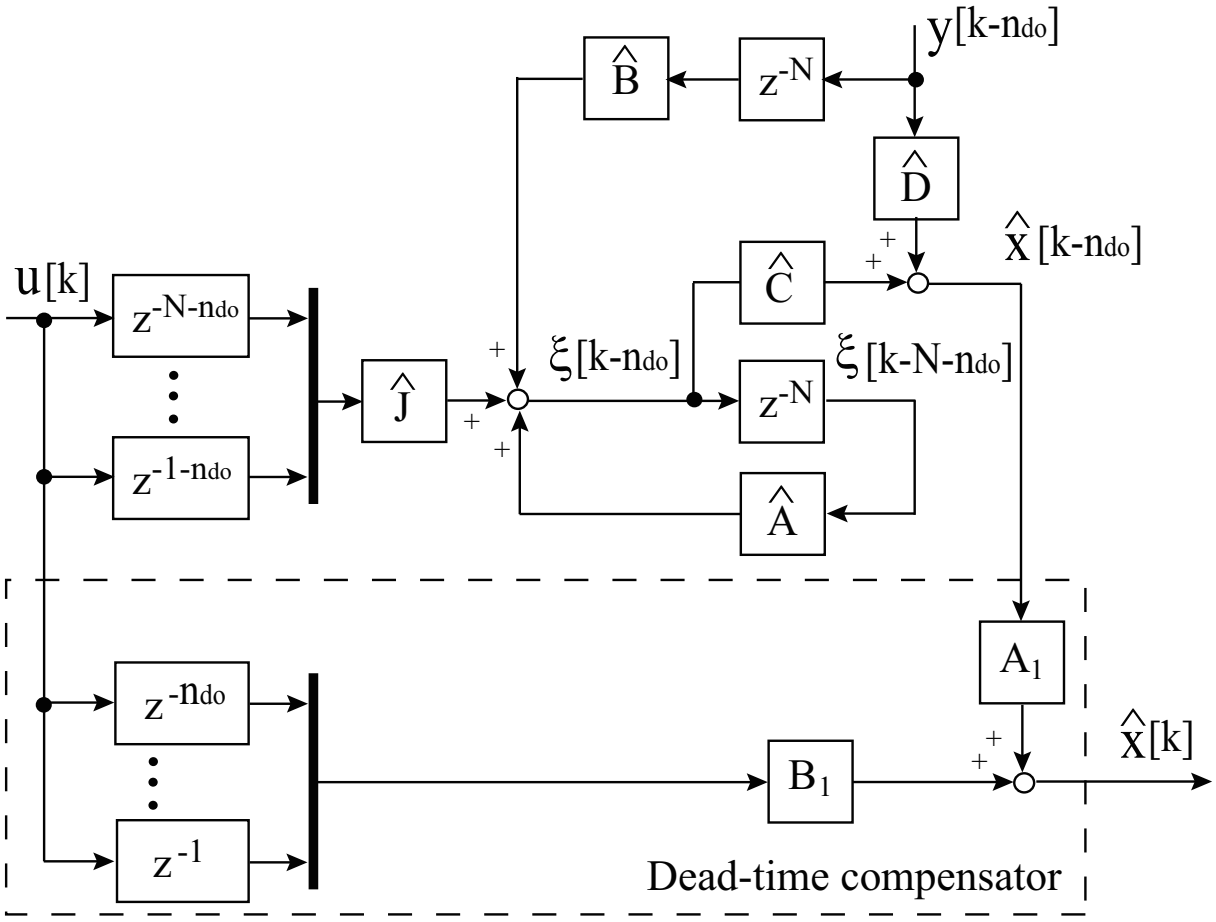

Figure 7.2: Long sampling short cycle observer with dead-time.

The continuous time state equation of the plant is determined as

$$\left[\begin{array}{c|c} \boldsymbol{A}_{cp} & \boldsymbol{b}_{cp} \\ \hline \boldsymbol{c}_{cp} & \boldsymbol{0} \end{array}\right] = \left[\begin{array}{cc|c} 0 & 1 & 0 \\ 0 & -\frac{B}{M} & \frac{1}{M} \\ \hline 1 & 0 & 0 \end{array}\right]. \tag{7.20}$$

The continuous time state equation of the step-type disturbance is determined as

$$\left[\begin{array}{c} \boldsymbol{A}_{cd} \\ \hline \boldsymbol{c}_{cd} \end{array}\right] = \left[\begin{array}{c} 0 \\ \hline 1 \end{array}\right]. \tag{7.21}$$

The control input $u(t)$ is the sinusoidal wave (amplitude: 0.025, frequency: 1 Hz). The disturbance $d(t)$ is step-type disturbance (amplitude: 0.05) applied at time 0 s.

7.5.2 Comparison of Moving Differents

The frequency response from y to v_{dif} by the moving difference in Fig. 7.4, where $N = 4$. The time response is also shown in Fig. 7.5. The difference per the long sampling NT_u is

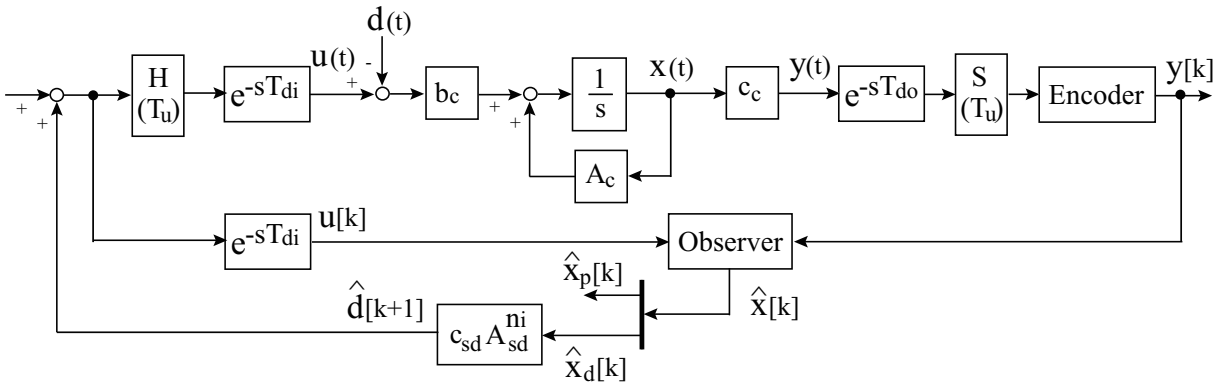

Figure 7.3: Block diagram of system.

Table 7.1: Specifications of plant.

Mass M	14.3 kg
Viscosity B	22.8 N/(m/s)
Thrust coefficient K_t	28.5 N/A
Sampling period T_u	1/2000 s
Input dead-time T_{di}	T_u
Output dead-time T_{do}	T_u
Resolution	0.1 μm

robust for the quantization error because its gain is lower than the difference per the short sampling T_u in the high frequency bandwidth. However, the difference per the long sampling NT_u also has bigger phase delay by $\frac{N}{2}$.

7.5.3 Comparison of Observers

The frequency response from y to $\hat{v}$ and $\hat{d}$ by the observer in Fig. 7.6, where $N = 4$. The frequency response of the singlerate full-order observer is equivalent to one of the singlerate minimum-order observer added 1-order LPF. The frequency response of LSSCO is also equivalent to one of the singlerate minimum-order observer discretized by the long sampling period NT_u.

The sensitivity function is shown in Fig. 7.7. Each observer was designed by pole-placement as the sensitivity function in the low frequency bandwidth is same.

The time response is shown in Fig. 7.8. The standard deviation 3σ of the time response is also shown in Table 7.2. LSSCO can reduce the quantization error best in these methods.

Moreover, it is verified that a noise of a particular frequency can be decoupled by utilizing

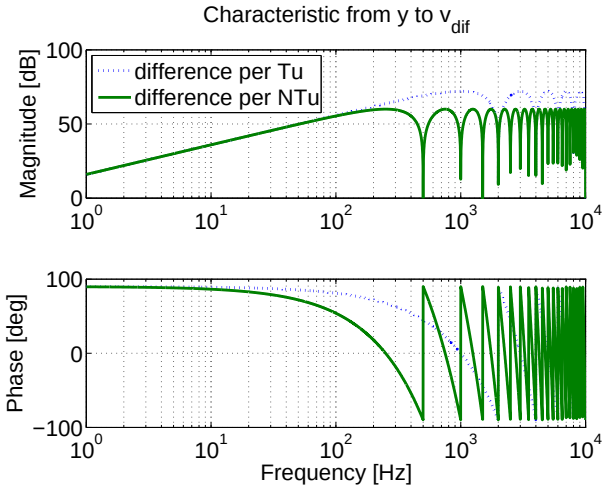

Figure 7.4: Frequency response of difference in $N = 4$.

Table 7.2: Standard deviation of velocity errors and disturbance errors in simulation.

	Velocity	Disturbance
Singlerate min-order	$10.5e^{-5}$ m/s	14.1 mN
Singlerate full-order	$9.62e^{-5}$ m/s	12.6 mN
LSSCO	$8.58e^{-5}$ m/s	11.0 mN

the folding characteristic of LSSCO in Fig. 7.6. In the case that sinusoidal noise (amplitude: 100 nm, frequency: 500 Hz) is applied, the time response is shown in Fig. 7.9. The minimum observer and the full order observer is influenced by the noise as Fig. 7.6 shows. On the other hand, LSSCO can decouple the noise of the particular frequency.

7.6 Experiments

The experimental stage has the linear encoder whose resolution is 1 nm/pulse for positioning in nano-scale. The velocity derived by the difference from the high resolution encoder is assured as the real velocity. Each method was compared after resolution is decreased until 0.1 μm by computing. This decreased resolution is same as Table 7.1.

In the experiment, very small velocity variation in servo-off is estimated. The velocity estimation by the moving difference is shown in Fig. 7.10, and the velocity estimation by the observer is shown in Fig. 7.11. The standard deviation 3σ of the time response is also shown in Table 7.2. LSSCO can reduce the quantization error best in these methods in the same way as the simulation.

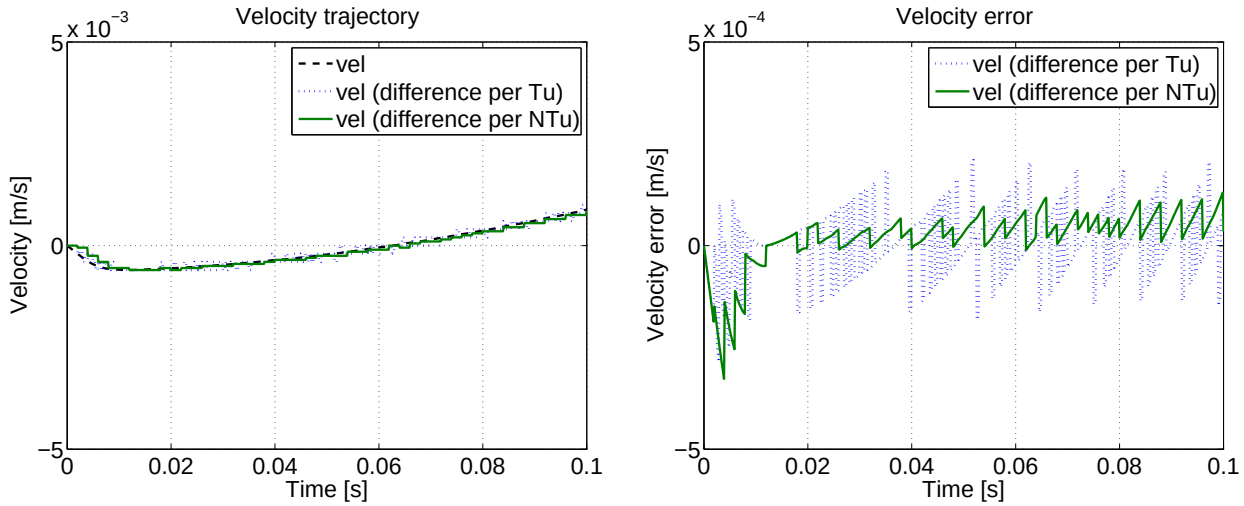

(a) Estimated velocity (b) Estimated velocity error

Figure 7.5: Time response by difference in $N = 4$.

Table 7.3: Standard deviation of velocity errors in experiment.

	Velocity
Singlerate min-order	$9.26e^{-5}$ m/s
Singlerate full-order	$11.03e^{-5}$ m/s
LSSCO	$8.07e^{-5}$ m/s

Moreover, in the case that sinusoidal noise (amplitude: 100 nm, frequency: 500 Hz) is applied, the time response is shown in Fig. 7.12. LSSCO can decouple the noise of the particular frequency in the same way as the simulation.

7.7 Summary

In the velocity derivation by the moving difference method, at least half sample delay is inevitable. The delay is longer if the difference sampling period is longer in order to reduce of the quantization error. On the other hand, the velocity derivation by the observer solves the sample delay problem though the plant model is needed. In this chapter, the observer which can estimate state variables with reducing the quantization error was proposed. The observer is based on multirate plant model by long sampling, and the states are estimated per the short cycle. Moreover, the proposed observer can also decouple the noise of the particular frequency. Finally, simulations and experiment with the experimental precision stage were performed to show the advantages of the proposed observer.

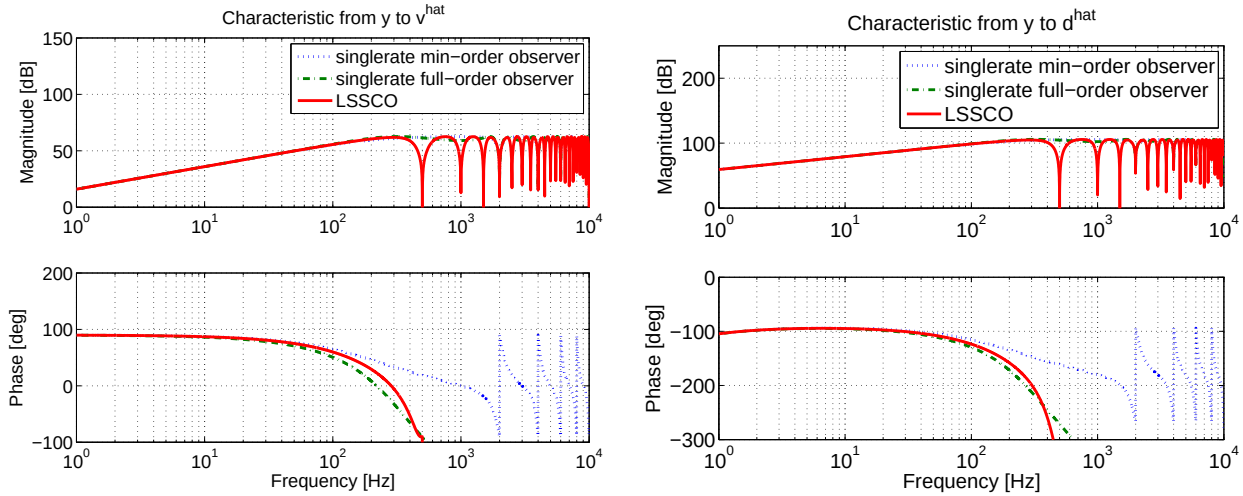

(a) y to $\hat{v}$ (b) y to $\hat{d}$

Figure 7.6: Frequency response of observer in $N = 4$.

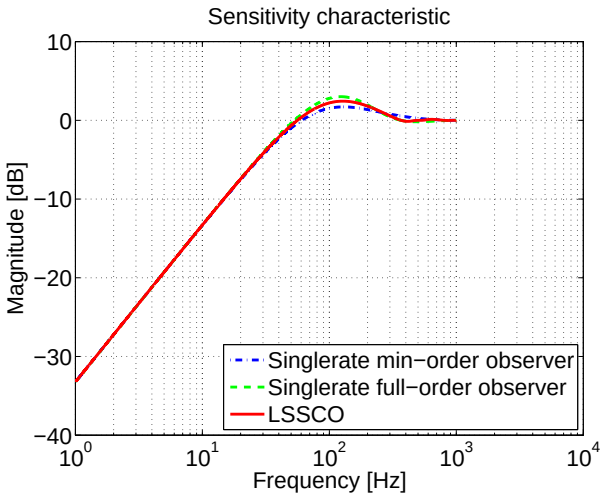

Figure 7.7: Sensitivity characteristic of observer in $N = 4$.

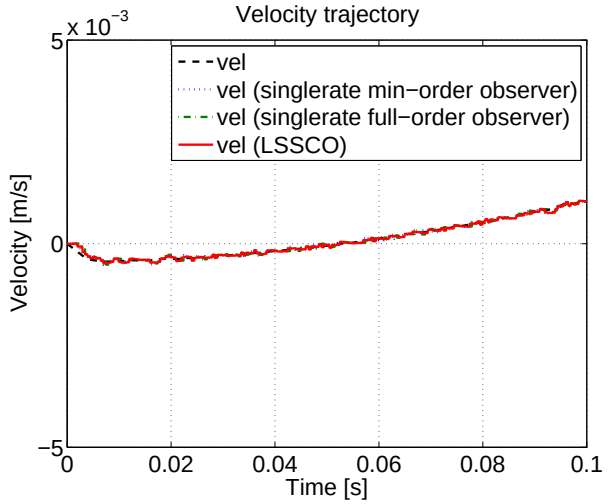

(a) Estimated velocity

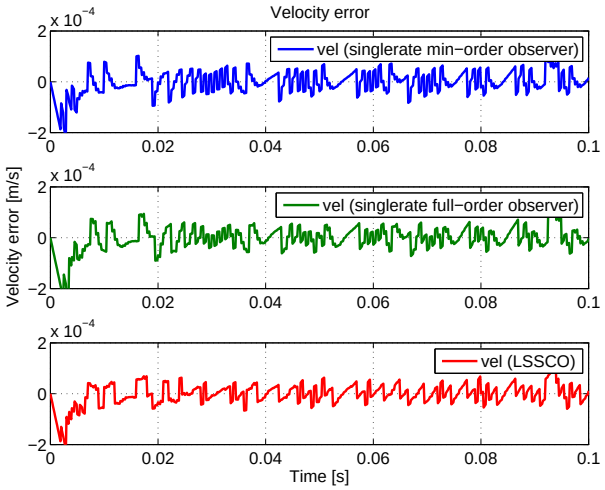

(b) Estimated velocity error

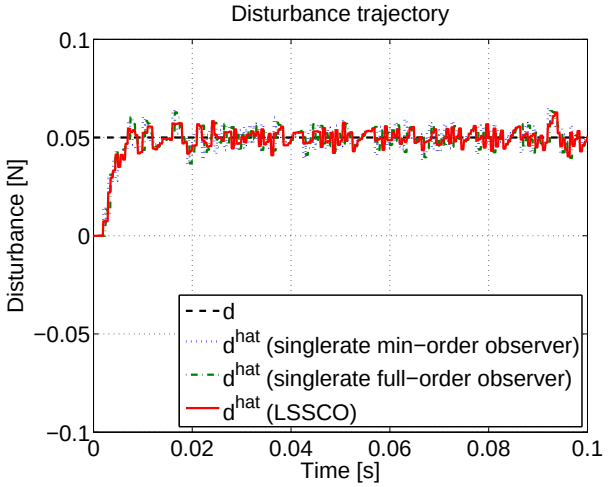

(c) Estimated disturbance

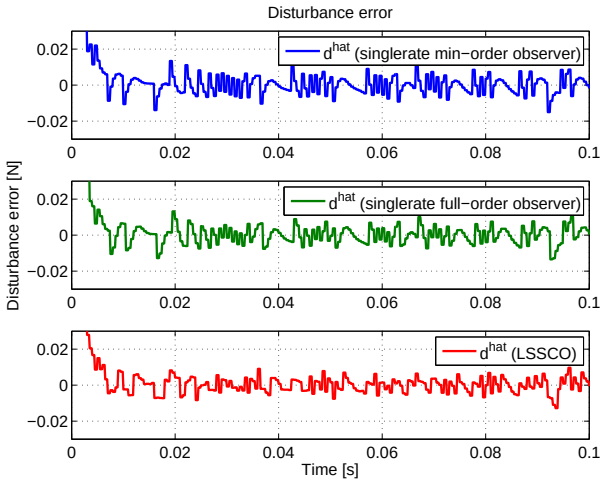

(d) Estimated disturbance error

Figure 7.8: Time response by observer in $N = 4$.

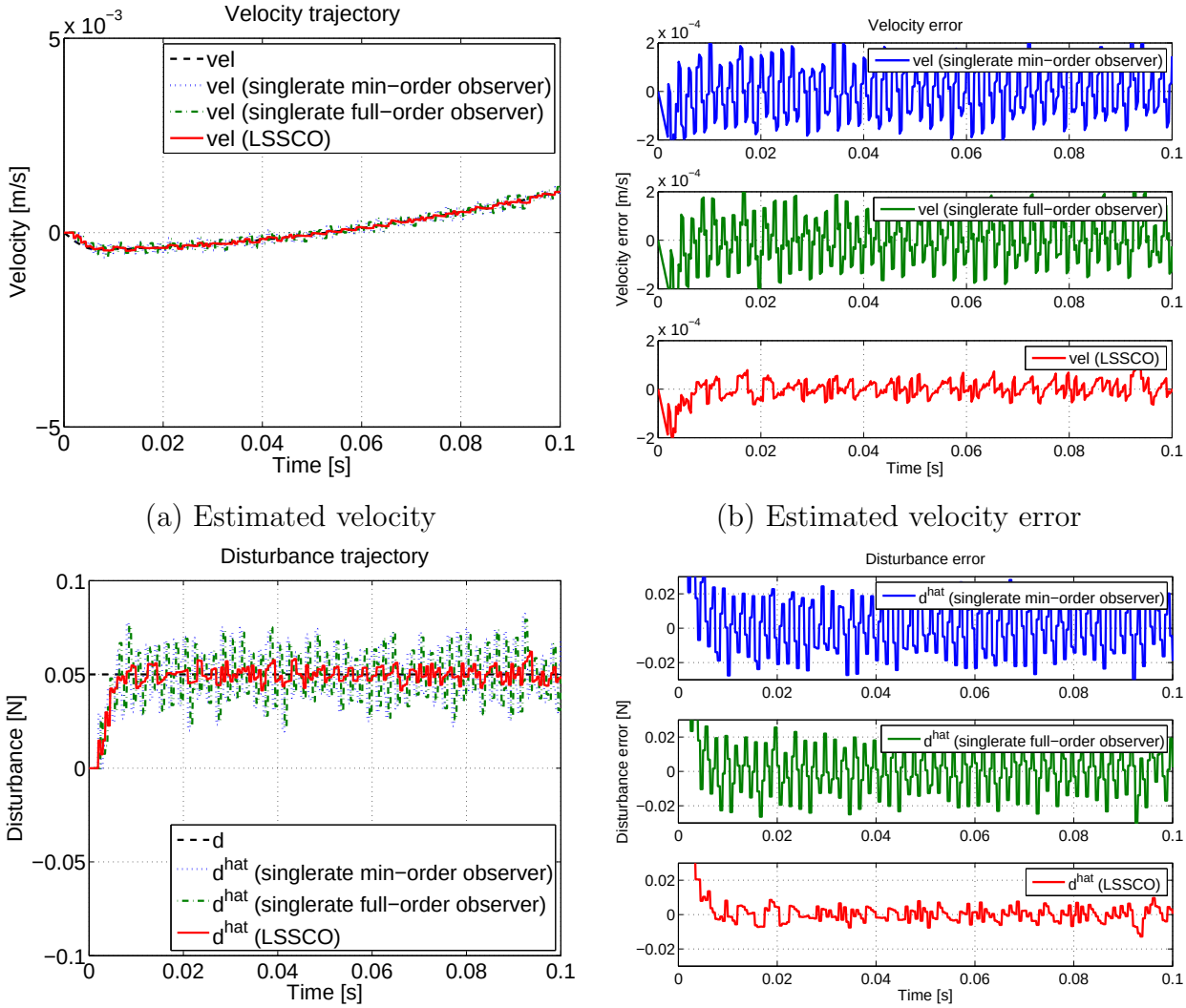

(a) Estimated velocity

(b) Estimated velocity error

(c) Estimated disturbance

(d) Estimated disturbance error

Figure 7.9: Time response by observer with sinusoidal noise in $N = 4$.

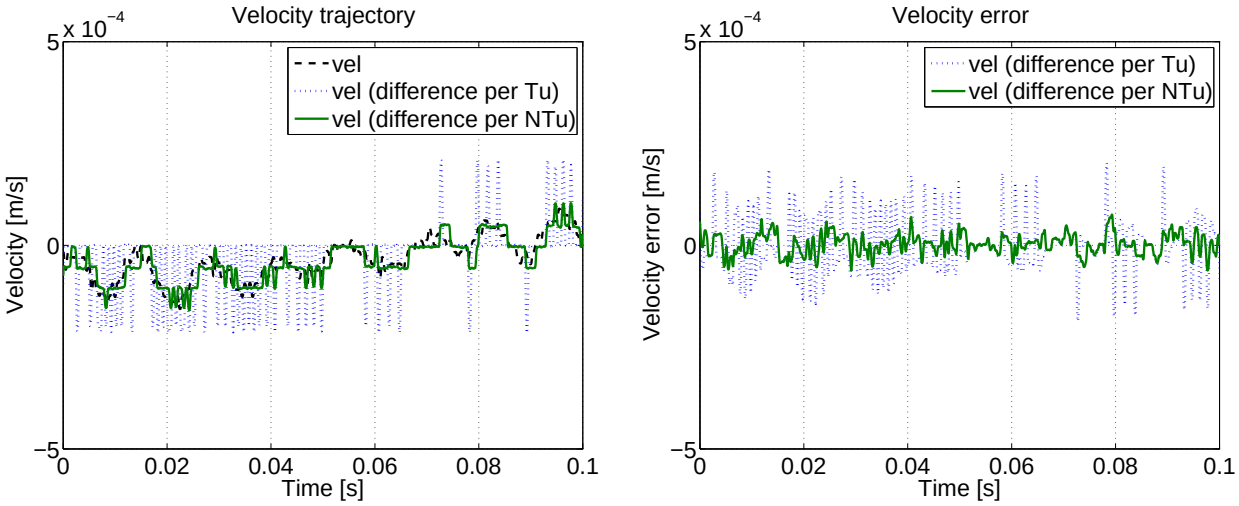

(a) Estimated velocity (b) Estimated velocity error

Figure 7.10: Experimental results by difference in $N = 4$.

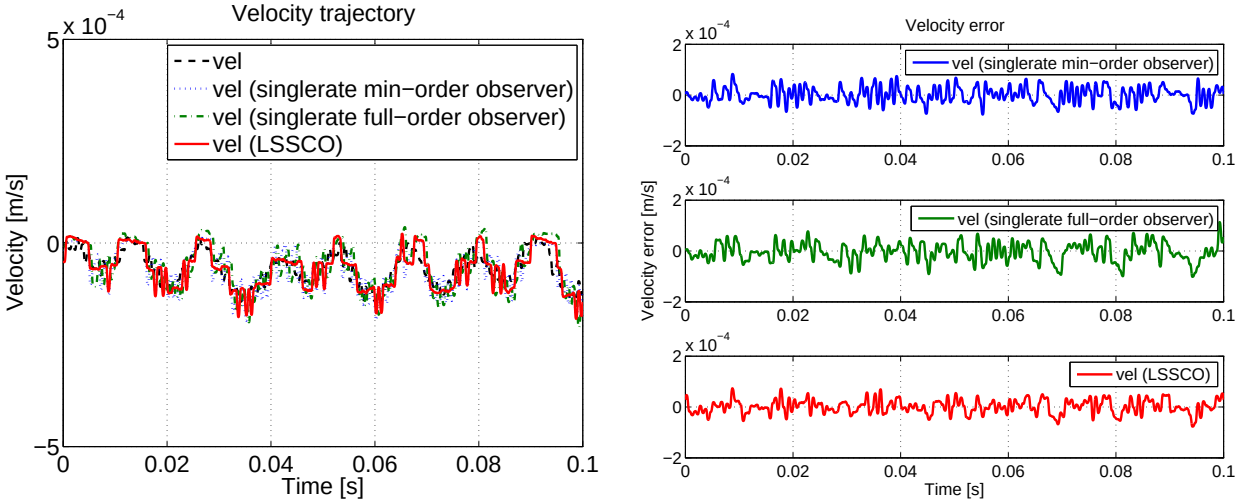

(a) Estimated velocity (b) Estimated velocity error

Figure 7.11: Experimental results by observer in $N = 4$.

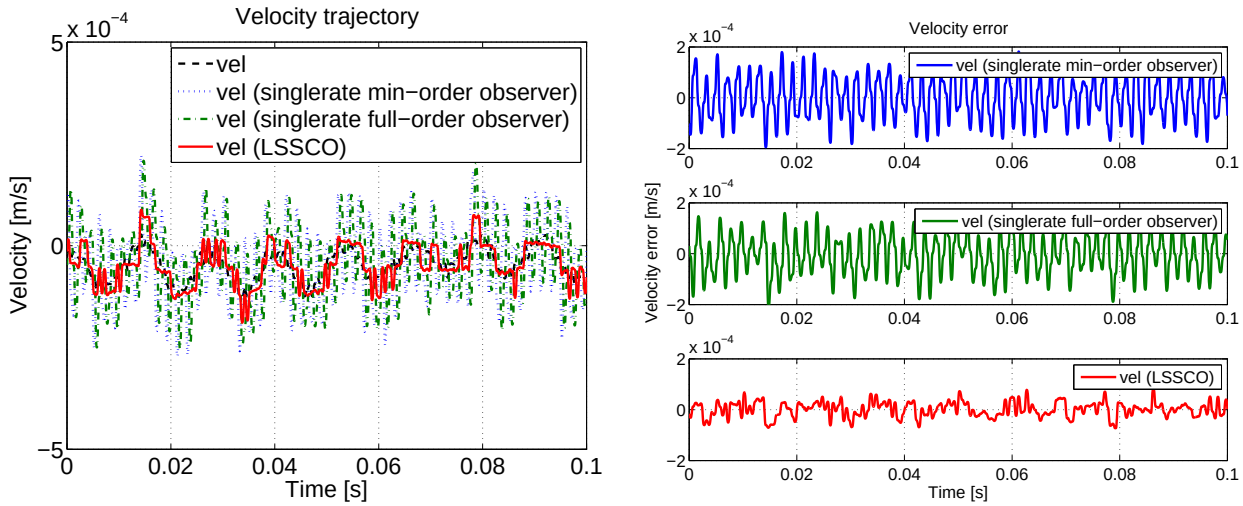

(a) Estimated velocity (b) Estimated velocity error

Figure 7.12: Experimental results by observer with sinusoidal noise in $N = 4$.

Chapter 8

Self Resonance Cancellation using Multiple Sensors

8.1 Abstract

The high-precision stage is industrial equipment for micro-fabrications and productions of semiconductors and LCD panels. The stage has the low resonance mode because of the structure of the stage and growing in the size. The resonance mode is a big trouble of fast and precise positioning. Simultaneous optimization of mechanism and control is a good approach for breakthrough of the control performance. However, in a large-scale gantry stage, it is difficult to change the structure incrementally because of the complexity of the stage. In this chapter, it is verified that high bandwidth design of the feedback control system is possible only by adding another sensor. Finally, simulations and experiments with the high-precision stage are performed to show the advantages of the proposed feedback control design.

8.2 Introduction

High-precision stages are used in industrial field such as manufacturing of semiconductors and liquid crystal panels (or displays). Fast and precise positioning control is very important technology related to the improvement of throughput and product quality.

XY gantry stage which has the table structure on the carriage in Fig. 2.5 is mainly applied to exposure systems and NC machine tools. However, a large-scale stage has a low resonance mode because of the low stiffness between the carriage and the table. The resonance mode is often located at about several ten Hz, and becomes an obstruction of fast and precise positioning in large-scale gantry stages.

In chapter 1, perfect tracking control (PTC) is applied to large-scale high-precision stage.

The severe specification of positioning of the large-scale high-precision stage is achieved by controlling the resonance mode actively.

However, it is difficult that the control design satisfies the specification which becomes severe every year for the given plant. Nowadays, simultaneous optimizations which design not only the controller but also the mechanics of the plant are researched well [51, 52]. The author's group also researches the simultaneous optimization for the high-precision stage. It was shown that it is possible for the plant to be in phase by changing mechanics of the stage [53] and to stabilize the phase by changing the driving point of the stage [54]. Although the breakthrough that large improvement of control performance is expected in the simultaneous optimization, it is difficult to change the structure incrementally because of the complexity of the large-scale gantry stage. The simultaneous optimization has to be considered from design stage of the mechanics of the product.

On the other hand, it is possible to increase detected state variables by adding another sensor. The control performance can be improved because degrees of freedom of design are increased. In previous researches, a piezoelectric element is applied to a galvano scanner [55]. In this chapter, another position sensor is applied to a high-precision stage in the case that it is difficult to change the structure additionally. It is shown that it is possible to design a novel feedback control which not only have high bandwidth but also is absolutely robust against the resonance mode parameters. Finally, simulations and experiments with the high-precision stage are performed to show the advantages of the proposed feedback control design. Here, adding sensors is often apt to be avoided because of sensor cost, but it is considered that sensors should be applied positively if high productivity brings in benefits more than the sensor cost.

8.3 Constitution of Stage and Modeling

8.3.1 High-Precision Stage

Fig. 8.1 shows the overview of the high-precision stage which has characteristic of x axis of the XY gantry stage shown in Fig. 2.5. Here, the high-precision stage is Nano-stage which is treated as the two-inertia mode. This stage consists of the carriage which move on the guide in the x direction and the table part on the carriage. The carriage is driven by the linear motor. the friction of the stage is almost zero because of using the air guide. The carriage and the table parts are connected by leaf springs. The resonance characteristic between the carriage and the table parts is equivalent to that of the large-scale gantry stage.

Moreover, the stage has two linear encoders to measure both the carriage part which is the drive and the table part which is the load. The resolution of the linear encoders is 1 nm/pulse respectively to achieve nanoscale positioning. In this chapter, the variable which

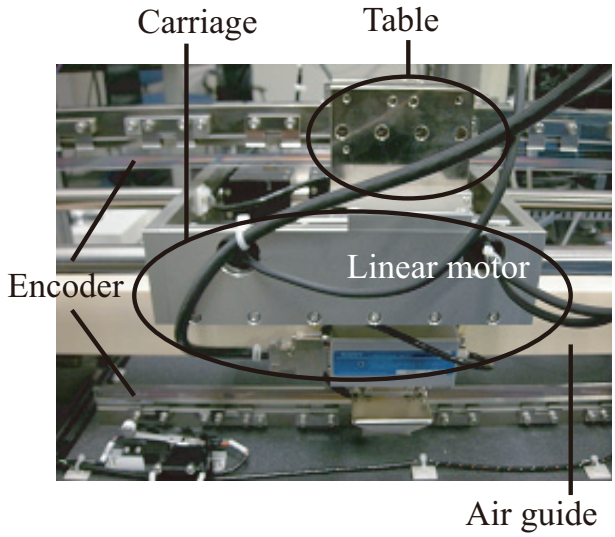

Figure 8.1: High-precision stage (same as Fig. 5.1).

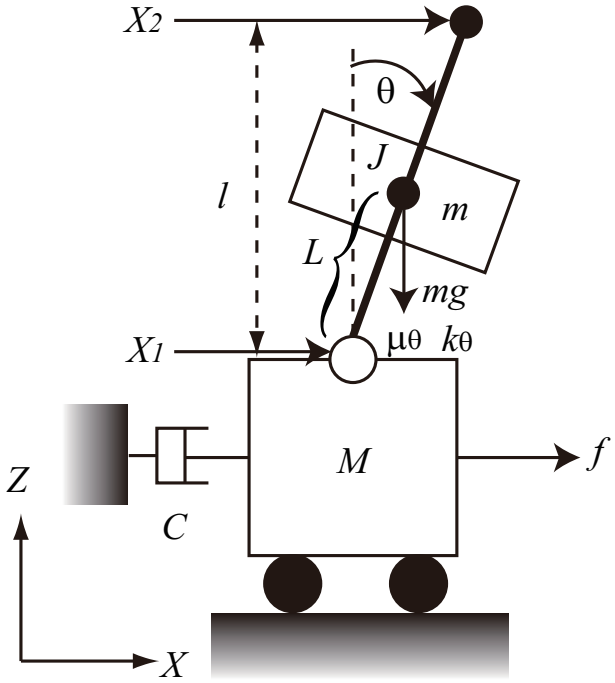

Figure 8.2: Stage model (same as Fig. 2.6).

should be controlled is the position of the table part.

8.3.2 Modeling

The high-precision stage can be assumed as 2-inertia system which consists of the carriage and the table. The stage model is shown in Fig. 8.2. Table 8.1 shows parameters of the stage. Here, variables X_1, X_2 and f represent the position of the carriage, the position of the table and the force, respectively. The transfer functions from the force f to each position are represented by

$$P_{X1}(s) = \frac{X_1}{f} = \frac{b_{12}s^2 + b_{11}s + b_{10}}{a_4 s^4 + a_3 s^3 + a_2 s^2 + a_1 s} \cdot e^{-sT_d}, \tag{8.1}$$

$$P_{X2}(s) = \frac{X_2}{f} = \frac{b_{22}s^2 + b_{21}s + b_{20}}{a_4 s^4 + a_3 s^3 + a_2 s^2 + a_1 s} \cdot e^{-sT_d}. \tag{8.2}$$

$$\begin{cases} a_4 = MmL^2 + MJ + mJ \\ a_3 = M\mu_\theta + m\mu_\theta + (mL^2 + J)C \\ a_2 = Mk_\theta + mk_\theta - MmgL - m^2gL + \mu_\theta C \\ a_1 = (k_\theta - mgL)C \\ b_{12} = mL^2 + J,\ b_{22} = mL^2 + J - mLl \\ b_{11} = b_{21} = \mu_\theta,\ b_{10} = b_{20} = k_\theta - mgL \end{cases}$$

Table 8.1: Stage parameters.

Carriage mass M	7.7	kg
Table mass m	5.3	kg
Inertia J	0.015	kg·m^2
Viscosity C	24	N/(m/s)
Spring constant k_θ	1700	N·m/rad
Decay constant μ_θ	0.20	N·m/(rad/s)
Length L	0.092	m
Length l	0.085	m
Dead-time T_d	6.0×10^{-4}	s

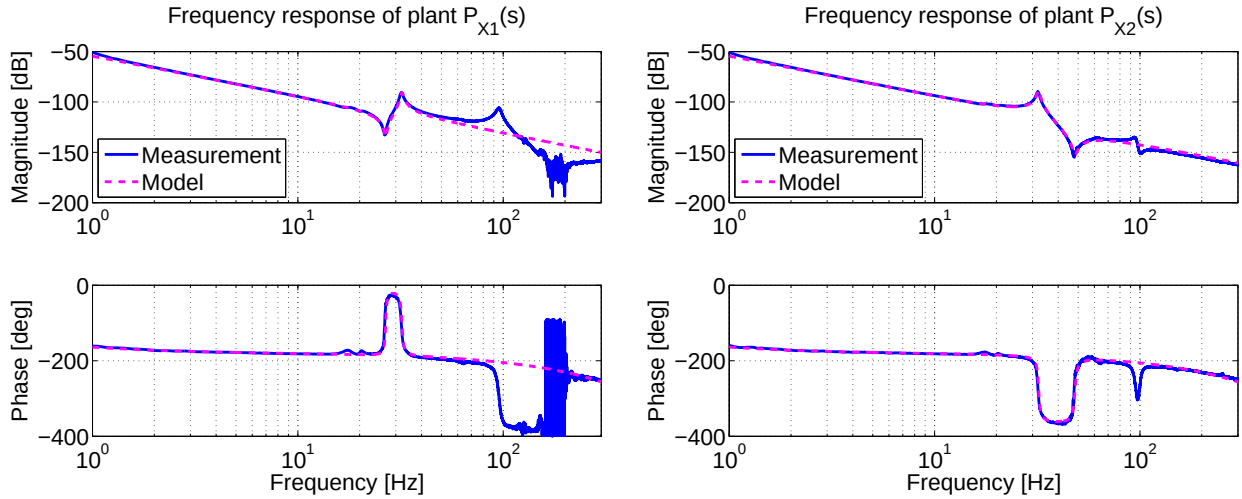

(a) $P_{X1}(s)$ (b) $P_{X2}(s)$

Figure 8.3: Frequency responses of plant.

The plant in single input single output (SISO) system is $P_{X2}(s)$ because the control input is the force f and the position of the table should be controlled. The frequency responses of the plant are shown in Fig. 8.3.

8.4 Design of Feedback Controller

8.4.1 Pole-placement Design for SISO System

Here, SISO system in which the control input is the force f and the position of the table X_2 is the output is considered. The PID controller:

$$C_{PID}(s) = K_P + \frac{K_I}{s} + \frac{K_D s}{\tau_D s + 1} \tag{8.3}$$

is designed for the rigid model of the plant:

$$P_{rigid}(s) = \frac{1}{(M+m)s^2 + Cs} \tag{8.4}$$

based on pole placement design. Next, the notch filter:

$$C_{notch}(s) = \frac{s^2 + d2\zeta\omega_N s + \omega_N^2}{s^2 + 2\zeta\omega_N s + \omega_N^2} \tag{8.5}$$

is designed for the primary resonance mode of the plant based on gain compensation. The feedback controller $C_{X2}(s)$ of SISO system is represented by

$$C_{X2}(s) = C_{PID}(s)C_{notch}(s), \tag{8.6}$$

as product of the PID controller and the notch filter.

8.4.2 Pole-placement Design for SIMO System

Here, single input multi output (SIMO) system, in which the control input is the force f and both the position of the table X_2 and the position of the carriage X_1 are the outputs, is considered.

The controller and the plant are defined as

$$\boldsymbol{C}(s) = [C_{X2}(s),\ C_{X1}(s)], \tag{8.7}$$

$$\boldsymbol{P}(s) = \begin{bmatrix} P_{X2}(s) \\ P_{X1}(s) \end{bmatrix}, \tag{8.8}$$

$$C_{X2}(s) = \frac{N_{c1}(s)}{D_c(s)},\ C_{X1}(s) = \frac{N_{c2}(s)}{D_c(s)}, \tag{8.9}$$

$$P_{X2}(s) \simeq \frac{N_{p1}(s)}{D_p(s)D_r(s)},\ P_{X1}(s) \simeq \frac{N_{p2}(s)}{D_p(s)D_r(s)}, \tag{8.10}$$

where,

$$\begin{cases} N_{p1}(s) = b_{22}s^2 + b_{21}s + b_{20} \\ N_{p2}(s) = b_{12}s^2 + b_{11}s + b_{10} \\ D_p(s) = s^2 + \frac{C}{M+m}s \\ D_r(s) = a_4s^2 + (a_3 - a_4\frac{C}{M+m})s + a_1\frac{M+m}{C} \end{cases}. \tag{8.11}$$

Here, the denominator of the plant cannot be separated into the rigid mode $D_p(s)$ and the resonance mode $D_r(s)$. The reason is that the motion of rotation direction is transformed into the motion of translation direction approximately in the 2 inertia model based on the pendulum. Therefore, it is tolerated the error occurs against dumping coefficient of 1st order in the resonance mode $D_r(s)$ as

$$a_4s^4 + a_3s^3 + a_2s^2 + a_1s = D_p(s)D_r(s) - \left(\frac{mLC}{M+m}\right)^2 s^2. \tag{8.12}$$

This approximation is appropriate because the value of $\left(\frac{mLC}{M+m}\right)^2$ is much smaller than that of the coefficient a_2.

By this separation, the characteristic equation $A_{cl}(s)$ of the closed loop is represented by

$$A_{cl} = D_c D_p D_r + N_{c1} N_{p1} + N_{c2} N_{p2}. \tag{8.13}$$

Here, if $N_{c1}(s)$ and $N_{c2}(s)$ can be designed as

$$N_{c1}(s) N_{p1}(s) + N_{c2}(s) N_{p2}(s) = D_r(s)\alpha(s), \tag{8.14}$$

the characteristic of the open loop is represented by

$$\begin{aligned} \boldsymbol{C}(s)\boldsymbol{P}(s) &= \frac{N_{c1}(s)N_{p1}(s) + N_{c2}(s)N_{p2}(s)}{D_c(s)D_p(s)D_r(s)} && (8.15) \\ &= \frac{\alpha(s)}{D_c(s)D_p(s)}, && (8.16) \end{aligned}$$

and then the pole-zero cancellation of the resonance mode occurs. In this case, the characteristic equation $A_{cl}(s)$ of the closed loop is represented by

$$A_{cl}(s) = (D_c(s)D_p(s) + \alpha(s))D_r(s). \tag{8.17}$$

$D_c(s)$ and $\alpha(s)$ can be designed in order to set the poles of the closed loop as

$$A_{cl}(s) = (s+\omega)^n D_r(s), \tag{8.18}$$

based on pole placement design.

Here, a design in which $N_{c1}(s)$ and $N_{c2}(s)$ do not contain $D_r(s)$ is considered. It is assumed that the following relational expression consists:

$$aN_{p1}(s) + bN_{p2}(s) = D_r(s), \tag{8.19}$$

where, a and b are constant. When the relational expression consists, $N_{c1}(s)$ and $N_{c2}(s)$ can be developed as

$$N_{c1}(s) = a\alpha(s), \quad N_{c2}(s) = b\alpha(s), \tag{8.20}$$

by (8.14).

Therefore, derivation of constant values a and b is considered. The coefficient comparison from (8.11) and (8.19) develops the relational expression for

$$\begin{cases} (a+b)(J+mL^2) - amLl = (M+m)J + MmL^2 \\ (a+b)\mu_\theta = (M+m)\mu_\theta + \frac{m^2L^2C}{M+m} \\ (a+b)(k_\theta - mgL) = (M+m)(k_\theta - mgL) \end{cases}. \tag{8.21}$$

Here, as long as term $\frac{m^2L^2C}{M+m}$ is ignored, constant values a and b can be developed as

$$\begin{cases} a = \frac{mL}{l} \\ b = M + m - a \end{cases}. \tag{8.22}$$

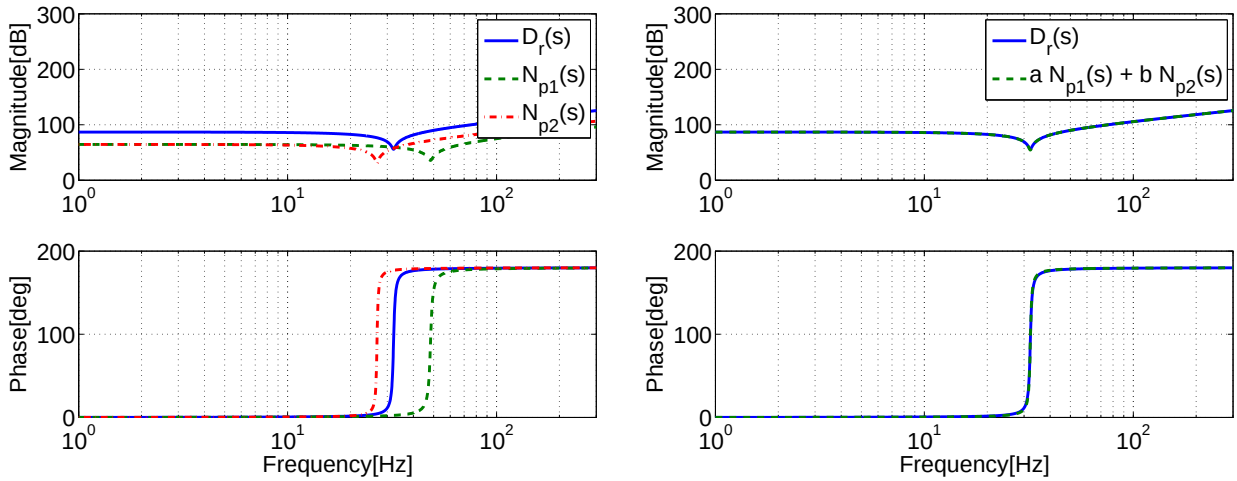

Figure 8.4: Frequency responses of resonance mode (Model).

Although this approximation allows that the dumping is slightly different, it hardly becomes a problem in a stage which has a small viscosity C (See Fig. 8.4).

Next, derivation of $D_c(s)$ and $\alpha(s)$ is considered. Here, the orders of $D_c(s)$ and $\alpha(s)$ have degrees of freedom of design. For example, PID type controller can be developed uniquely in the case of

$$\begin{cases} D_c(s) = s^2 + a_{c1}s \\ \alpha(s) = a_{\alpha 2}s^2 + a_{\alpha 1}s + a_{\alpha 0} \\ (D_c(s)D_p(s) + \alpha(s)) = (s+\omega)^4 \end{cases} . \tag{8.23}$$

In this case, $D_c(s)$ and $\alpha(s)$ are developed by the following expressions:

$$\begin{cases} a_{c1} = 4\omega - \frac{C}{M+m} \\ a_{\alpha 2} = 6\omega^2 - \frac{C}{M+m}a_{c1} \\ a_{\alpha 1} = 4\omega^3 \\ a_{\alpha 0} = \omega^4 \end{cases} . \tag{8.24}$$

As above, the feedback controller $\boldsymbol{C}(s)$ of SIMO system has been developed. This proposed control design is named "Self Resonance Cancellation".

In practical equipment, there is offset between the sensor position of X_1 and the sensor position of X_2. In the case that the offset can be a problem of the control performance, a high pass filter (HPF) is added in the controller $C_{X1}(s)$ in order to cut the low frequency components of X_1. The variable X_2 which should be controlled can track a target trajectory.

8.4.3 Robust Stability

In the case of SISO system, the notch filter compensates the gain of the primary resonance. Therefore, the robust stability becomes seriously impaired if the resonance mode is changed.

Table 8.2: Gain and phase margin.

	SISO		SIMO	
	G_m[dB]	P_m[deg]	G_m[dB]	P_m[deg]
Nominal	9.7	30.1	17.8	35.7
$k_{\theta n} = 0.5k_\theta$	Unstable	Unstable	17.8	35.7
$J_n = 5.0J$	Unstable	Unstable	17.8	35.7

On the other hand, in the case of SIMO system, constant values a and b are independent of parameters J, k_θ and μ_θ. Thus, (8.19) keeps on consisting even if these parameters are changed. Moreover, these parameters are independent on the pole placement design from (8.24). In other words, it is possible to design the absolutely robust feedback controller against these parameters which are important to determine the resonance mode.

8.5 Simulations

The feedback bandwidth of the SISO system was set to 5 Hz. The feedback bandwidth of the SIMO system was set to 20 Hz, and the cutoff frequency of the HPF was set to 1 Hz. Then, the control period was set to 200 μs, feedback controllers were discretized by Tustin transformation. The frequency responses of feedback controllers are shown in Fig. 8.5. It is shown that the feedback controller of the SISO system consists of the PID controller and the notch filter, and the feedback controller of the SIMO system consists of two PID controller for positions X_1 and X_2.

Simulations were performed in the three cases. First, the plant is nominal. Second, the spring constant of the nominal value $k_{\theta n}$ is different from that of real value k_θ by 0.5 times. Third, the inertia of the nominal value J_n is different from that of real value J by 5 times.

The frequency responses of the closed loop, the frequency responses of the open loop frequency and Nyquist diagrams are shown in Fig. 8.6, 8.7 and 8.8, respectively. Then, these gain and phase margins are shown in Table 8.2.

In the results, both the gain margin and the phase margin of the SIMO system are better than those of the SISO system even though the feedback bandwidth of the SIMO system is 4 times as high as that of the SISO system. Moreover, the robust stability becomes seriously impaired if the spring constant k_θ or the inertia J is changed in the SISO system. On the other hand, in the SIMO system, the control performance is not deteriorated at all even though the controllers are fixed.

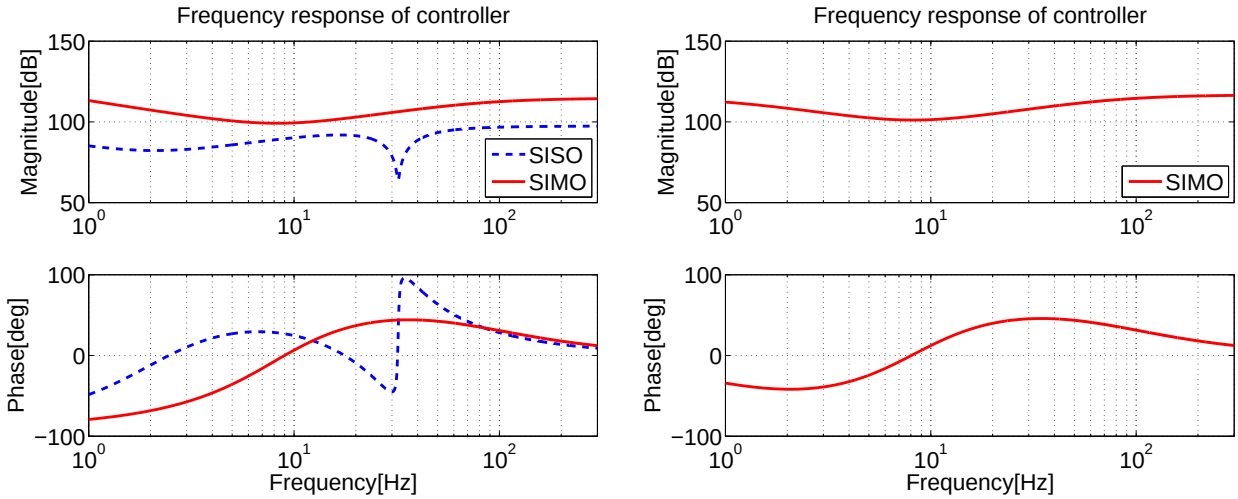

(a) Controller $C_{X2}[z]$ (b) Controller $C_{X1}[z]$

Figure 8.5: Frequency responses of controller.

8.6 Experiments

8.6.1 Frequency Responces

The frequency responses were measured with the high-precision stage in the three cases. First, the plant is nominal. Second, the spring constant of the nominal value $k_{\theta n}$ is different from that of real value k_θ by 0.5 times. Third, the inertia of the nominal value J_n is different from that of real value J by 5 times. In experiments, a stabilization filter was applied to the controller to cancel the secondary resonance mode of the plant because the real plant has not only the primary resonance mode but also the secondary resonance mode.

The frequency responses of the closed loop, the frequency responses of the open loop frequency and Nyquist diagrams are shown in Fig. 8.9, 8.10 and 8.11, respectively. From the measurements, in the SIMO system, the control performance is not deteriorated at all even though the spring constant k_θ or the inertia J is changed.

8.6.2 Tracking Performance

Finally, the tracking performance of the table position X_2 was evaluated with the high-precision stage. The target trajectories are shown in Fig. 8.12. The experimental results in the case of both feedback controller only and VSPTC + FB are shown in Fig. 8.13.

Both the gain margin and the phase margin of the SIMO system are better than those of the SISO system even though the feedback bandwidth of the SIMO system is 4 times as high as that of the SISO system. This is the reason why the tracking performance of the SIMO system is improved drastically.

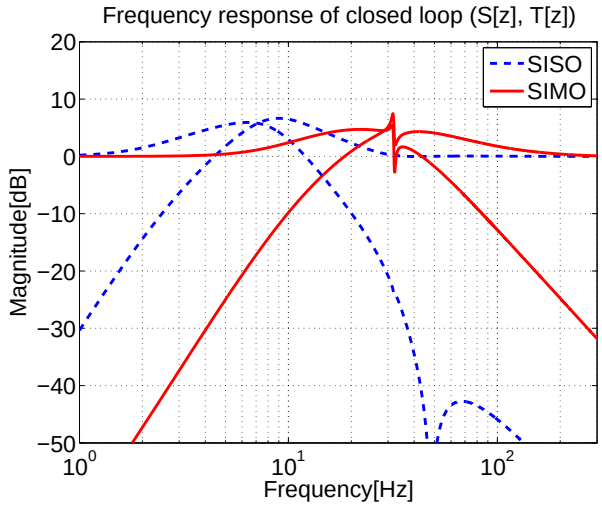

(a) Nominal

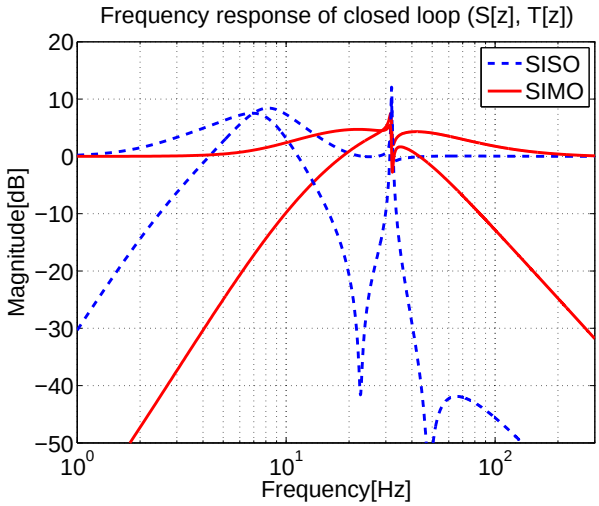

(b) $k_{\theta n} = 0.5k_\theta$

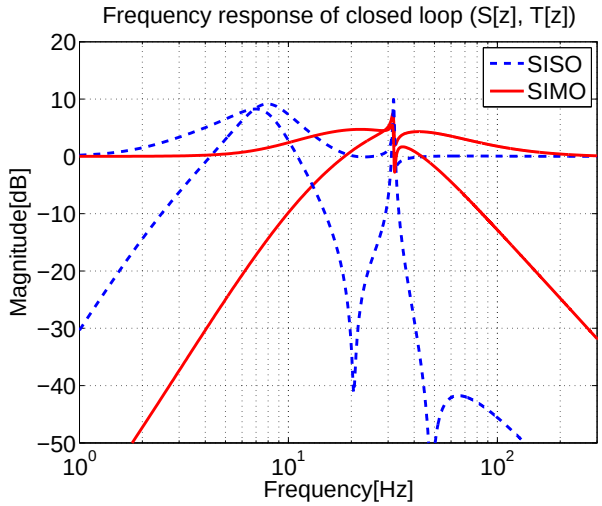

(c) $J_n = 5.0J$

Figure 8.6: Frequency responses of closed loop (Model).

8.7 Generalization to 2 Inertia System

Self resonance cancellation is generalized to the general 2 inertia system shown in Fig. 8.14.

8.7.1 Model of General 2 Inertia System

The block diagram of the general 2 inertia system is shown in Fig. 8.15. Table 8.3 shows parameters of the system. Here, variables θ_M, θ_L and T_M represent the position of the motor, the position of the load and the motor torque. The transfer functions from the torque T_M

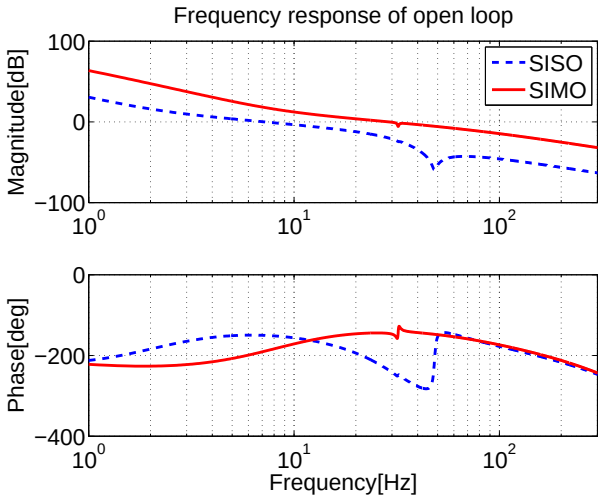

(a) Nominal

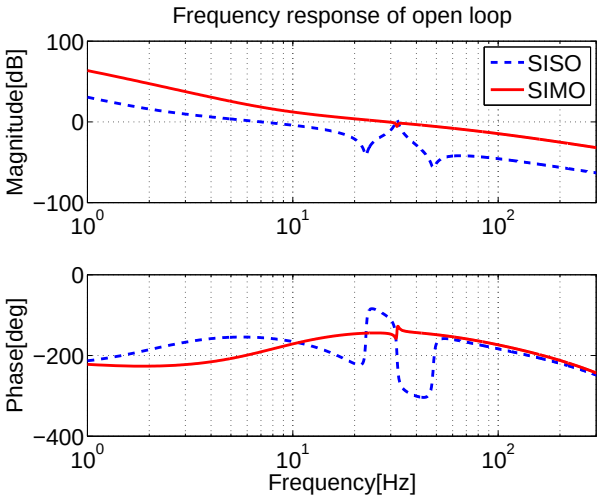

(b) $k_{\theta n} = 0.5k_\theta$

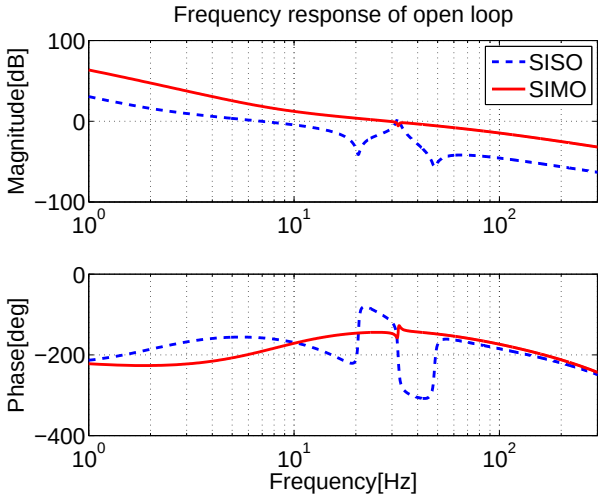

(c) $J_n = 5.0J$

Figure 8.7: Frequency responses of open loop (Model).

to each position are represented by

$$P_M(s) = \frac{\theta_M}{T_M} = \frac{1}{J_M s^2} \frac{s^2 + \frac{K}{J_L}}{s^2 + \frac{K}{J_L}(1 + \frac{J_L}{J_M})}, \tag{8.25}$$

$$P_L(s) = \frac{\theta_L}{T_M} = \frac{1}{J_M s^2} \frac{\frac{K}{J_L}}{s^2 + \frac{K}{J_L}(1 + \frac{J_L}{J_M})}. \tag{8.26}$$

The frequency responses of the plant are shown in Fig. 8.16.

8.7.2 Self Resonance Cancellation for General 2 Inertia Model

SIMO system in which the control input is the torque T_M and both the position of the load θ_L and the position of the motor θ_M are the outputs is considered.

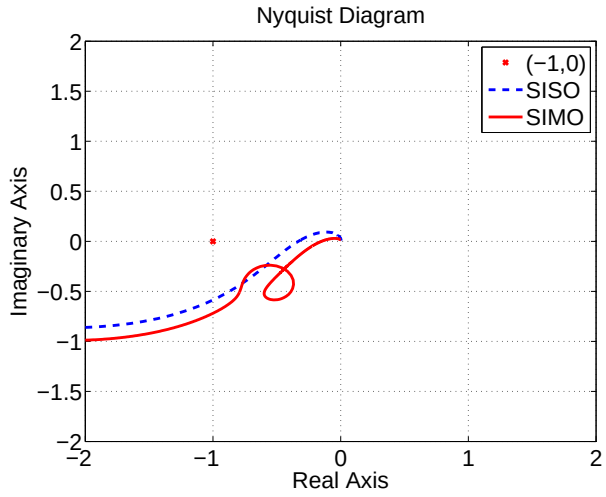

(a) Nominal

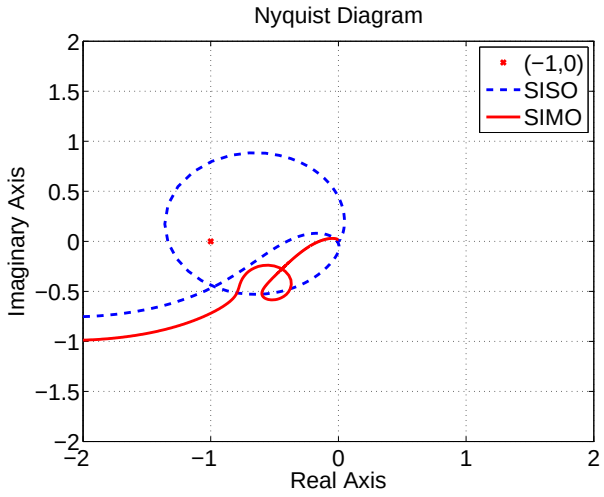

(b) $k_{\theta n} = 0.5k_\theta$

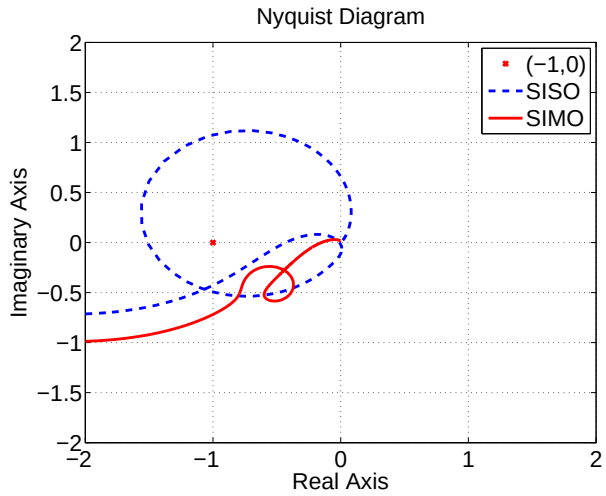

(c) $J_n = 5.0J$

Figure 8.8: Nyquist diagram (Model).

The controller and the plant are defined as

$$\boldsymbol{C}(s) = [C_L(s),\ C_M(s)], \tag{8.27}$$

$$\boldsymbol{P}(s) = \begin{bmatrix} P_L(s) \\ P_M(s) \end{bmatrix}, \tag{8.28}$$

$$C_L(s) = \frac{N_{CL}(s)}{D_C(s)},\ C_M(s) = \frac{N_{CM}(s)}{D_C(s)}, \tag{8.29}$$

$$P_L(s) = \frac{N_{PL}(s)}{D_P(s)D_R(s)},\ P_M(s) = \frac{N_{PM}(s)}{D_P(s)D_R(s)}, \tag{8.30}$$

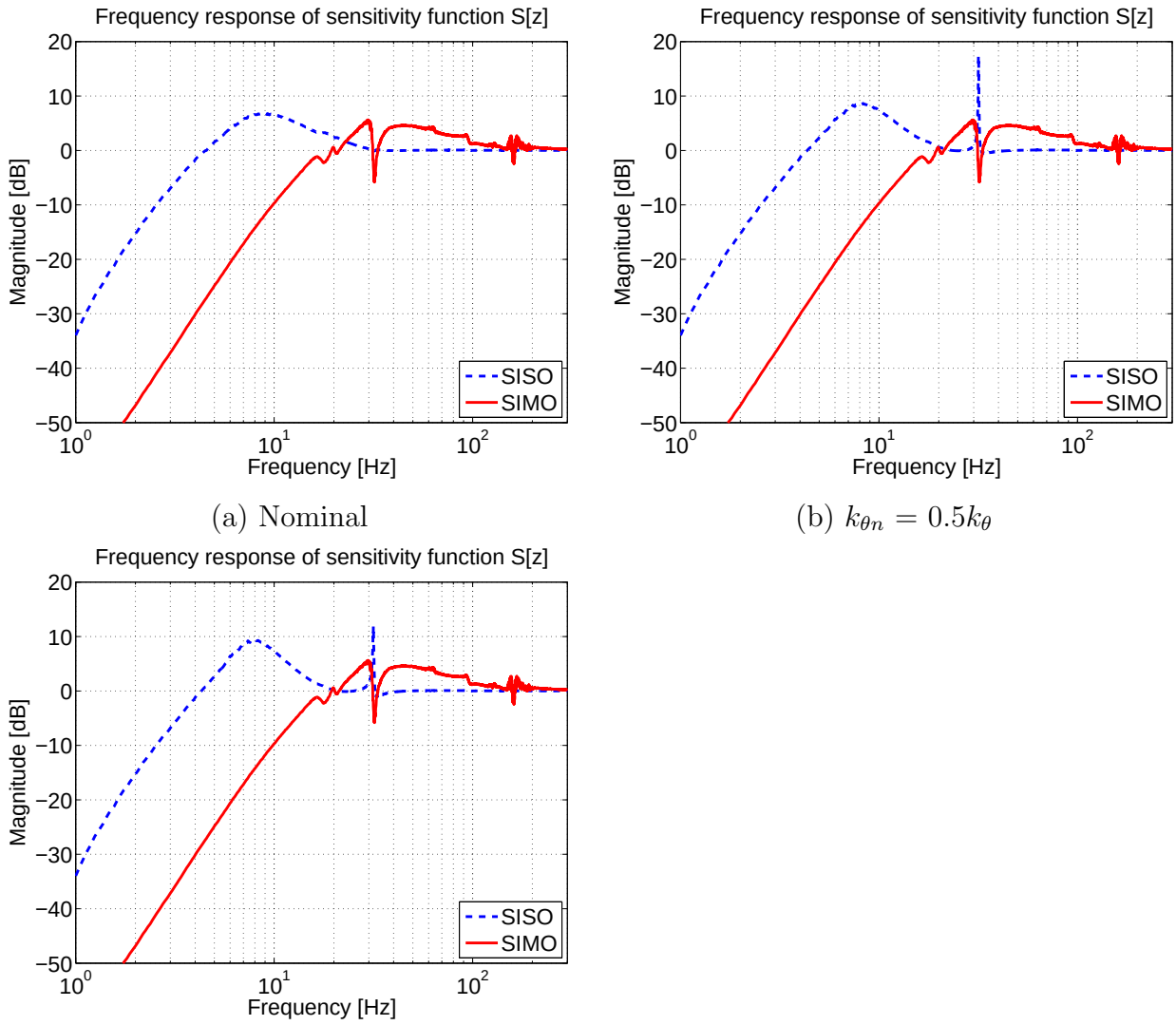

(a) Nominal

(b) $k_{\theta n} = 0.5k_\theta$

(c) $J_n = 5.0J$

Figure 8.9: Frequency responses of closed loop (Measurement).

where,

$$\begin{cases} N_{PL}(s) = \frac{K}{J_L} \\ N_{PM}(s) = s^2 + \frac{K}{J_L} \\ D_P(s) = J_M s^2 \\ D_R(s) = s^2 + \frac{K}{J_L}(1 + \frac{J_L}{J_M}) \end{cases} . \tag{8.31}$$

The characteristic equation $A_{cl}(s)$ of the closed loop is represented by

$$A_{cl} = D_C D_P D_R + N_{CL} N_{PL} + N_{CM} N_{PM}. \tag{8.32}$$

Here, if $N_{CL}(s)$ and $N_{CM}(s)$ can be designed as

$$N_{CL}(s)N_{PL}(s) + N_{CM}(s)N_{PM}(s) = D_R(s)\alpha(s), \tag{8.33}$$

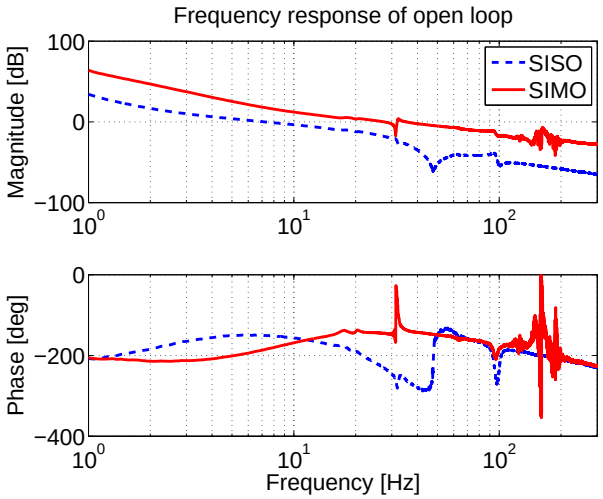

(a) Nominal

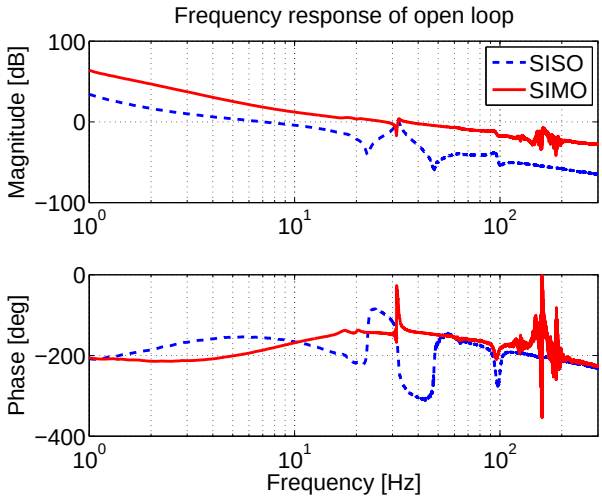

(b) $k_{\theta n} = 0.5k_\theta$

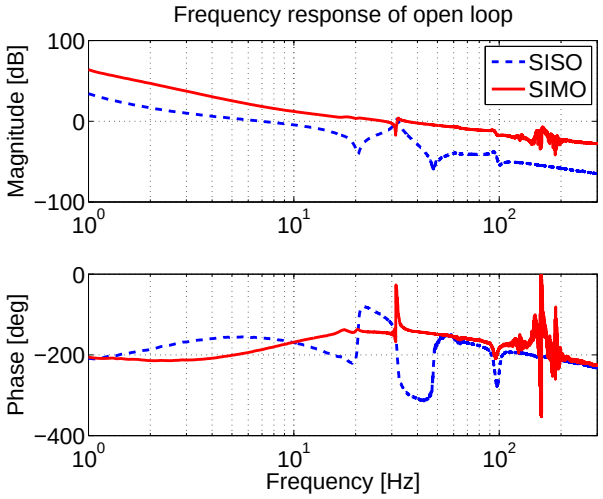

(c) $J_n = 5.0J$

Figure 8.10: Frequency responses of open loop (Measurement).

the characteristic of the open loop is represented by

$$\boldsymbol{C}(s)\boldsymbol{P}(s) = \frac{N_{CL}(s)N_{PL}(s) + N_{CM}(s)N_{PM}(s)}{D_C(s)D_P(s)D_R(s)} \tag{8.34}$$

$$= \frac{\alpha(s)}{D_C(s)D_P(s)}, \tag{8.35}$$

and then the pole-zero cancellation of the resonance mode occurs. In this case, the characteristic equation $A_{cl}(s)$ of the closed loop is represented by

$$A_{cl}(s) = (D_C(s)D_P(s) + \alpha(s))D_R(s). \tag{8.36}$$

$D_c(s)$ and $\alpha(s)$ can be designed in order to set the poles of the closed loop as

$$A_{cl}(s) = (s + \omega)^n D_R(s), \tag{8.37}$$

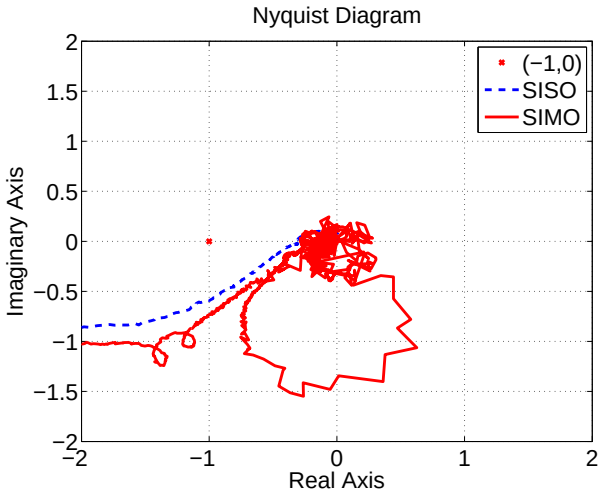

(a) Nominal

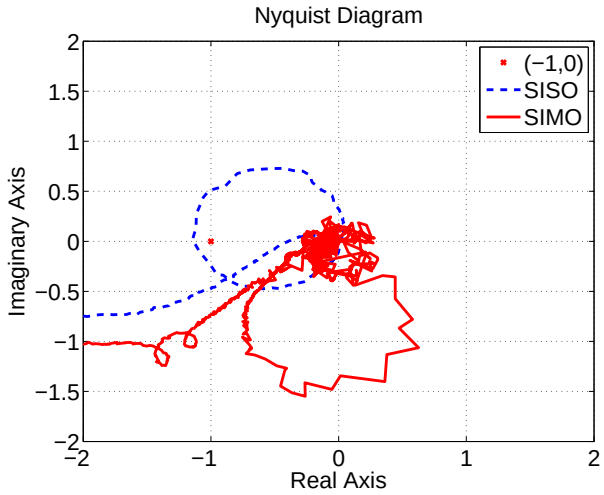

(b) $k_{\theta n} = 0.5k_{\theta}$

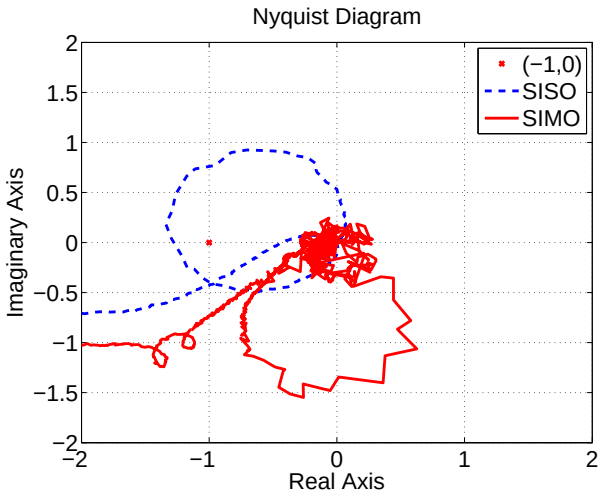

(c) $J_n = 5.0J$

Figure 8.11: Nyquist diagram (Measurement).

based on pole placement design.

Here, a design in which $N_{CL}(s)$ and $N_{CM}(s)$ do not contain $D_R(s)$ is considered. It is assumed that the following relational expression consists:

$$aN_{PL}(s) + bN_{PM}(s) = D_R(s), \tag{8.38}$$

where, a and b are constant. When the relational expression consists, $N_{CL}(s)$ and $N_{CM}(s)$ can be developed as

$$N_{CL}(s) = a\alpha(s), \quad N_{CM}(s) = b\alpha(s), \tag{8.39}$$

by (8.33).

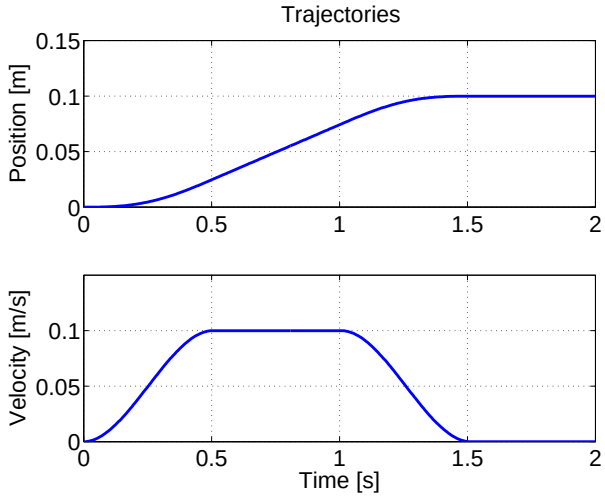

Figure 8.12: Target trajectories.

Table 8.3: parameters of 2 inertia system.

Motor Inertia J_M	0.02	kg·m^2
Load Inertia J_L	0.01	kg·m^2
Spring constant K	1000	N·m/rad

Therefore, derivation of constant values a and b is considered. The coefficient comparison from (8.31) and (8.38) develops the relational expression for

$$\begin{cases} a = \frac{J_L}{J_M} \\ b = 1 \end{cases} . \tag{8.40}$$

Next, derivation of $D_C(s)$ and $\alpha(s)$ is considered. Here, the orders of $D_C(s)$ and $\alpha(s)$ have degrees of freedom of design. For example, PID type controller can be developed uniquely in the case of

$$\begin{cases} D_C(s) = s^2 + a_{c1}s \\ \alpha(s) = a_{\alpha 2}s^2 + a_{\alpha 1}s + a_{\alpha 0} \\ (D_C(s)D_P(s) + \alpha(s)) = (s+\omega)^4 \end{cases} . \tag{8.41}$$

In this case, $D_C(s)$ and $\alpha(s)$ are developed by the following expressions:

$$\begin{cases} a_{c1} = 4\omega \\ a_{\alpha 2} = 6J_M\omega^2 \\ a_{\alpha 1} = 4J_M\omega^3 \\ a_{\alpha 0} = J_M\omega^4 \end{cases} . \tag{8.42}$$

As above, the feedback controller $\boldsymbol{C}(s)$ of SIMO system has been developed.

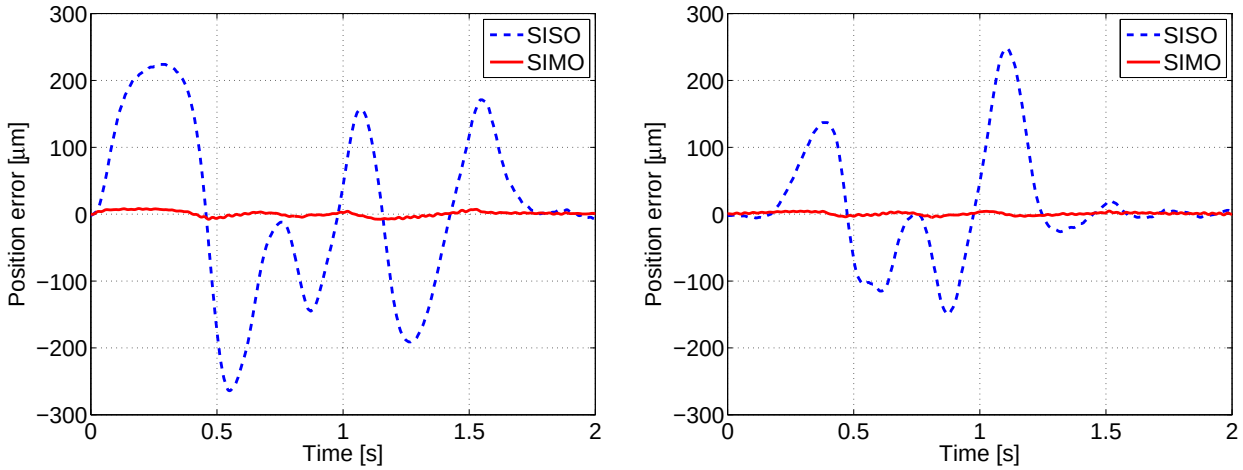

(a) FB only (b) VSPTC + FB

Figure 8.13: Tracking performance (Experiment).

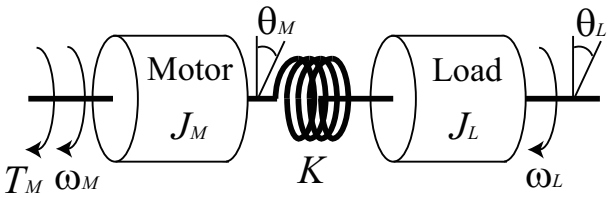

Figure 8.14: 2 inertia system.

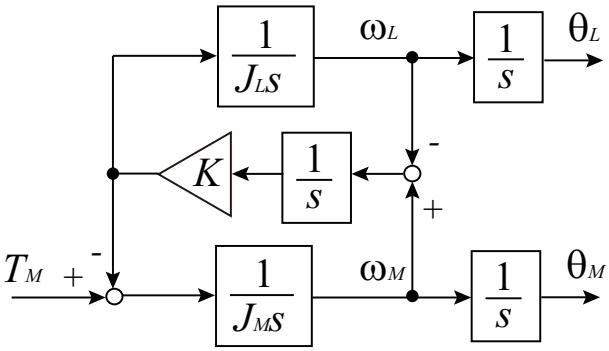

Figure 8.15: Block diagram of 2 inertia system.

8.7.3 Simulations of General 2 Inertia Model

The feedback bandwidth of the SISO system was set to 5 Hz. The feedback bandwidth of the SIMO system was set to 20 Hz, and the cutoff frequency of the HPF was set to 1 Hz. Then, the control period was set to 200 μs, feedback controllers were discretized by Tustin transformation. The frequency responses of feedback controllers are shown in Fig. 8.17.

The frequency responses of the closed loop, the frequency responses of the open loop frequency and Nyquist diagrams are shown in Fig. 8.18, 8.19 and 8.20, respectively. Then, these gain and phase margins are shown in Table 8.4.

In the results, both the gain margin and the phase margin of the SIMO system are better than those of the SISO system even though the feedback bandwidth of the SIMO system is 4 times as high as that of the SISO system.

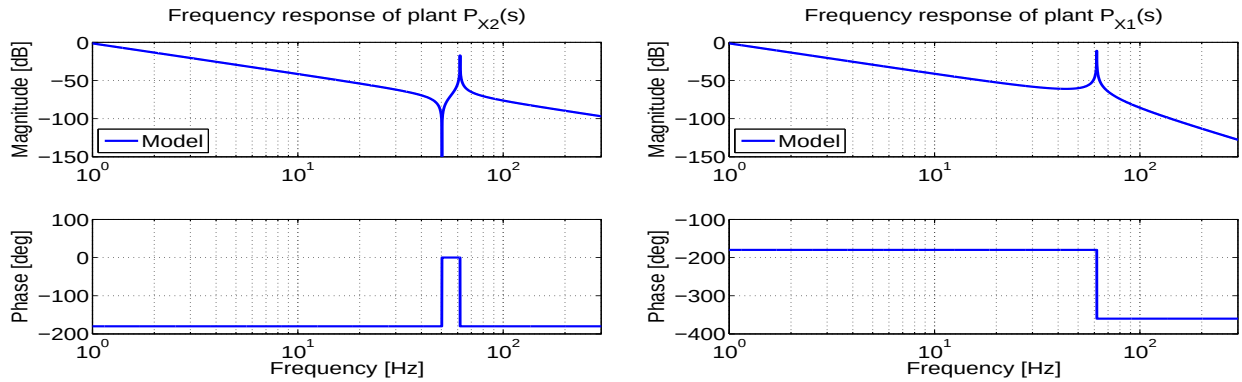

(a) $P_M(s)$ (b) $P_L(s)$

Figure 8.16: Frequency responses of plant.

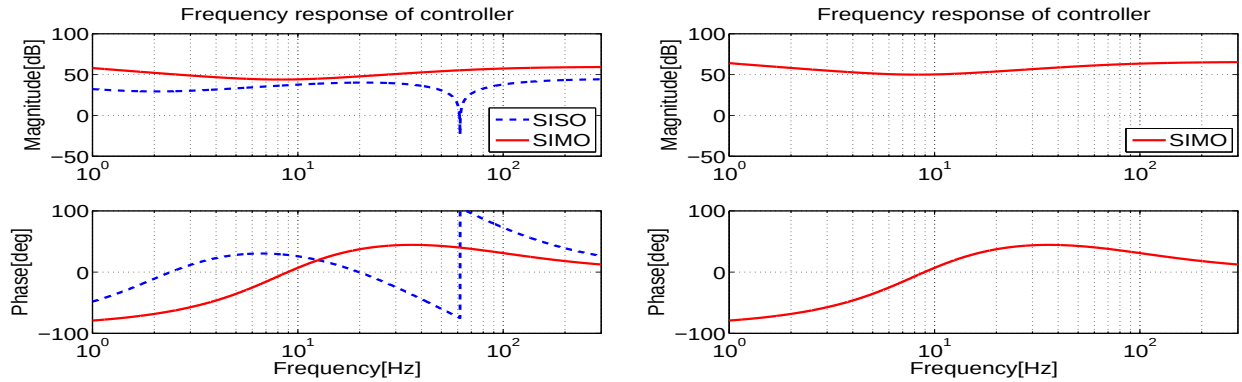

(a) Controller $C_L(s)$ (b) Controller $C_M(s)$

Figure 8.17: Frequency responses of controller.

8.8 Summary

The control system, in which not only the sensor of the table position but also the sensor of the carriage position was applied, was proposed in the positioning control of the gantry type high-precision stage. The proposed control design is named self resonance cancellation. It is shown that it is possible to achieve the high bandwidth and the absolute robustness against the resonance mode parameters by only two PID controllers. It was evaluated with the high-precision stage that the tracking performance of the proposed system was improved drastically. Finally, self resonance cancellation was generalized to the general 2 inertia system.

It is expected that the proposed method is applied to all 2 inertia systems in which the inertia variations are small. In future, the proposed method will be developed for multi-inertia systems.

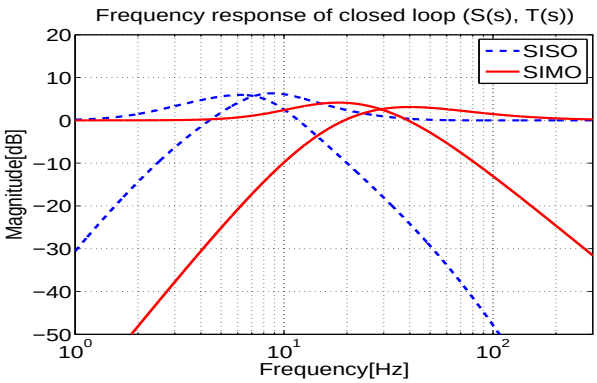

Figure 8.18: Frequency responses of closed loop (Model).

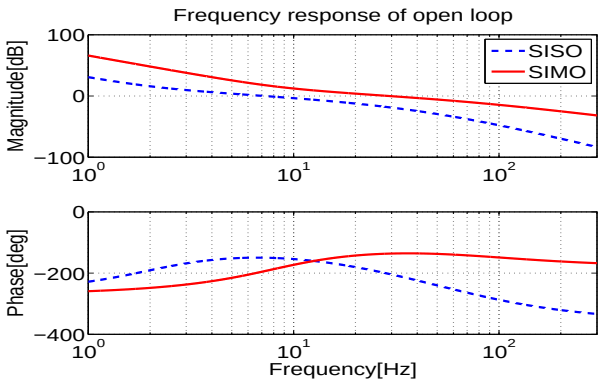

Figure 8.19: Frequency responses of open loop (Model).

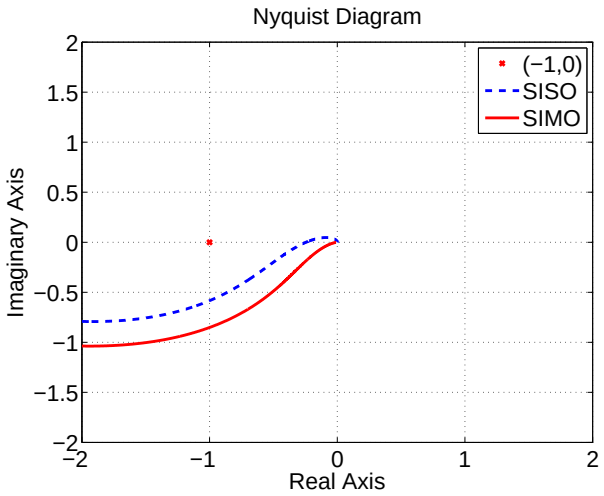

Figure 8.20: Nyquist diagram (Model).

Table 8.4: Gain and phase margin.

	SISO		SIMO	
	G_m[dB]	P_m[deg]	G_m[dB]	P_m[deg]
Nominal	12.2	30.2	Inf	43.5

Chapter 9

Design Fabrication of 4-DOF High-Precision Stage

9.1 Abstract

Motion control techniques are employed on nanoscale positioning in precision mechanical equipment, for example, NC machine tools, exposure systems, and so on. Then, the stages in actual industrial equipment often have several degrees of freedom. The degrees of freedom have to be controlled simultaneously. In this chapter, a new experimental 4-DOF high-precision stage is designed and fabricated. The 4-DOF stage can move to not only one translation but also the height, the pitching, and the rolling directions. Then, a control system for the 4-DOF stage is proposed. Finally, experiments are performed to show the advantages of the proposed method.

9.2 Introduction

Nowadays, motion control techniques are employed on nanoscale positioning in precision mechanical equipment, for example, NC machine tools, exposure systems, and so on. Especially, the high-precision motion control is required to achieve nanoscale positioning for stages of exposure systems.

Then, the stages in actual industrial equipment often have several degrees of freedom. The degrees of freedom have to be controlled simultaneously. Especially, the control of the attitude of the stages is very important as well as the translation direction in precision industrial equipment.

In this chapter, a new experimental 4-DOF high-precision stage which has a table structure is designed and fabricated. The 4-DOF stage can move to not only one translation but also the height, the pitching, and the rolling directions by the table structure. In section

9.3, the constitution and characteristics of the stage are shown. In section 9.4, a control system for the 4-DOF stage is proposed. The target of the control system is to maintain the attitude of the table flatly in driving the translation direction as well as fast and precise position control in the translation direction. The control system is based on perfect tracking control (PTC) [20] and a decoupling control for a coupling term between the translation and the pitching. In section 9.5, experiments are performed to show the advantages of the proposed system.

9.3 Nano-stage Ⅱ

A new experimental high-precision stage is designed and fabricated to control 4-DOF directions. The experimental stage is called "Nano-stage Ⅱ" below.

9.3.1 Constitution of Nano-stage Ⅱ

Fig. 9.1 shows the overview of Nano-stage Ⅱ. The stage is driven by twin linear motors in the translation x direction. The friction is almost zero because of using the air guide in x axis. Moreover, Nano-stage Ⅱ has the table part which has 3-DOF. The table part can move to the height z, the pitching θ_y, and the rolling θ_x directions by four voice coil motors (VCMs). Fig. 9.2 shows the structure of the table part. The four VCMs are under the four corners of the table. The gravity canceller is under the center of the table. The gravity canceller cancels only gravity of the table part with air press.

Nano-stage Ⅱ has two linear encoders both sides of the table part in Fig. 9.1. The sensor header mounts of the two linear encoders are shown in Fig. 9.2. Calculating the center position of the table with the two linear encoders, the position is assumed as the real position of the stage. Then, four linear encoders for the VCMs are on the inside of the VCMs under the four corners of the table. The four linear encoders can measure the positions of the VCMs in a local coordinate based on the stage. The sensor header mounts of the four linear encoders are shown in Fig. 9.2. Thus, Nano-stage Ⅱ has six linear encoders totally. The resolutions of all linear encoders are 1 nm/pulse.

Moreover, the table sensors are over the table in Fig. 9.1. These sensors can measure the positions at the points of table in the global coordinate. In this chapter, these positions are evaluated in the local coordinate.

9.3.2 Characteristics of Nano-stage Ⅱ

The plant model of the translation x is

$$P_x(s) = \frac{x}{u_x} = \frac{b_{x0}}{s^2 + a_{x1}s}. \tag{9.1}$$

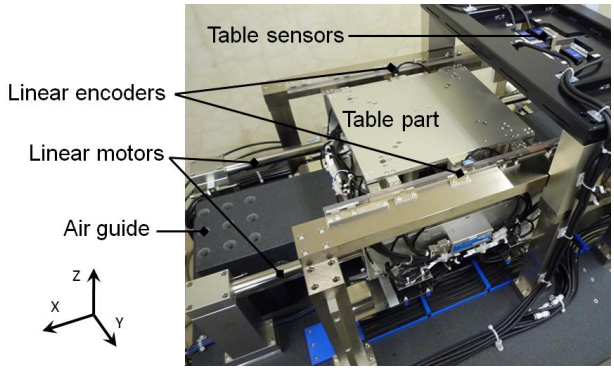

Figure 9.1: Overview of Nano-stage Ⅱ.

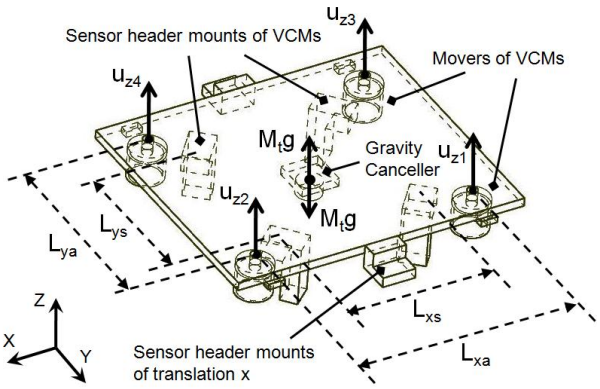

Figure 9.2: Structure of table part.

The input u_x is the current reference of the linear motors. Here, a PI current controller is designed for the current loop to be first-order system whose band frequency is 500 Hz. The current loop is not included in this model.

The other models of the table are gotten by transform matrices. The inputs u_{z1}, u_{z2}, u_{z3} and u_{z4} of VCMs in Fig. 9.2 are transformed into the inputs u_z, $u_{\theta x}$ and $u_{\theta y}$ by

$$\begin{bmatrix} u_{z1} \\ u_{z2} \\ u_{z3} \\ u_{z4} \end{bmatrix} = \begin{bmatrix} \frac{1}{4} & \frac{1}{2L_{ya}} & \frac{1}{2L_{xa}} \\ \frac{1}{4} & \frac{1}{2L_{ya}} & -\frac{1}{2L_{xa}} \\ \frac{1}{4} & -\frac{1}{2L_{ya}} & \frac{1}{2L_{xa}} \\ \frac{1}{4} & -\frac{1}{2L_{ya}} & -\frac{1}{2L_{xa}} \end{bmatrix} \begin{bmatrix} u_z \\ u_{\theta x} \\ u_{\theta y} \end{bmatrix}. \tag{9.2}$$

The positions z_1, z_2, z_3 and z_4 of linear encoders for VCMs are transformed into the positions z, θ_x and θ_y by

$$\begin{bmatrix} z \\ \theta_x \\ \theta_y \end{bmatrix} = \begin{bmatrix} \frac{1}{4} & \frac{1}{4} & \frac{1}{4} & \frac{1}{4} \\ \frac{1}{2L_{ys}} & \frac{1}{2L_{ys}} & -\frac{1}{2L_{ys}} & -\frac{1}{2L_{ys}} \\ \frac{1}{2L_{xs}} & -\frac{1}{2L_{xs}} & \frac{1}{2L_{xs}} & -\frac{1}{2L_{xs}} \end{bmatrix} \begin{bmatrix} z_1 \\ z_2 \\ z_3 \\ z_4 \end{bmatrix}. \tag{9.3}$$

The plant models of the height y, the rolling θ_x and the pitching θ_y are

$$P_z(s) = \frac{z}{u_z} = \frac{b_{z0}}{s^2 + a_{z1}s + a_{z0}}, \tag{9.4}$$

$$P_{\theta x}(s) = \frac{\theta_x}{u_{\theta x}} = \frac{b_{\theta x0}}{s^2 + a_{\theta x1}s + a_{\theta x0}}, \tag{9.5}$$

$$P_{\theta y}(s) = \frac{\theta_y}{u_{\theta y}} = \frac{b_{\theta y0}}{s^2 + a_{\theta y1}s + a_{\theta y0}}. \tag{9.6}$$

Fig. 9.3 shows the frequency responses of all plants in measurements and models.

Then, the structure of the table part was analysed by both FEM analyses and experimental modal analyses. The modal patterns of both FEM analyses and experimental modal

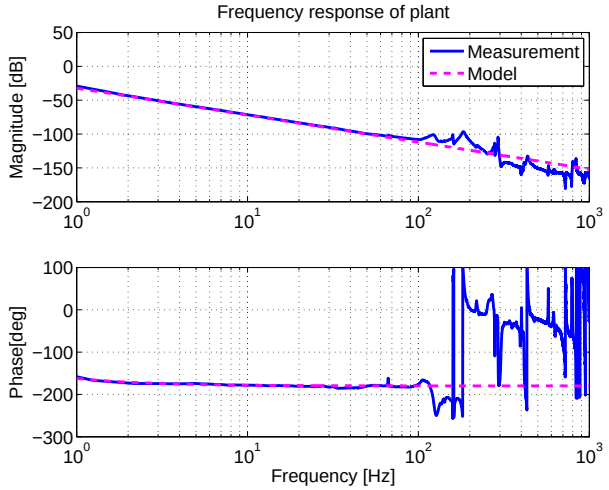

(a) Translation x

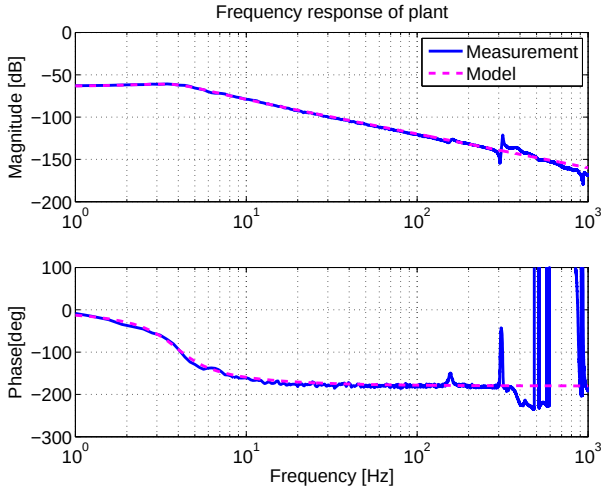

(b) Height z

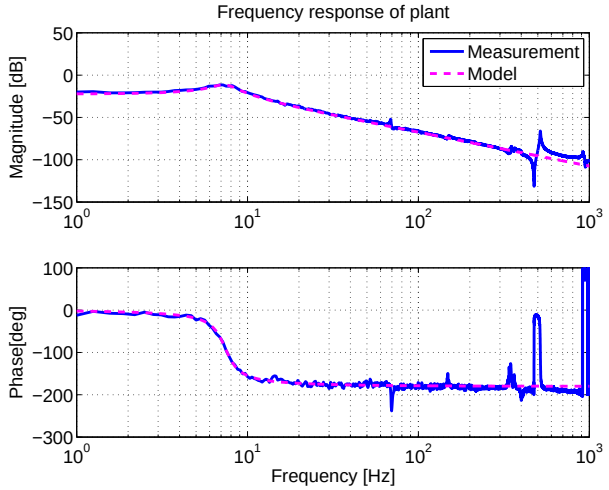

(c) Rolling θ_x

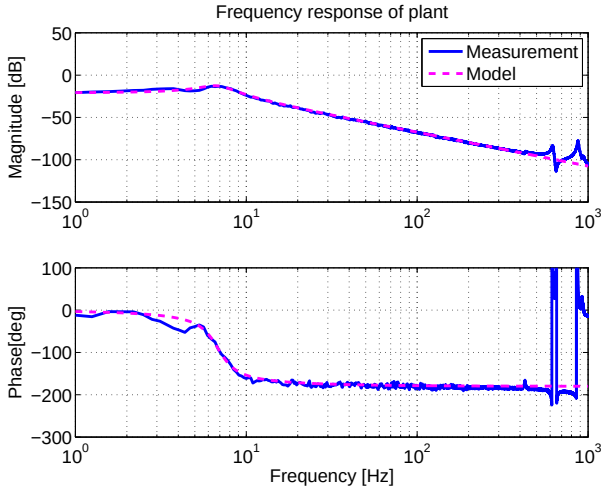

(d) Pitching θ_y

Figure 9.3: Frequency responses of plants.

analyses almost coincided. Fig. 9.4 shows the modal patterns. Here, note that the sensors of VCMs are under the four corners of the table in Fig. 9.2. For example, in modal pattern of Fig. 9.4 (a), the four corners of the table are vibrating at 314 Hz in the same direction z. Therefore, sensor position z including the vibration at 314 Hz is measured. In the frequency response of the height z of Fig. 9.3 (b), the resonanse mode at 314 Hz can be recognized. In the same way, the others modes in Fig. 9.4 can be recognized in the frequency responses in Fig. 9.3 respectively.

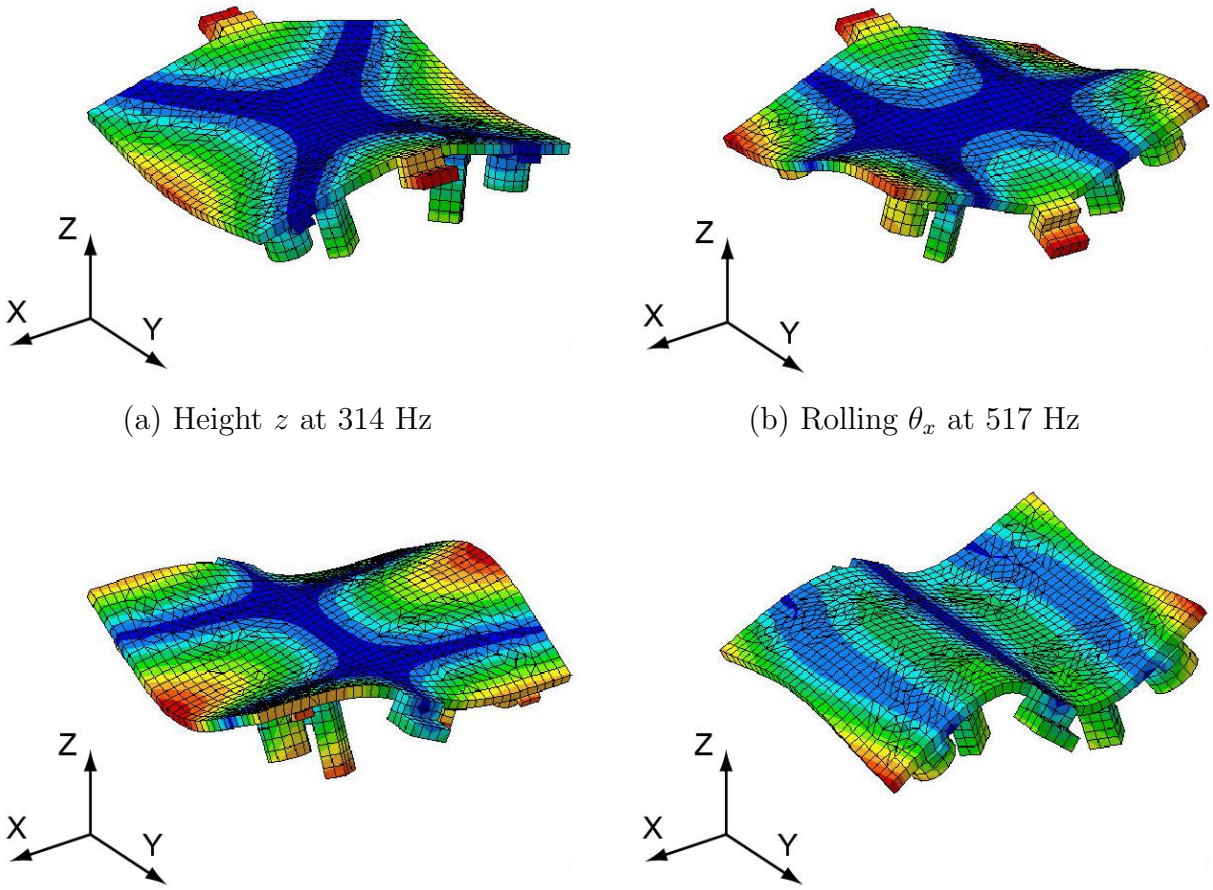

(a) Height z at 314 Hz

(b) Rolling θ_x at 517 Hz

(c) Pitching θ_y at 625 Hz

(d) Pitching θ_y at 869 Hz

Figure 9.4: Modal patterns of table part.

9.4 Control System Design

9.4.1 Feedback Control Design

Feedback controllers are designed for the plant models respectively based on pole placement design. A PID position controller is designed for the plant of the translation x, as the band frequency of the position loop is 10 Hz. For the other plants, I-PD position controllers are designed. The band frequencies of the position loop are 50 Hz, 20 Hz and 20 Hz for the height z, the rolling θ_x and the pitching θ_y, respectively.

9.4.2 Proposed System

The proposed system is based on PTC and a decoupling control for a coupling term between the translation and the pitching.

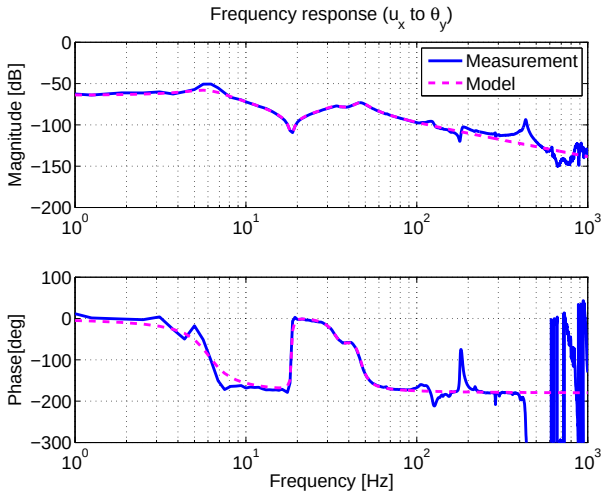

Figure 9.5: Frequency responses of coupling term.

The stage is driven dynamically in x direction. PTC is applied for the control system of x axis in order to control the translation x fast and precisely.

Then, the coupling term exists between the translation x and the pitching θ_y. Fig. 9.5 shows the frequency response from the input u_x to the pitching θ_y. A decoupling controller is designed in the control system of θ_y axis for the coupling term. The coupling term is modeled as

$$\begin{aligned} G(s) &= \frac{\theta_y}{u_x} \\ &= \frac{b_{d4}s^4+b_{d3}s^3+b_{d2}s^2+b_{d1}s+b_{d0}}{a_{d6}s^6+a_{d5}s^5+a_{d4}s^4+a_{d3}s^3+a_{d2}s^2+a_{d1}s+a_{d0}}. \end{aligned} \tag{9.7}$$

This model is a minimum phase system.

A decoupling term which is added to the input $u_{\theta y}$ can be designed as $P_{\theta y}^{-1}G(s)$ in continuous time. Here, the relative degrees of both $P_{\theta y}(s)$ and $G(s)$ are just 2-order respectively. Thus, the decoupling term $P_{\theta y}^{-1}G(s)$ can be designed because the system is a biproper minimum phase system. The discretized model $P_{\theta y}^{-1}G[z]$ by Tustin transform is applied to the control system. Fig. 9.6 shows the proposed system.

9.5 Experiments

Experiments are performed by three steps. The specification of the sampling periods is shown in Table 9.1. First, the control system which consists of only feedback controllers is performed. The target position trajectory is based on 5-order polynomials. The target position and velocity trajectories are shown in Fig. 9.7. These trajectories in time 0 s to 0.5 s, 1 s to 1.5 s, 2 s to 2.5 s and 3 s to 3.5 s are in acceleration and deceleration regions.

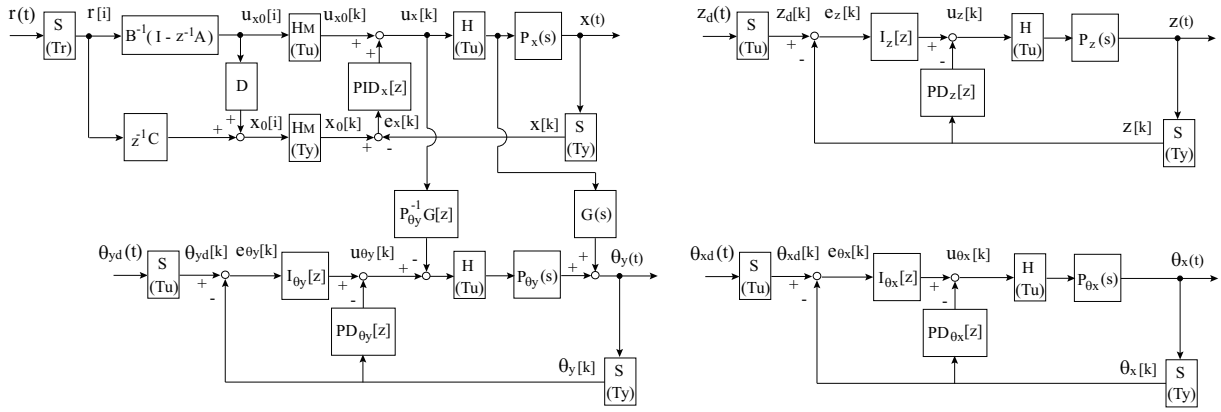

Figure 9.6: Proposed system.

Table 9.1: Sampling periods.

T_r	T_u	T_y
0.4 ms	0.2 ms	0.2 ms

These trajectories in time 0.5 s to 1 s, 2.5 s to 3 s are in constant velocity regions. These trajectories are same below experiments. The position errors in all axes are shown in Fig. 9.8(a). The position error of the translation x in acceleration and deceleration regions is worse without a feedforward controller. In the same region, the pitching θ_y is influenced by the translation x response.

Second, the control system which consists of PTC in x axis is performed. The experimental results of PTC are shown in Fig. 9.8(b). In acceleration and deceleration regions, the position error of the translation x is improved. However, in constant velocity region, the error is vibrating at 5 Hz which is 2-order harmonics caused by unbalanced three phase of the linear motors. In this chapter, it is not improved any more although a compensator for the harmonics is available.

Finally, the proposed system is performed. The experimental results of the proposed system are shown in Fig. 9.8(c). In acceleration and deceleration regions, the position errors of not only the translation x but also the pitching θ_y are improved by the decoupling control.

9.6 Summary

In this chapter, a 4-DOF precision stage, which was named "Nano-stage Ⅱ," was designed and fabricated for precise position control including the structure of the table part. A control system which was based on PTC and a decoupling control for a coupling term between

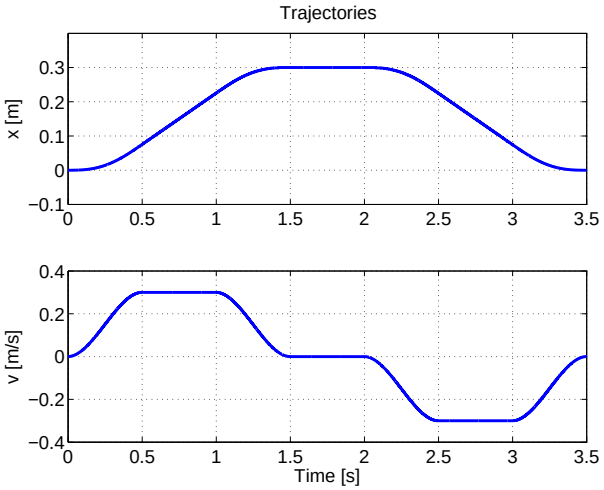

Figure 9.7: Trajectories.

the translation and the pitching was proposed. Experiments were performed to show the advantages of the proposed system.

In future works, improvement of the position control of the translation x in constant velocity periods and coupling models which influence the height z and the rolling θ_x are considered.

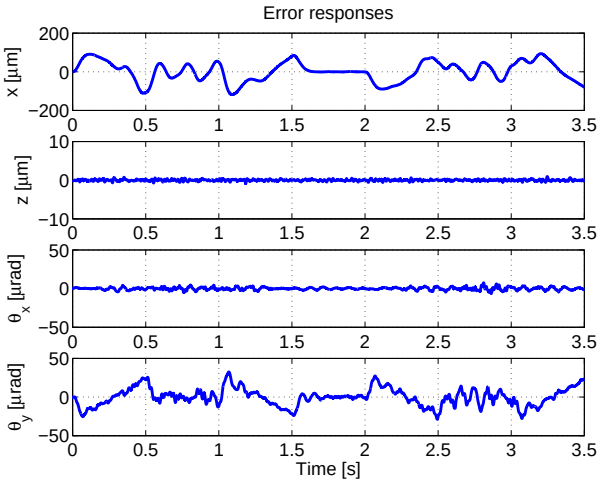

(a) FB only

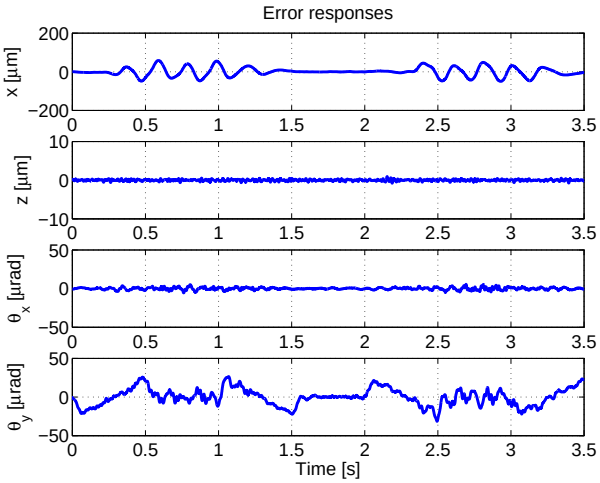

(b) PTC

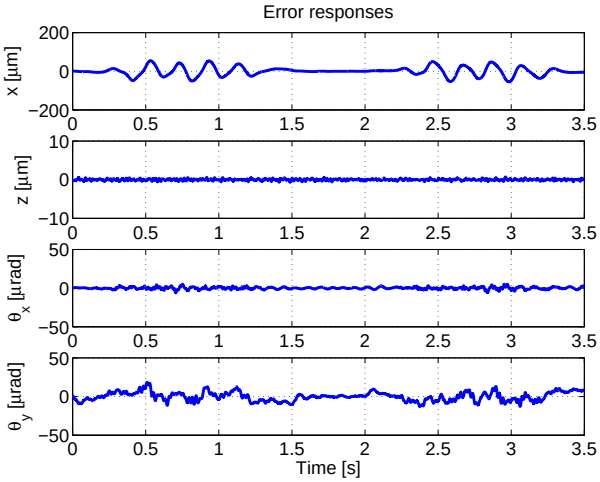

(c) Proposed system

Figure 9.8: Time responses.

Chapter 10

Conclusion

In this dissertation, applications of multirate control techniques to high-precision stages were introduced, and then multirate control techniques which extended to power electronics, sensors and mechanics around control techniques were established.

From chapter 2 to chapter 4, PTC method based on multirate feedforward control were applied to practical precision stages which required not only fast and precise positioning but also synchronous position control and attitude control. In chapter 2, appropriate modeling of the step stage and the gantry stage was performed. Vibration suppression PTC [21] was applied. Especially, the feedforward control was quite effective to large-scale high precision stages which had the resonance modes.

In chapter 3, a novel synchronous position control system based on multirate control was proposed for a pair of precision stages which were designed by PTC in previous chapter. The proposed synchronous position control consists of the PTC and the observer, and can compensate the dead-time of the system.

In chapter 4, an attitude control based on multirate control was proposed. The disturbances via the driving force in the translation direction and the surface shape of the stage were modeled. In the proposed attitude control, the disturbance information is utilized as the target trajectory. Therefore, the disturbance can be rejected in high frequency bandwidth even though the sampling time of the sensor is much longer. These proposed multirate control techniques for practical precision stages were performed in experiments, and then effectiveness of these techniques were evaluated.

From chapter 5 to chapter 9, multirate control techniques which extended to power electronics, sensors and mechanics around control techniques were established. In chapter 5, multirate PWM control which combined multirate control with modeling based on PWM pulses of the inverter was proposed. This is a novel multirate control technique which introduces power electronics technique with considering dynamics of the inverter. Experiments with an experimental high-precision stage were performed to show the advantages of the

proposed control technique.

In chapter 6, it was shown that multirate control technique with considering dynamics of the driver was effective in not only position control but also speed and current control. The proposed control technique can satisfy both reduction of switching loss of the driver and the tracking performance. Moreover, the robustness of multirate feedforward controller was verified both theoretically and experimentally.

In chapter 7, an observer which can estimate state variables with reducing the quantization error of the encoder was proposed. The proposed observer based on multirate control utilizes the difference between the updating time of the observer and the sampling time of control input. Experiments with experimental precision stages were performed to show the advantages of the proposed observer.

In chapter 8, another position sensor was applied to a high-precision stage in the case that it was difficult to change the structure additionally. It was shown that it was possible to design a novel feedback control which not only had high bandwidth but also was absolutely robust against the resonance mode parameters. Finally, the proposed control design was generalized to the general 2 inertia system.

In chapter 9, a new experimental 4-DOF high-precision stage was designed and fabricated. The structure of the table part was analyzed by both FEM analyses and experimental modal analyses, and then relationship between the mode shapes and plant characteristics was demonstrated. Moreover, control systems in chapter 2 and 4 were applied to the stage, and experiments were performed to show the advantages of the control systems.

Application examples in these chapters showed that the performance of the proposed methods was superior to that of the conventional method and it is possible to apply to practical precision stages. These facts showed that this dissertation gave a big contribution to the subject of precise positioning. Moreover, this dissertation succeeded establishing of a novel multirate control techniques which extend to power electronics, sensors and mechanics.

Appendix A

Derivation of Equations (3.12) and (3.13)

$$\begin{aligned}\hat{\boldsymbol{x}}_m[k-n_{dm}+1] &= \boldsymbol{A}_{zm}\hat{\boldsymbol{x}}_m[k-n_{dm}]+\boldsymbol{b}_{zm}u_m[k-n_{dm}] \\ &\quad +\boldsymbol{H}(y_m[k]-\boldsymbol{c}_{dm}\hat{\boldsymbol{x}}_m[k-n_{dm}]-\boldsymbol{d}_{dm}u_m[k-n_{dm}])\end{aligned}$$

$$\begin{aligned}\hat{\boldsymbol{x}}_m[k-n_{dm}+2] &= \boldsymbol{A}_{zm}\hat{\boldsymbol{x}}_m[k-n_{dm}+1]+\boldsymbol{b}_{zm}u_m[k-n_{dm}+1] \\ &= \boldsymbol{A}_{zm}^2\hat{\boldsymbol{x}}_m[k-n_{dm}]+[\boldsymbol{A}_{zm}\boldsymbol{b}_{zm},\boldsymbol{b}_{zm}]\begin{bmatrix}u_m[k-n_{dm}]\\ u_m[k-n_{dm}+1]\end{bmatrix} \\ &\quad +\boldsymbol{A}_{zm}\boldsymbol{H}(y_m[k]-\boldsymbol{c}_{dm}\hat{\boldsymbol{x}}_m[k-n_{dm}]-\boldsymbol{d}_{dm}u_m[k-n_{dm}])\end{aligned}$$

In the same way,

$$\begin{aligned}\hat{\boldsymbol{x}}_m[k] &= \boldsymbol{A}_{zm}\hat{\boldsymbol{x}}_m[k-1]+\boldsymbol{b}_{zm}u_m[k-1] \\ &= \boldsymbol{A}_{zm}^{n_{dm}}\hat{\boldsymbol{x}}_m[k-n_{dm}]+[\boldsymbol{A}_{zm}^{n_{dm}-1}\boldsymbol{b}_{zm},\boldsymbol{A}_{zm}^{n_{dm}-2}\boldsymbol{b}_{zm},\cdots,\boldsymbol{b}_{zm}]\begin{bmatrix}u_m[k-n_{dm}]\\ \vdots \\ u_m[k-1]\end{bmatrix} \\ &\quad +\boldsymbol{A}_{zm}^{n_{dm}-1}\boldsymbol{H}(y_m[k]-\boldsymbol{c}_{dm}\hat{\boldsymbol{x}}_m[k-n_{dm}]-\boldsymbol{d}_{dm}u_m[k-n_{dm}])\end{aligned}$$

(3.12) is obtained. From this equation,

$$\begin{aligned}\boldsymbol{e}_m[k] &= \boldsymbol{x}_m[k]-\hat{\boldsymbol{x}}_m[k] \\ &= \boldsymbol{A}_{zm}^{n_{dm}}(\boldsymbol{x}_m[k-n_{dm}]-\hat{\boldsymbol{x}}_m[k-n_{dm}])-\boldsymbol{A}_{zm}^{n_{dm}-1}\boldsymbol{H}\boldsymbol{c}_{dm}(\boldsymbol{x}_m[k-n_{dm}]-\hat{\boldsymbol{x}}_m[k-n_{dm}]) \\ &= (\boldsymbol{A}_{zm}^{n_{dm}}-\boldsymbol{A}_{zm}^{n_{dm}-1}\boldsymbol{H}\boldsymbol{c}_{dm})\boldsymbol{e}_m[k-n_{dm}]\end{aligned}$$

(3.13) is obtained.

Bibliography

[1] R. A. de Callafon and P. M. J. Van den Hof, "Multivariable feedback relevant system identification of a wafer stepper system," *IEEE Trans. Control Syst. Technol.*, vol. 9, no. 2, pp. 381–390, 2001.

[2] M. van de Wal, G. van Baars, F. Sperling, and O. H. Bosgra, "Multivariable H_∞/μ feedback control design for high-precision wafer stage motion," *Control Engineering Practice*, vol. 10, no. 7, pp. 739–755, 2002.

[3] Z. Z. Liu, F. L. Luo, and M. A. Rahman, "Robust and precision motion control system of linear-motor direct drive for high-speed X-Y table positioning mechanism," *IEEE Trans. Ind. Electron.*, vol. 52, no. 5, pp. 1357–1363, 2005.

[4] M. F. Heertjes, X. G. P. Schuurbiers, and H. Nijmeijer, "Performance-improved design of N-PID controlled motion systems with applications to wafer stages," *IEEE Trans. Ind. Electron.*, vol. 56, no. 5, pp. 1347–1355, 2009.

[5] G. Cheng, K. Peng, B. M. Chen, and T. H. Lee, "Improving transient performance in tracking general references using composite nonlinear feedback control and its application to high-speed XY-table positioning mechanism," *IEEE Trans. Ind. Electron.*, vol. 54, no. 2, pp. 1039–1051, 2007.

[6] H.-J. Shieh and C.-H. Hsu, "An adaptive approximator-based backstepping control approach for piezoactuator-driven stages," *IEEE Trans. Ind. Electron.*, vol. 55, no. 4, pp. 1729–1738, 2008.

[7] KL. Moore, "Iterative learning control a survey and new results," *Journal of Robotic Systems*, vol. 9, no. 5, pp. 563–594, 1992.

[8] C. L. van Oosten, O. H. Bosgra, and B. G. Dijkstra, "Reducing residual vibrations through iterative learning control, with application to a wafer stage," in *Proc. American Control Conference*, pp. 5150–5155, 2004.

[9] H. Ding and J. Wu, "Point-to-point motion control for a high-acceleration positioning table via cascaded learning schemes," *IEEE Trans. Ind. Electron.*, vol. 54, no. 5, pp. 2735–2744, 2007.

[10] S. H. van der Meulen, R. L. Tousain, and O. H. Bosgra, "Fixed structure feedforward controller design exploiting iterative trials: application to a wafer stage and a desktop printer," *Journal of Dynamic Systems, Measurement and Control*, vol. 130, 051006-1/16, 2008.

[11] K. Yuki, T. Murakami, and K. Ohnishi, "Vibration control of a 2 mass system by the resonance ratio control," *Trans. IEE of Japan. IA*, vol. 113, no. 10, pp. 1162–1169, 1993 (in Japanese).

[12] Y. Hori, H. Sawada, and Y. Chun, "Slow resonance ratio control for vibration suppression and disturbance rejection in torsional system," *IEEE Trans. Industrial Electronics*, vol. 46, no. 1, pp. 162–168, 1999.

[13] T. Atsumi, T. Arisaka, T. Shimizu, and T. Yamaguchi, "Vibration servo control design for mechanical resonant modes of a hard-disk-drive actuator," *JSME International Journal Series C*, vol. 46, no. 3, pp. 819–827, 2003.

[14] S. Katsura and K. Ohnishi, "Vibration control of multi-mass resonant system based on phase-lead compensator," *Trans. IEE of Japan. IA*, vol. 126, no. 12, pp. 1601–1607, 2006 (in Japanese).

[15] T. Totani and H. Nishimura, "Final-state control using compensation input," *Trans. of the SICE*, vol. 30, no. 3, pp. 253–260, 1994.

[16] M. Hirata, T. Hasegawa, and K. Nonami, "Short track-seeking control of hard disk drives by using final-state control," *Trans. IEE of Japan. IA*, vol. 125, no. 5, pp. 524–529, 2005 (in Japanese).

[17] M. Iwasaki, K. Sakai, and N. Matsui, "Genetic algorithms-based design of vibration suppression compensator for 2-mass resonant system," *Trans. IEE of Japan. IA*, vol. 120, no. 3, pp. 351–358, 2000 (in Japanese).

[18] K. Ito, M. Iwasaki, and N. Matsui, "GA-based autonomous feedforward compensator design for robust fast-response and high-precision positioning," *Journal of JSPE*, vol. 69, no. 1, pp. 58–63, 2003 (in Japanese).

[19] K. Ito, R. Nagata, M. Iwasaki, and N. Matsui, "GA-based autonomous design of robust fast and precise positioning considering machine stand vibration suppression," *Trans. IEE of Japan. IA*, vol. 124, no. 6, pp. 607–615, 2004 (in Japanese).

[20] H. Fujimoto, Y. Hori, and A. Kawamura, "Perfect tracking control based on multirate feedforward control with generalized sampling periods," *IEEE Trans. Industrial Electronics*, vol. 48, no. 3, pp. 636–644, 2001.

[21] H. Fujimoto, K. Fukushima, and S. Nakagawa, "Vibration suppression short-span seeking of HDD with multirate feedforward control," in *Proc. American Control Conference*, pp. 582–587, 2006.

[22] J. Otsuka, "Present and future technique of ultraprecision positioning," *JSPE*, vol. 61, no. 12, pp. 1645–1649, 1995 (in Japanese).

[23] K. J. Åström, P. Hangander and J. Sternby, "Zeros of sampled system," *Automatica*, vol. 20, no. 1, pp. 31–38, 1984.

[24] M. Tomizuka, "Zero Phase error tracking algorithm for digital control," *ASME, J. Dynam. Syst., Measur.*, vol. 109, pp. 65–68, 1987.

[25] K. Sakata and H. Fujimoto, "Perfect tracking control of servo motor based on precise model with PWM hold and current loop," in *Proc. The Fourth Power Conversion Conference*, pp. 1612–1617, 2007.

[26] M. Iwasaki, M. Kawafuku, and H. Hirai, "2DOF Control-Based Fast and Precise Positioning for Vibratory Mechanism with Nonlinear Friction," in *Proc. IEEE International Conference on Mechatronics*, pp. 27–31, 2006.

[27] M. Nakamura, S. Goto, and N. Kyura, "Mechatronic Servo System Control," *Springer Berlin / Heidelberg*, pp. 149–168, 2004.

[28] X. Yang, K. Masaki, H. Suzuki, and S. Makinouchi, "Synchronization Control for High-Speed and High-Precision Stage of Scanning Stepper," in *Proc. JIASC*, pp. 55–60, 2001, in Japanese.

[29] K. Saiki, A. Hara, K. Sakata, and H. Fujimoto, "A Study on High-Speed and High-Precision Tracking Control of Large-Scale Stage Using Perfect Tracking Control Method Based on Multirate Feedforward Control," in *Proc. the 10th Internatinal Workshop on Advanced Motion Control*, pp. 206–211, 2008.

[30] Hiroshi Fujimoto and Yoichi Hori, "Visual servoing based on intersample disturbance rejection by multirate sampling control – Time Delay Compensation and Experimental Verification –," in *Proc. 40th IEEE Conference on Decision and Control*, pp. 334–339, 2001.

[31] S. Wakui, "Roles of an Active Anti-Vibration Apparatus in Precision Positioning," *J. JSPE*, vol. 73, no. 4, pp. 405-409, 2007 (in Japanese).

[32] K. Komata, S. Iguchi, H. Kadono, S. Toyooka, and N. Arai, "Study on Laser Direct Imaging System for Next Generation to Use Statistical Interferometry," *SAITEC*, vol. 4, 2006 (in Japanese).

[33] H. Fujimoto and Y. Hori, "Vibration suppression and optimal repetitive disturbance rejection control in semi-Nyquist frequency region using multirate sampling control," in *Proc. 39th IEEE Conf. on Decision and Contr.* , pp. 3745–3750, 2000.

[34] T. Yokoyama, M. Horiuchi, and S. Simogata, "Instantaneous deadbeat control for PWM inverter using FPGA based hardware controller," in *Proc. 29th Annu. IEEE IECON*, vol. 1, pp. 180–185, 2003.

[35] H. Abe and H. Fujimoto, "Multirate perfect tracking control of single-phase inverter with inter sampling for arbitrary waveform," in *Proc. PCC–Nagoya*, pp. 810–815, 2007.

[36] K. P. Gokhale, A. Kawamura, and R. G. Hoft, "Deat beat microprocessor control of PWM inverter for sinusoidal output waveform synthesis," *IEEE Trans. Ind. Appl.*, vol. 23, no. 5, pp. 901–910, 1987.

[37] H. Fujimoto, K. Fukushima, and S. Nakagawa, "Vibration suppression multirate seeking control of hard disk drives," in *Proc. AMC*, pp. 153–158, 2006.

[38] K. Sakata, H. Fujimoto, and K. Saiki, "Positioning of large-scale high-precision stage with vibration suppression PTC," in *Proc. 17th IFAC World Congress*, pp. 3124–3129, 2008.

[39] S. -G. Jeong and M. -H. Park, "The analysis and compensation of dead-time effects in PWM inverters," *IEEE Trans. Ind. Electron.*, vol. 38, no. 2, pp. 108–114, 1991.

[40] T. Umeno and Y. Hori, "Robust speed control of DC servomotors using modern two degrees-of-freedom controller design," *IEEE Trans. Ind. Electron.*, vol. 38, no. 5, pp. 363–368, 1991.

[41] T.-J. Kweon and D.-S. Hyun, "High-performance speed control of electric machine using low-precision shaft encoder," *IEEE Trans. power Electron.*, vol. 14, no. 5, pp. 838–849, 1999.

[42] Y. A.-R. I. Mohamed, "Design and implementation of a robust current-control scheme for a PMSM vector drive with a simple adaptive disturbance observer," *IEEE Trans. Ind. Electron.*, vol. 54, no. 4, pp. 1981–1988, 2007.

[43] Y. Terada, T. Nakai, and H. Fujimoto, "Proposal of high-speed and high-precision control method for SPMSM based on perfect tracking control with multirate PWM –low-carrier current control and inspection of position control with high-resolution encoder–," in *Proc. IEE of Japan Technical Meeting Record*, IIC-08-46, 2008 (in Japanese).

[44] R. C. Kavanagh and J. M. D. Murphy, "The effects of quantization noise and sensor nonideality on digital-differentiator-based velocity measurement," *IEEE Trans. Instrumentation and Measurement*, vol. 47, no. 6, pp. 1457–1463, 1998.

[45] T. Ohmae, T. Matsuda, K. Kamiyama, and M. Tachikawa, "A microprocessor-controlled high-accuracy wide-range speed regulator for motor drives," *IEEE Trans. Industrial Electronics*, vol. 29, no. 3, pp. 207–211, 1982.

[46] R C. Kavanagh, "Improved digital tachometer with reduced sensitivity to sensor non-ideality," *IEEE Trans. Industrial Electronics*, vol. 47, vo. 4, pp. 890–897, 2000.

[47] T. Tsuji, T. Hashimoto, H. Kobayashi, M. Mizuochi, and K. Ohnishi, "A wide-range velocity measurement method for motion control," in *IEEE Trans. Industrial Electronics*, vol. 56, no. 2, pp. 510–519, 2009.

[48] N. Iiyama, K. Ohnishi, and T. Tsuji, "An approach to estimate velocity for acceleration control," in *Proc. 10th IEEE International Workshop on Advanced Motion Control*, pp. 687-692, 2008.

[49] K. Fujita and K. Sado, "Instantaneous speed detection with parameter identification for ac servo systems," *IEEE Trans. Industry Applications*, vol. 28, no. 4, pp. 864–872, 1992.

[50] Y. Hori, T. Umeno, T. Uchida, and Y. Konno, "An instantaneous speed observer for high performance control of dc servo motor using DSP and low precision shaft encoder," in *Proc. 4th European Conf. Power Electronics*, vol. 3, pp. 647–652, 1991.

[51] G. Obinata, T. Sato, K. Hiramoto, Y. Muragishi, and Y. Kurita, "Simultaneous optimization for structural and control subsystems: the case of the regulator problem," *Trans of the Japan Society of Mechanical Engineers, Series C*, vol. 61, no. 591, pp. 4264–4269, 1995 (in Japanese).

[52] S. Hara and H. Yamaura, "Integrated design for magnetic head positioning mechanism and control," *Journal of the Society of Instrument and Control Engineers*, vol. 41, no. 6, pp. 406–411, 2002 (in Japanese).

[53] A. Hara, K. Saiki, H. Fujimoto, and K. Sakata, "Basic examination on simultaneous optimization of mechanism and control," in *Proc. IEE of Japan Technical Meeting Record*, IIC-07-127, 2007 (in Japanese).

[54] Y. Seki, H. Fujimoto, A. Hara, T. Yamanaka, and K. Saiki, "Basic examination of simultaneous optimization of mechanical and control design for gantry-type precision stage modeled as two-mass 4-DOF system," in *Proc. The 36rd Annual Conference of the IEEE Industrial Electronics Society*, pp. 1872–1877, 2010.

[55] K. Seki, K. Mochizuki, M. Iwasaki, and H. Hirai, "High-precision positioning with strain feedback using piezoelectric element," *Trans. IEE of Japan. IA*, vol. 130, no. 4, pp. 560–567, 2010 (in Japanese).

List of Publications

Journals

1. K. Sakata and H. Fujimoto, "Perfect tracking control of servo motor based on precise model considering current loop and PWM hold," *Trans. IEE of Japan. IA*, vol. 127, no. 6, pp. 587–593, 2007 (in Japanese).

2. K. Sakata, H. Fujimoto, T. Ohtomo, and K. Saiki, "Auto focus and leveling control of large-scale high-precision scan-stage using driving force and surface shape of the stage," *Trans. IEE of Japan.* IA, vol. 129, no. 6, pp. 564–570, 2009 (in Japanese).

International conference

1. K. Sakata and H. Fujimoto, "Perfect tracking control of servo motor based on precise model with PWM hold and current loop," in *Proc. The Fourth Power Conversion Conference*, pp. 1612–1617, 2007.

2. K. Sakata, H. Fujimoto, T. Shimoyama, and K. Saiki, "Improvement of fast and precise positioning of large-scale high-precision step-stage based on vibration suppression PTC," in *Proc. The 33rd Annual Conference of the IEEE Industrial Electronics Society (IECON'07)*, pp. 339–344, 2007.

3. K. Sakata, H. Fujimoto, and K. Saiki, "Positioning of large-scale high-precision stage with vibration suppression PTC," in *Proc. The 17th IFAC World Congress*, pp. 3124–3129, 2008.

4. K. Sakata, H. Fujimoto, A. Hara, and K. Saiki, "Design fabrication of high-precision stage and ultrahigh-speed nanoscale positioning," in *Proc. American Control Conference*, pp. 2254–2259, 2009.

5. K. Sakata and H. Fujimoto, "Master-slave synchronous position control for precision stages based on multirate control and dead-time compensation," in *Proc. IEEE/ASME*

International Conference on Advanced Intelligent Mechatronics (AIM'09), pp. 263–268, 2009.

6. K. Sakata and H. Fujimoto, "Proposal of multirate PWM positioning control considering resonance mode for precision stage," in *Proc. The 35rd Annual Conference of the IEEE Industrial Electronics Society (IECON'09)*, pp. 3156–3161, 2009.

7. K. Sakata, H. Fujimoto, A. Hara, T. Ohtomo, and K. Saiki, "Design fabrication and control of 4-DOF high-precision stage," in *Proc. The 11th International Workshop on Advanced Motion Control (AMC'10)*, pp. 366–370, 2010.

8. K. Sakata, H. Fujimoto, L. Peretti, and M. Zigliotto, "Enhanced speed and current control of PMSM drives by perfect tracking algorithms," in *Proc. IPEC-Sapporo2010*, pp. 587–592, 2010.

9. K. Sakata and H. Fujimoto, "Proposal of long sampling short cycle observer for quantization error reduction," in *Proc. IEEE International Symposium on Industrial Electronics (ISIE'10)*, pp. 1919–1924, 2010.

Domestic conference

1. K. Sakata and H. Fujimoto, "Perfect tracking control of servo motor based on PWM hold model," in *Proc. IEE of Japan Technical Meeting Record*, IIC-06-62, 2006 (in Japanese).

2. K. Sakata and H. Fujimoto, "Perfect tracking control of servo motor based on precise model considering current loop and PWM hold," in *Proc. IEE of Japan Industry Applications Society Conference*, vol. 1, pp. 163–168, 2006 (in Japanese).

3. K. Sakata, H. Fujimoto, T. Shimoyama, and K. Saiki, "Fast and precise positioning control of large scaled high precision step-stage using vibration suppression PTC," in *Proc. T. SICE 6th Annual Conference on Control System*, 065-3-1, 2007 (in Japanese).

4. K. Sakata, H. Fujimoto, T. Ohtomo, and K. Saiki, "Auto focus and leveling control of large-scale high-precisition scan-stage based on multirate control," in *Proc. IEE of Japan Technical Meeting Record*, IIC-07-124, 2007 (in Japanese).

5. K. Sakata, H. Fujimoto, T. Ohtomo, and K. Saiki, "Experimental verification on auto focus and leveling control of scan-stage using driving force and surface shape of the stage," in *Proc. IEE of Japan Technical Meeting Record*, IIC-08-44, 2008 (in Japanese), (*1).

6. K. Sakata, H. Fujimoto, A. Hara, and K. Saiki, "Design fabrication of high-precision stage and experimental verification on ultrahigh-speed nanoscale positioning," in *Proc. IEE of Japan Industry Applications Society Conference*, vol. 2, pp. 165–168, 2008 (in Japanese), (*2).

7. K. Sakata and H. Fujimoto, "Master-slave synchronous position control for experimental precision stages based on multirate control and dead-time compensation," in *Proc. IEE of Japan Technical Meeting Record*, IIC-08-161, 2008 (in Japanese).

8. K. Sakata and H. Fujimoto, "Nanoscale servo based on mechanism for precision stage – proposal of multirate PWM positioning control considering resonance mode –," in *Proc. IEE of Japan Technical Meeting Record*, IIC-09-100, 2009 (in Japanese).

9. K. Sakata and H. Fujimoto, "Proposal of moving difference long sampling observer for quantization error reduction," in *Proc. IEE of Japan Technical Meeting Record*, IIC-09-161, 2009 (in Japanese).

10. K. Sakata, H. Fujimoto, and K. Saiki, "Application of perfect tracking control method for positioning control of large-scale high-precision stage," in *Proc. The 28th Annual Conference of The Robotics Society of Japan*, RSJ2010AC1F1-3, 2010 (in Japanese).

11. K. Sakata and H. Fujimoto, "High bandwidth design of feedback control system using multiple sensors for high-precision stage," in *Proc. The 39th SICE Symposium on Control Theory*, pp. 285–290, 2010 (in Japanese), (*3).

12. K. Sakata, H. Fujimoto, and K. Saiki, "Design of feedback control for robustness of resonance mode using multiple sensors for high-precision gantry stage," in *Proc. IEE of Japan Technical Meeting Record*, IIC-11-065, 2011 (in Japanese).

Coauthor papers

1. A. Hara, K. Saiki, H. Fujimoto, and K. Sakata, "Basic examination on simultaneous optimization of mechanism and control," in *Proc. IEE of Japan Technical Meeting Record*, IIC-07-127, 2007 (in Japanese).

2. K. Saiki, A. Hara, K. Sakata, and H. Fujimoto, "A study on high-speed and high-precision tracking control of large-scale stage using perfect tracking control method based on multirate feedforward control," in *Proc. The 10th IEEE International Workshop on Advanced Motion Control (AMC'08)*, pp. 206–211, 2008.

3. K. Saiki, K. Hirachi, K. Sakata, and H. Fujimoto, "High-speed and high-precision tracking control of large-scale stage using perfect tracking control with disturbance observer," in *Proc. Annual Conference of the IEEE Industrial Electronics Society (IECON'08)*, pp. 2545–2550, 2008.

4. A. Hara, K. Saiki, K. Sakata, and H. Fujimoto, "Basic examination on simultaneous optimization of mechanism and control for high precision single axis stage and experimental verification," in *Proc. Annual Conference of the IEEE Industrial Electronics Society (IECON'08)*, pp. 2509–2514, 2008.

5. K. Saiki, T. Shimoyama, K. Sakata, and H. Fujimoto, "Positioning of large-scale high-precision viscoelastic stage based on vibration suppression PTC," in *Proc. Annual Conference of the IEEE Industrial Electronics Society (IECON'09)*, pp. 3150–3155, 2009.

6. H. Fujimoto, K. Sakata, and K. Saiki, "Application of perfect tracking control to large-scale high-precision stage," in *Proc. The 5th IFAC Symposium on Mechatronic Systems*, pp. 188–193, 2010.

7. K. Saiki, T. Shimoyama, K. Sakata, and H. Fujimoto, "Investigation of an appropriate nominal model and high-precision positioning of large-scale stage using perfect tracking control," *Trans. IEE of Japan. IA*, vol. 130, no. 8, pp. 1022–1029, 2010 (in Japanese).

8. K. Saiki, A. Hara, K. Sakata, and H. Fujimoto, "A study on high-speed and high-precision tracking control of large-scale stage using perfect tracking control method based on multirate feedforward control," *IEEE Trans. on Industrial Electronics*. vol. 57, no. 4, pp. 1393–1400, 2010.

International patents

1. H. Fujimoto, K. Sakata, K. Saiki, and T. Ohtomo, publication no. WO2009/031654.

Domestic patents

1. H. Fujimoto, K. Sakata, K. Saiki, and A. Hara, publication no. 2009-65058.

2. H. Fujimoto, K. Sakata, and K. Saiki, publication no. 2010-39004.

Awards

1. K. Sakata, "Excellent Paper Presentation Award" for paper (*1), *IEE of Japan Technical Meeting*, December, 2008.

2. K. Sakata, "Excellent Paper Presentation Award (A)" for paper (*1), *IEE of Japan*, March, 2009.

3. K. Sakata, "Excellent Paper Presentation Award (A)" for paper (*2), *IEE of Japan*, September, 2009.

4. K. Sakata, "Academic Encouragement Award (Technique Encouragement Award)" for paper (*3), *SICE*, February, 2011.